MOTION ARTIFACT REDUCTION TECHNIQUES IN MAGNETIC RESONANCE IMAGING

A DISSERTATION
SUBMITTED TO THE DEPARTMENT OF ELECTRICAL AND ELECTRONICS ENGINEERING
AND THE INSTITUTE OF ENGINEERING AND SCIENCE
OF BİLKENT UNIVERSITY
IN PARTIAL FULFILLMENT OF THE REQUIREMENTS
FOR THE DEGREE OF
DOCTOR OF PHILOSPHY

By
Ergin Atalar
July 1991

I certify that I have read this dissertation and that in my opinion it is fully adequate, in scope and in quality, as a dissertation for the degree of Doctor of Philosophy.

Assoc. Prof. Levent Onural (Supervisor)

I certify that I have read this dissertation and that in my opinion it is fully adequate, in scope and in quality, as a dissertation for the degree of Doctor of Philosophy.

Prof. Hayrettin Köymen

I certify that I have read this dissertation and that in my opinion it is fully adequate, in scope and in quality, as a dissertation for the degree of Doctor of Philosophy.

Prof. Cemal Yalabık

I certify that I have read this dissertation and that in my opinion it is fully adequate, in scope and in quality, as a dissertation for the degree of Doctor of Philosophy.

Prof. Ziya İder

I certify that I have read this dissertation and that in my opinion it is fully adequate, in scope and in quality, as a dissertation for the degree of Doctor of Philosophy.

Assoc. Prof. Haluk Tosun

Approved for the Institute of Engineering and Science:

Prof. Mehmet Baray,
Director of Institute of Engineering and Science

Abstract

MOTION ARTIFACT REDUCTION TECHNIQUES IN MAGNETIC RESONANCE IMAGING

Ergin Atalar
Ph. D. in Electrical and Electronics Engineering
Supervisor: Assoc. Prof. Levent Onural
July 1991

It is shown that the expansion/shrinkage and rotational motions of the body cause phase and amplitude distortions and non-rectangular sampling over the k-domain. If these distortions are not compensated then the reconstructed image will suffer from "*the motion artifact*". The mathematical relation between motion and motion artifact is given. If the motion of the body is known, it is possible to obtain motion artifact free images. The motion is estimated either by using the information in the acquired data or by direct measurement. These estimates and the relation between motion and artifact are used to compensate the phase and amplitude distortions. Using the non-rectangular samples over the k-domain the rectangular samples are obtain by the aid of the singular value decomposition method. And finally, the inverse Fourier transform of these calculated samples gives the motion artifact free image. The proposed method is tested by simulations. For the estimation of the motion, two methods are proposed and tested. The first method is an iterative image reconstruction method. The second one uses the navigator echoes to obtain the amount of motion.

Keywords: Magnetic Resonance Imaging, Motion Artifact Reduction in MRI, Respiratory Motion Artifact,

Özet

MANYETİK REZONANS GÖRÜNTÜLEMEDE KIPIRTI BOZUKLUKLARININ GİDERİLME YÖNTEMLERİ

Ergin Atalar
Elektrik ve Elektronik Mühendisliğinde Doktora
Tez Yöneticisi: Doç. Dr. Levent Onural
Temmuz 1991

Manyetik rezonans görüntülemede, görüntülenen cismin dönme ve genişleyip daralma hareketlerinin toplanan verilerin evre ve genliklerinde bozukluklara ve Fourier dönüşüm düzlemindeki örneklerin istenenden farklı yerlede alınmasına neden olduğu gösterilmiştir. Gerekli düzeltmeler yapılmazsa görüntülerde "*kıpırtı bozuklukları*" oluşur. Hareket ile bozukluklar arasındaki matematiksel ilişkiler verilmiştir. Cismin nasıl kıpırdadığı tam olarak biliniyorsa, net görüntülerin elde edilmesi mümkündür. Önerilen yöntemde, elde edilen verilerden ya da doğrudan ölçümlerden cismin hareketi kestirilir. Bu kestirim sonuçlarını ve bilinen hareket-bozulma ilişkisini kullanarak evre ve genliklerdeki hatalar düzeltilir. Fourier düzleminde ölçümlerle elde edilmiş örnekler kullanılarak tekil değer ayrışımı yöntemi ile düzgün aralıklı yerleşik yeni örnekler hesaplanır. Son olarak da bu hesaplanan değerlerin ters Fourier dönüşümü alınarak bozukluğu giderilmiş görüntü elde edilir. Önerilen yöntem benzetim ile elde edilmiş veriler kullanılarak denenmiştir. Yukarıda belirtilen hareket kestirimi için de iki yöntem önerilmiş ve denemiştir. Bunlardan ilki bir tekrarlamalı görüntü onarım yöntemidir. İkincisi ise yönlendirici yankı (navigator echo) kullanılarak kıpırdama miktarının bulunması ilkesine dayanmaktadır.

Anahtar sözcükler: Manyetik Rezonans Görüntüleme, Manyetik Rezonans Görüntülemede Kıpırtı Etkilerinin Giderilmesi, Görüntü Bozuklukları

Acknowledgement

On the completion of this dissertation I would like to express my appreciation to all those who have contributed in one way or another.

I gratefully thank Prof. Levent Onural for his supervision in every stages of this dissertation. I started working on magnetic resonance imaging by his encouragement. We had many long and useful discussions. He directed my research with a perfect timing. In addition, I am obliged to him for his effort in correcting the English text.

I have been working as a member of the MRI team in Biomedical lab of the Middle East Technical University, Electrical and Electronics Engineering Department for a long time. I would like to thank all the team members for their continuous support during my long dissertation period. I should also acknowledge the directors of the team, Prof. Ziya İder and Prof. Hayrettin Köymen. Without their helps it was impossible to complete this dissertation.

I attended to a very intensive magnetic resonance imaging course in KAIST MRI lab., Korea in April-June 1989. Prof. Z. H. Cho and his students taught me the basics of magnetic resonance imaging. Our relation continued after this course. They wrote me valuable comments on my research. I would like to thank Prof. Z. H. Cho and his students for their efforts.

I would like to thank my friend Dr. Erkan Tekman for his valuable comments on the second chapter of the dissertation.

Thanks should also be given to my wife, Şelale. To prepare this dissertation I somewhat neglected our family and social contacts. She accepted that without any murmur. Her constant patience and care which have made it possible for me to concentrate fully on the work for this dissertation.

Contents

List of Figures

Chapter 1

INTRODUCTION

In the last decade magnetic resonance imaging (MRI) became one of the major imaging methods used for the diagnosis of various kinds of illnesses. Although the cost of a magnetic resonance imaging instrument is very high, the capability of showing the cross-sectional image of the human body with very high soft tissue contrast makes it very useful. The MRI is based on the nuclear magnetic resonance (NMR) phenomenon which was discovered by Bloch [1] and Purcell [2] in 1946 independently. They both shared the 1952 Nobel prize for their invention. After the invention of NMR, it took a long period to get the first magnetic resonance image. In 1973, Paul Lauterbur [3] obtained the first MRI images. Until now, thousands of works were carried out to get higher quality magnetic resonance images. Impressive image quality improvement is achieved. But still there are many studies on getting higher and higher quality images.

One of the important problems of MRI is that the data acquisition process takes a long time (in the order of 10 minutes). In this interval, the patient must lie in an uncomfortable and noisy bore without any movement. In the standard magnetic resonance imaging methods any movement of the body during the data acquisition period causes image degradation which is called *the motion artifact.* To reduce the severity of this motion artifact problem usually the patients are fastened to the bed. But there are some physiological motions that can not be stopped such as the motion of the heart, blood flow and breathing. The motion

artifact due to these types of motions appear on the image as ghost-like replicas of the moving structure. In addition, the blurring of the moving structure is observed. These types of artifacts on the image may cause faulty diagnosis.

The studies on the solution of this problem can be divided into two main categories. The scientists working on the first category try to decrease the data acquisition time. To get a motion artifact free image, the data acquisition time must be much less than the one heart beat period (For a normal human, this period is in the order of 700 msec). Although there is a tremendous decrease in the data acquisition time, there is still a long way to go [‡]. Other scientists are trying to find MR imaging methods which minimize the effect of the motion to the acquired magnetic resonance signal. In these methods, the images are obtained by the standard image reconstruction method. The magnetic resonance signal is sampled as if there is no motion, and two-dimensional inverse Fourier transform of the collected data is evaluated to obtain the image.

In this dissertation, the motion artifact problem in MR imaging is analyzed and some artifact reduction methods are proposed. In these new methods, the MR signal is acquired using the standard Fourier transform imaging pulse sequence. The effect of motion is eliminated by signal processing methods. The image is obtained by calculating the inverse Fourier transform of the processed data.

In the next chapter a brief introduction to the nuclear magnetic resonance and magnetic resonance imaging are given. This introduction will be helpful for those who are not familiar with the magnetic resonance imaging. For those who already know the magnetic resonance imaging, the next chapter may be a review and an introduction to the notation that will be used in the later chapters. The third chapter is a literature survey. It is very difficult to cover all the methods which are used on the motion artifact reduction, but the author has selected the artifact reduction methods which are related to the approaches used in this dissertation. In the fourth chapter the effect of the motion to the MR signal

[‡]In some very recent studies subsecond MR imaging methods are announced [4]. But the images suffer from very poor resolution and very poor SNR.

will be formulated. This formulation will cover various forms of motion of the body. In the fifth chapter, the image reconstruction methods will be explained and the simulation results will be demonstrated. The last chapter is devoted to concluding remarks.

Chapter 2

BASICS OF MR IMAGING

As the title implies, the basic principles of the Magnetic Resonance Imaging (MRI) will be discussed in this chapter. Very well written tutorials on this subject can be found elsewhere [5]-[15]. The aims of this chapter are to introduce the basic principles to those who have no or little knowledge on MRI and to show the derivation of the basic imaging equation. In the next chapters this basic imaging equation will be modified to include the effects of the motion.

In the first section of this chapter, the nuclear magnetic resonance (NMR) phenomenon is shortly discussed, the equipment necessary for the observation of the phenomenon is introduced, and the famous spin echo pulse sequence is explained. In the second section of this chapter, the principles of the magnetic resonance imaging is mentioned and the imaging equation is constructed.

2.1 Nuclear Magnetic Resonance

If a sample is placed in a uniform time invariant magnetic field and is subject to radiofrequency (RF) radiation at the appropriate frequency, nuclei in the sample can absorb energy. This phenomenon is called "*nuclear magnetic resonance*" or "*NMR*" [16]. When the RF radiation is stopped, the energy absorbed by nuclei is emitted. The NMR phenomenon can be detected by the measuring either the absorbed or the emitted energy.

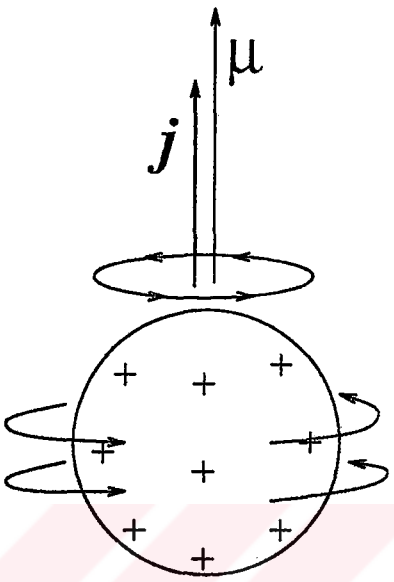

Figure 2.1: A spinning positively charged sphere has an angular momentum and a magnetic dipole moment which are in the same direction

Because of some special properties of the hydrogen, detection the NMR phenomenon for hydrogen nucleus (i.e. proton) is relatively easy. First, hydrogen is naturally abundant. Second, in the NMR experiments, it is shown that the level of energy absorption by hydrogen is higher than all the other elements [7]. For these reasons, in magnetic resonance imaging, the NMR for proton is used.

In this section, first the proton energy emission process is explained. The energy emission can be observed in a uniform magnetic field. For this reason, the behavior of protons in a uniform magnetic field is given. Second, a method for measuring the emitted energy is illustrated. Later, the proton energy absorption process is explained. And finally, the spin echo pulse sequence is introduced.

2.1.1 Protons in a Uniform Magnetic Field

The nuclear magnetic resonance of proton is a quantum mechanical phenomenon. But it is possible to visualize it in terms of classical electrodynamics by modeling

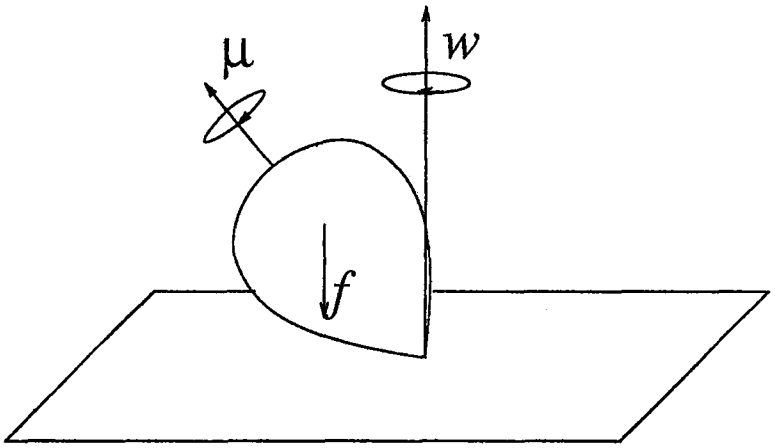

Figure 2.2: A rapidly spinning top. The gravitational force, f, acting to the top, and the spin of the top causes precession. The precession axis is parallel to f.

the proton as a spinning positively charged sphere (See Figure 2.1). The spinning sphere has both a magnetic dipole moment and an angular momentum. The rotating charges outside the sphere behave like a current passing through a circular wire. As a result of this current, a magnetic dipole moment, μ, will be produced [17]. The angular momentum of the sphere, j, will be in the same direction with the magnetic moment (See Figure 2.1). Thus

$$\mu = \gamma j \tag{2.1}$$

Quantum mechanically, a proton has an intrinsic angular momentum, called "*spin*". The spin, in turn, gives rise to a magnetic dipole moment. As in the spinning sphere case, the spin and the magnetic dipole moment of a proton are in the same direction. And therefore, Eq. 2.1 is also valid for a proton. In that equation, the scalar constant, γ, is called "*the gyromagnetic ratio*" (sometimes it is called the magnetogyric ratio).

The behavior of a spin under a uniform magnetic field is similar to the motion of a spinning top. The spin of the top causes rotation around the vertical axis (see Figure 2.2). This rotation is called the gyroscopic precession [18]. If the spin

is under a uniform magnetic field, $\boldsymbol{h}$, a torque acts on it as (See [17, page 15.1]):

$$\boldsymbol{\tau} = \boldsymbol{\mu} \times \boldsymbol{h} \tag{2.2}$$

This torque causes a change in the angular momentum of the proton, i.e.:

$$\boldsymbol{\tau} = \frac{d\boldsymbol{j}}{dt} \tag{2.3}$$

Using equations 2.1, 2.2, and 2.3 one may derive the following equation:

$$\frac{d\boldsymbol{\mu}}{dt} = \gamma \boldsymbol{\mu} \times \boldsymbol{h} \tag{2.4}$$

The above explanation is tricky because a quantum mechanical phenomenon is explained using the classical physics. However, the macroscopic behavior of the protons obeys the results obtained by this derivation. A quantum mechanical explanation exists and the same macroscopic results can be obtained [16].

The macroscopic form of Eq. 2.4 is in the same form. But in this form, we will not have spins and individual protons instead we will have spin density and proton density. Another name of the spin density is "*magnetization*, and its symbol is m. Therefore, the macroscopic equation for NMR is

$$\frac{d\boldsymbol{m}}{dt} = \gamma \boldsymbol{m} \times \boldsymbol{h} \tag{2.5}$$

In NMR, the motion of the magnetization under time invariant magnetic field is very important. Let the magnetic field be

$$\boldsymbol{h} = H_0 \hat{\boldsymbol{z}} \tag{2.6}$$

where $\hat{\boldsymbol{z}}$ is the unit vector along the z-direction. Here, the direction of the magnetic field is arbitrarily selected. For the case of time invariant magnetic field (Eq. 2.6), the solution of Eq. 2.5 is

$$m_x(t) = m_x(0)\cos(\omega_0 t) + m_y \sin(\omega_0 t) \tag{2.7}$$

$$m_y(t) = -m_x(0)\sin(\omega_0 t) + m_y \cos(\omega_0 t) \tag{2.8}$$

$$m_z(t) = m_z(0) \tag{2.9}$$

where m_x, m_y, and m_z are the x, y, and z components of the magnetization vector $\boldsymbol{m}$, respectively. and

$$\omega_0 = \gamma H_0 \tag{2.10}$$

In general, it can be said that in a static magnetic field, the magnetization vector rotates around the axis of the magnetic field with, so called, the Larmor frequency ω_0. This motion of the magnetization is called the precessional motion because the spins of the protons axes cause rotation around the axis of the magnetic field.

2.1.2 The Rotating Frame

The analysis of the magnetization vector is much more easier if a rotating frame is introduced. This is frequently used in the explanation of the NMR related phenemona.

In the previous subsection, it is derived that in a uniform time invariant magnetic field, the magnetization vector rotates around the axis of the field. For the field, H_0, in the z direction, the rotation axis was the z-axis and the frequency was ω_0 (see Eq. 2.10). Let x', y', and z' be the coordinates of the rotating frame which rotates around the z-axis with the frequency ω_0 in the same direction with the precessional motion.

Since the rotation frequency of the frame and the magnetization are the same, the magnetization vector stays still in the rotating frame (see Figure 2.3).

From the behavior of the magnetization vector on the rotating frame one can deduce that there is no effective magnetic field [9]. In the theoretical analysis of this fact, one can find the same result: *the rotating frame cancels the effect of the main magnetic field.* The basic NMR equation for the rotating frame can be written as:

$$\frac{d\boldsymbol{m}'}{dt} = \gamma \boldsymbol{m}' \times \boldsymbol{h}_{eff} \tag{2.11}$$

where

$$\boldsymbol{h}_{eff} = \boldsymbol{h}' - H_0 \hat{\boldsymbol{z}}.$$

The above equation is proved in Appendix A.

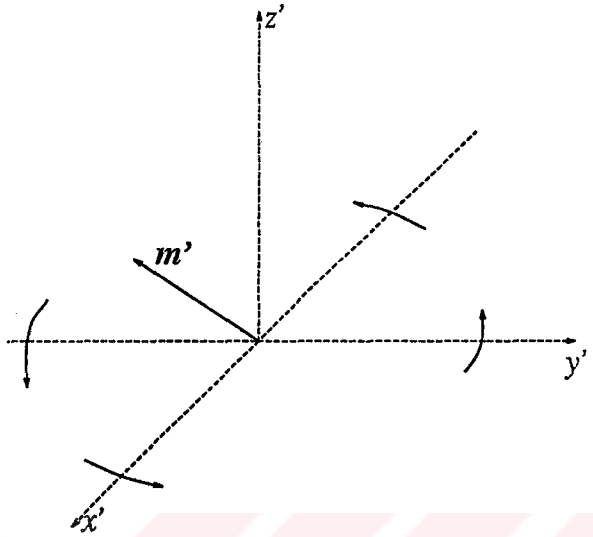

Figure 2.3: The rotating frame. In the rotating frame the magnetization vector seems to have no motion.

2.1.3 The Steady State Magnetization

The magnetization vector aligns with the applied magnetic field at the steady state although the previous formulation does not say anything about it. In the previous formulation the protons are assumed to have no interaction with their lattice and the other protons. As a result of these interactions, the protons give energy to the environment and the magnetization vector tends to stop its precession. This is similar to the effect of the friction to the motion of the spinning top. The motion of the magnetization vector toward its steady state position is called *the relaxation.*

Whatever the initial position is, the magnetization vector reaches a unique steady state value. This value, M_0, is proportional with the amplitude of the applied magnetic field and the proton density (See [16, page 2]):

$$M_0 = \chi_0 H_0 \tag{2.12}$$

where the variable χ_0 is called the static nuclear susceptibility. The susceptibility is proportional with the proton density, ρ, and inversely proportional with the

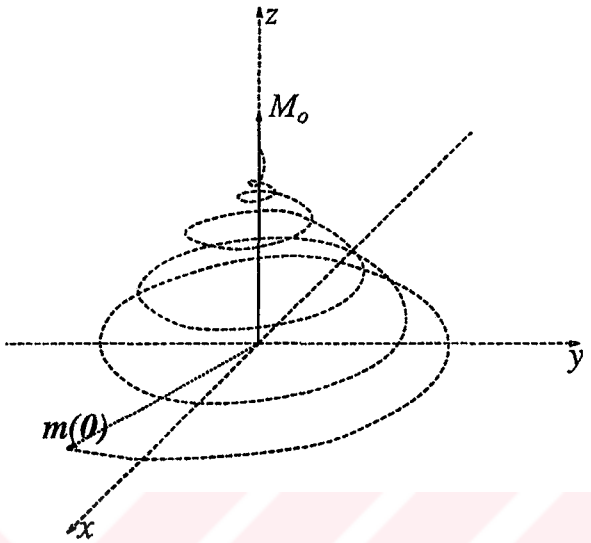

Figure 2.4: The relaxation of the magnetization vector. The magnetization vector has a spiral like motion. It rotates around z axis while moving towards its steady state value.

temperature when the temperature is given in Kelvins.

In magnetic resonance imaging (MRI), the aim is to obtain the image of the proton density distribution in the body. This is achieved by imaging the steady state magnetization, M_0, assuming the temperature and the main magnetic field intensity are space and time invariant.

2.1.4 The Relaxation Time Constants

Due to the relaxation, the magnetization vector moves in a spiral trajectory as shown in Figure 2.4. This motion can also be observed in the rotating frame (see Figure 2.5). This relaxation can be formulated by the aid of two time constants: T_1, *the longitudinal (spin-lattice)*, and T_2, *the transverse (spin-to-spin)* relaxation time constants.

The longitudinal component of the magnetization vector, m_z, moves toward

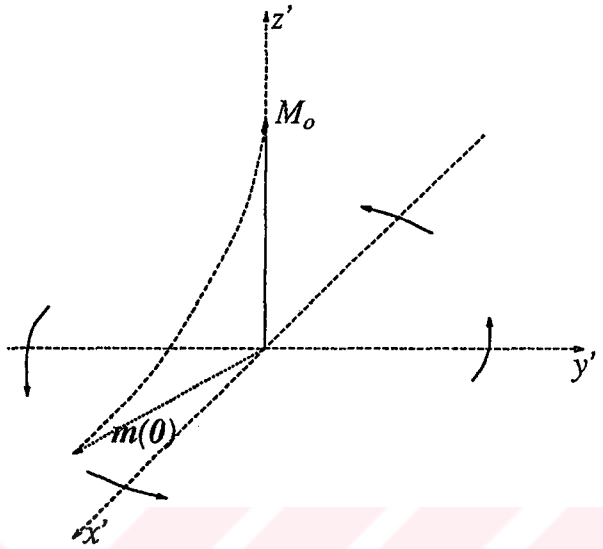

Figure 2.5: The relaxation of the magnetization vector in the rotating frame. The rotational motion of the magnetization vector can not be observed in the rotating frame. Only the motion due to the relaxation of the vector can be observed.

the steady state magnetization with the time constant T_1.

$$m_z(t) = \exp(-t/T_1)m_z(0) + (1 - \exp(-t/T_1))\, M_0 \tag{2.13}$$

The transverse components of the magnetization vector, (m_x and m_y) decays exponentially while rotating around the z-axis. The decay time constant is T_2. In the rotating frame only the exponential decay can be observed:

$$m'_x(t) = \exp(-t/T_2)m'_x(0) \tag{2.14}$$

$$m'_y(t) = \exp(-t/T_2)m'_y(0) \tag{2.15}$$

The transverse component of the magnetization vector may be shown in the complex number form[‡] as:

$$m = m'_x + jm'_y \tag{2.16}$$

[‡]In this text, the components of the magnetization vector will be shown in various forms. The magnetization vector is shown as a three dimensional vector with a symbol, $\boldsymbol{m}$. The

where $j = \sqrt{-1}$. The complex plane is defined as the rotating frame. In other words, if m is time invariant, it means the magnetization vector rotates around the z-axis with frequency ω_0. Using this complex notation, the equations 2.14 and 2.15 can be written as:

$$m(t) = m(0)\exp(-t/T_2) \tag{2.17}$$

Since the T_1 and T_2 time constants depend on the structure of the material, they are also space variant. In magnetic resonance imaging, not only the proton density distribution image, but also the T_1 and T_2 images can be obtained. Medical doctors usually prefer T_2 weighted proton density images because of their high contrast between the normal and the abnormal tissues.

T_1 is always longer then T_2, and the longest time constants are in the order of 1 second for the human body.

2.1.5 Receiving the NMR Signal

Observation of the motion of the magnetization vector is one of the key issues in the nuclear magnetic resonance. This can be achieved by measuring the emitted energy by the protons.

It is derived in the previous sections that, the transverse component of the magnetization vector has a rotational motion and the longitudinal motion of the magnetization vector is very slow. But on the other hand, with a simple RF (radio frequency) coil it is possible to observe the rapid rotational motion of the magnetization.

For example, a saddle-type RF coil (see Figure 2.6) which is placed along the z-direction is sensitive to the change of the magnetic field in the transverse plane. Examples of RF coil designs can be found in [19] - [21]. The RF coil which is

---

m_x, m_y and m_z are the x, y, and z components of it. The transverse components of the magnetization are m_x and m_y. And the longitudinal component of the vector is m_z. Symbols with prime in their notation are defined in the rotating frame (for example, m' and m'_z). Note that $m'_z = m_z$. And finally, m stands for the complex form representation of the transverse component of the magnetization.

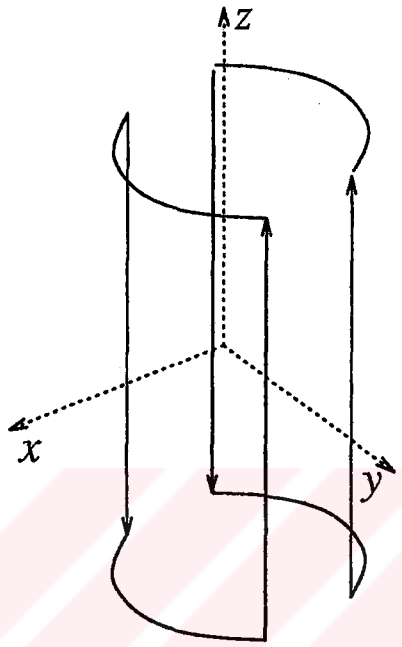

Figure 2.6: A sample RF coil: Saddle-type. This coil is sensitive to change of the total magnetization in the transverse plane.

placed around the object is stationary. So only the change of magnetic field may generate voltage across the coil.

In Figure 2.7, the block diagram the data acquisition unit is shown. Using this unit, the total magnetization in the volume of interest can be obtained. For this system, the relation between the magnetization and the received signal can be written as:

$$s(t) = \int w(\boldsymbol{x}) m(t; \boldsymbol{x}) d\boldsymbol{x} \tag{2.18}$$

where $s(t)$ is the complex form of the NMR signal which is given as:

$$s(t) = s_r(t) + j s_i(t)$$

and $\boldsymbol{x}$ and $d\boldsymbol{x}$ are the position vector and differential volume element, respectively:

$$\begin{aligned} \boldsymbol{x} &= [x, y, z]^T \\ d\boldsymbol{x} &= dxdydz \end{aligned}$$

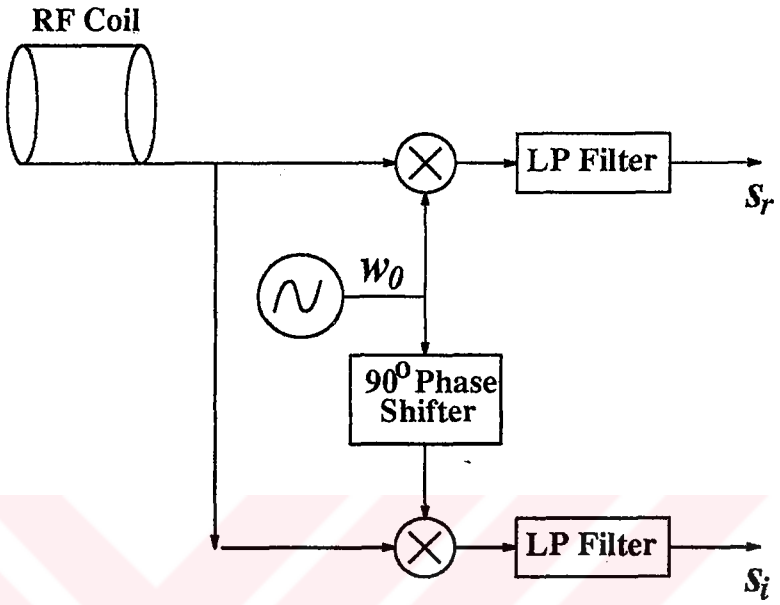

Figure 2.7: The block diagram of the data acquisition unit. The electrical signal at the output of the RF coil is a bandlimited signal which has a center frequency ω_0. The data acquisition unit changes the center frequency to 0, and digitize the data in the complex form.

In Eq. 2.18, w stands for the weighting function which is related to the design of the RF coil. In the RF coil design, the designer tries to make w space independent. The design is approximately valid for the volume of interest (VOI). Assuming a good RF coil design and no object outside the volume of interest, the above equation may be modified as:

$$s(t) = W \int_{VOI} m(t)dv \tag{2.19}$$

where W, which may be complex number, is the value of the weighting function in the volume of interest.

$$w(x) = W \qquad \text{for } x \in VOI \tag{2.20}$$

As a result, the received signal for the system shown in Figure 2.7 is equal to a constant times the transverse component of the total magnetization of the

body. Since the total magnetization is time dependent, the received signal is also time dependent. In magnetic resonance imaging, the steady state magnetization distribution will be found using the measurement of the transverse component of the total magnetization.

2.1.6 The Effects of RF Magnetic Field

In the steady state, the energy of the protons will vanish, the transverse component of the magnetization will be zero, and therefore the NMR signal cannot be observed. To observe the signal, the transverse component of the magnetization must be made non-zero. This can be achieved by tilting the magnetization vector. For this purpose a time limited additional radio frequency (RF) magnetic field is used:

$$\boldsymbol{h}(t) = H_0\hat{\boldsymbol{z}} + \begin{cases} 0 & t < 0 \\ H_1\mathcal{R}_z(\omega_0 t)\hat{\boldsymbol{y}} & \text{for } 0 < t < T_{RF} \\ 0 & t > T_{RF} \end{cases} \tag{2.21}$$

where H_1 and T_{RF} are the amplitude and the duration of the RF magnetic field, respectively. $\hat{\boldsymbol{y}}$ stands for the unit vector along the y-direction and $\mathcal{R}_z(\theta)$ is the rotation matrix which is defined as:

$$\mathcal{R}_z(\theta) \stackrel{\text{def}}{=} \begin{bmatrix} \cos(\theta) & \sin(\theta) & 0 \\ -\sin(\theta) & \cos(\theta) & 0 \\ 0 & 0 & 1 \end{bmatrix} \tag{2.22}$$

As it can be seen in the above equation, this magnetic field is composed of two parts: A static magnetic field along z direction and a time limited radio frequency (RF) magnetic field which rotates around the z-axis with a frequency of ω_0. Because of the short duration of the RF magnetic field, it is called *an RF pulse.*

Assume T_{RF} is selected so that

$$T_{RF} \ll T_1 \text{ and } T_2$$

It means there is no relaxation during the RF pulse period.

It is interesting to observe that in the rotating frame the analysis of this complicated magnetic field becomes very simple. In section 2.1.2, it is shown that the rotating frame cancels the effect of the main magnetic field. Therefore

$$\boldsymbol{h}_{eff}(t) = \begin{cases} 0 & t < 0 \\ H_1 \hat{\boldsymbol{y}}' & \text{for} \quad 0 \leq t \leq T_{RF} \\ 0 & t > T_{RF} \end{cases} \tag{2.23}$$

During the RF pulse period ($0 \leq t \leq T_{RF}$), the effective field appears as if it is a stationary field. It means the magnetization vector will rotate around the field axis (y') with frequency ω_1 (See Figure 2.8) where

$$\omega_1 = \gamma H_1. \tag{2.24}$$

Therefore at the end of the RF pulse, the magnetization vector will be tilted α radians in the $x' - z'$ plane (See Figure 2.9) where

$$\alpha = \gamma H_1 T_{RF} \tag{2.25}$$

Assume that the magnetization vector was at the steady state before the RF pulse:

$$\boldsymbol{m}(0) = [0, 0, M_0]^T. \tag{2.26}$$

Just after the RF pulse, the magnetization vector will be:

$$\boldsymbol{m}(T_{RF}) = [M_0 \sin(\alpha), 0, M_0 \cos(\alpha)]^T. \tag{2.27}$$

The maximum NMR signal can be obtained if the magnetization vector aligns with the x-axis. This can be achieve by the aid of an RF pulse whose H_1 and T_{RF} are arranged so that $\alpha = \frac{\pi}{2}$. In this case, the amplitude of the transverse component of the magnetization will be equal to M_0 (steady state magnetization) just after the RF pulse. This type of pulse is called a 90° RF pulse.

As a result, in a uniform time invariant magnetic field, the magnetization vector is aligned with the magnetic field. The position of this magnetization

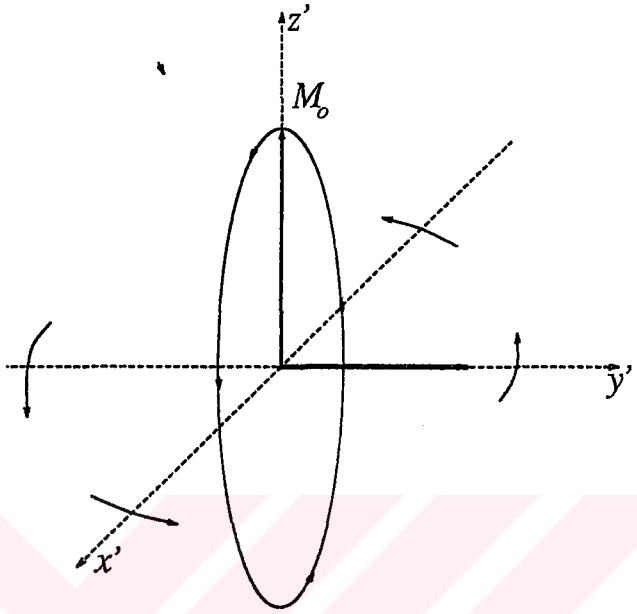

Figure 2.8: The effective magnetic field of the RF field in the rotating frame. If there is an RF magnetic field in the transverse direction with a frequency ω_0 in addition to a constant magnetic field, H_0, in the z direction, then the effective magnetic field in the rotating frame will be a constant magnetic field in the transverse plane. The magnetization vector rotates around the axis of this effective magnetic field.

vector can be changed by the aid of a RF magnetic field applied in the transverse plane, if the frequency of the RF field is *exactly* the same as the Larmor frequency of the protons which are in that field. In this way, energy can be transferred to the protons.

The analysis for the RF magnetic field which have a frequency other than ω_0 is not carried out here. But it can be shown that the RF pulse frequency is very critical. A slight change in the frequency causes *no* change in the magnetization vectors and therefore no energy transfer can be observed. The magnetization vectors *resonate* at the frequency ω_0. This phenomenon is called "*the nuclear magnetic resonance*".

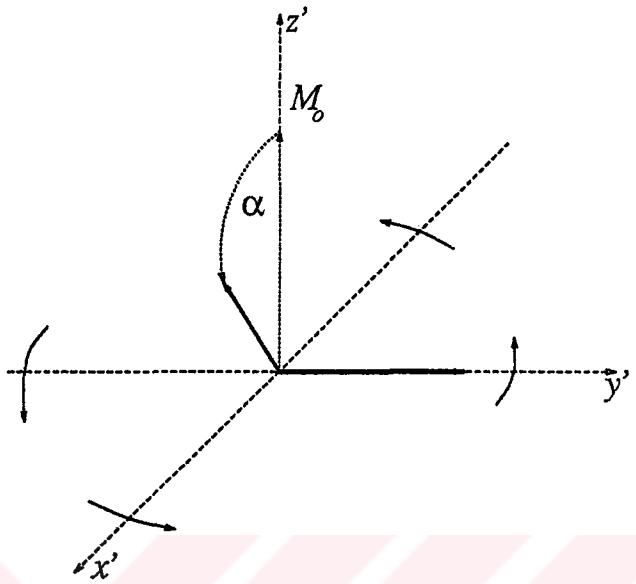

Figure 2.9: The effect of an RF pulse which has a tilt angle of α. A short RF pulse rotates the magnetization vector around its axis during the RF pulse application period. At the end of this period, the magnetization vector will be tilted towards the transverse plane. The tilt angle depends on the strength and the duration of the RF pulse.

2.1.7 The Spin Echo

As it is stated in the previous subsection, the angle of the RF pulse can be set to any value by controlling the duration and the amplitude of the RF pulse. The angles 90° and 180° have very special usage.

As it is stated in the previous subsection, the 90° RF pulse which is applied when the magnetization vector is at the steady state maximizes the transverse component of the vector. The maximization of the transverse component is very important because only this component of the magnetization vector can be measured. The 180° RF pulse which we are talking about is an RF pulse which is in phase with the x'-axis and and its amplitude and duration are arranged so that a 180° rotation of the magnetization vector around the x'-axis is obtained. If the

180° RF pulse is applied when all the magnetization vectors are in the transverse plane, their amplitudes will remain the same, but their angle with respect to the x'-axis will be the negative of their previous angles. In the complex notation:

$$m_+ = m_-^* \tag{2.28}$$

where m_-, and m_+ are the magnetizations before and after the 180° RF pulse, and $*$ indicates the complex conjugation.

Unfortunately, there are some measurement problems. The first one is that the transverse component of the magnetization can not be observed while the RF pulse is applied. Since the NMR signal and the RF pulse have the exactly same frequencies (Larmor frequency), in the acquisition of the NMR signal the effect of the RF magnetic field is unavoidable.

The second problem is the main magnetic field inhomogenity. In practice, it is impossible to obtain a uniform magnetic field. Under an inhomogeneous magnetic field, all the spins will have close but different Larmor frequencies. Usually the mean value of all of these Larmor frequencies is selected as the global Larmor frequency, and the angular velocity of the rotating frame, and the frequency of the RF field is equal to this global Larmor frequency. The spins which have different frequencies than the global Larmor frequency, move in the rotating frame with a frequency $\Delta\omega$ where

$$\Delta\omega = (\omega_0)_{spin} - (\omega_0)_{global}\,. \tag{2.29}$$

In the above equation, $(\omega_0)_{spin}$ and $(\omega_0)_{global}$ are the spin and the global Larmor frequencies. Note that $\Delta\omega$ is a function of space. In most systems, the maximum value of $\Delta\omega$ is in the order of 500 radians/seconds. The typical Larmor frequencies are in the range of 25 to 500 megaradians/second.

All the magnetization vectors are in the x direction just after the RF pulse, but they start moving with different angular velocities. After a short time interval all the vectors will be dispersed in the transverse plane. Since the NMR signal is the integration of the magnetization vectors, no signal can be obtained.

A useful signal can be obtained if and only if the magnetization directions are close to each other. Therefore a method for collecting the dispersed vectors in

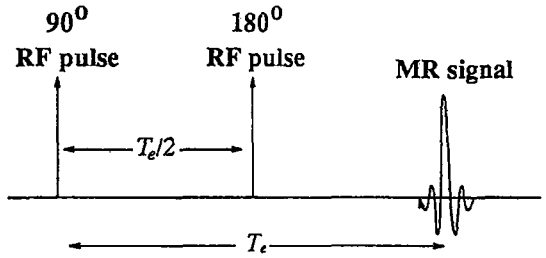

Figure 2.10: The spin echo RF pulse sequence

one direction is necessary.

The spin echo is the solution to this problem. Some time after the application of a 90° RF pulse, another RF pulse which has a tilt angle 180° is applied (See Figure 2.10). Assume that many spins are concentrated at a point and they all have close but different Larmor frequencies. Just after the 90° RF pulse, all of them are aligned in the transverse plane (See Figure 2.11). As the time goes on the spins are dispersed (Figure 2.12). At time $T_e/2$ a 180° RF pulse is applied. With this RF pulse the spins rotate around the x-axis (Figure 2.13). The spins which were moving in the positive direction now have negative angles. On the other hand, the spins which were moving in the negative direction now have positive angles. The faster moving spins have larger angles. After the 180° RF pulse the spins which have negative angles move in the positive direction, and the spins which have positive angles move in the negative direction. As the time goes the spins move towards the x-axis. At the echo time, T_e, all the spins are aligned and the NMR signal is obtained (Figure 2.14).

2.2 Magnetic Resonance Imaging

The ultimate aim of the magnetic resonance imaging (MRI) is to obtain a proton density image of a slice of the body. In addition to the proton density images, T_1 and T_2 weighted proton density images can be obtained. The meaning of the T_1, and T_2 weighted images will be clarified at the end of this section.

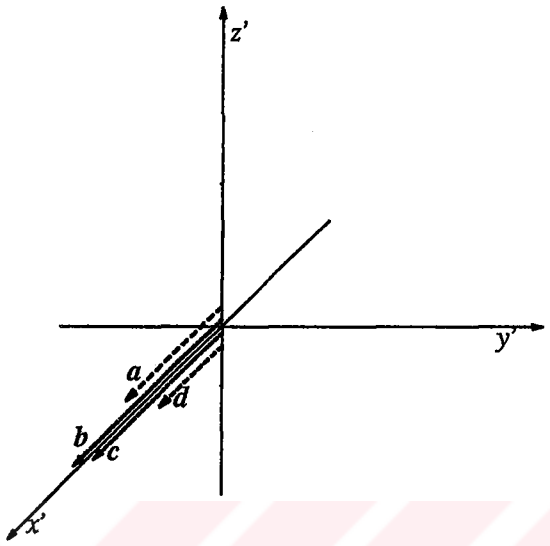

Figure 2.11: The positions of the magnetization vectors just after a 90° RF pulse.

In all MR imaging methods (there are many of them), the main idea is to make the Larmor frequency space and time variant. It is possible to have a one to one correspondence between the angular frequency of the rotation of the magnetization vector and the position if the field is designed properly. In the image reconstruction step, the amplitudes of the frequency components of the measured total magnetization are found using the Fourier transformation. And using the one to one relation between the frequency and the position, the MR image will be obtained.

For this purpose an expensive high precision instrument is needed. This instrument generates a very high uniform magnetic field. In addition to the this uniform field, a computer controlled time and space dependent perturbation magnetic is generated. With the proper adjustment of the perturbation magnetic field, the NMR signal is acquired and processed.

This section is a short introduction to MRI. In the first subsection, the MRI instrument will be explained. The space and time variant magnetic field generation method will be introduced. Then the basic imaging equation will be

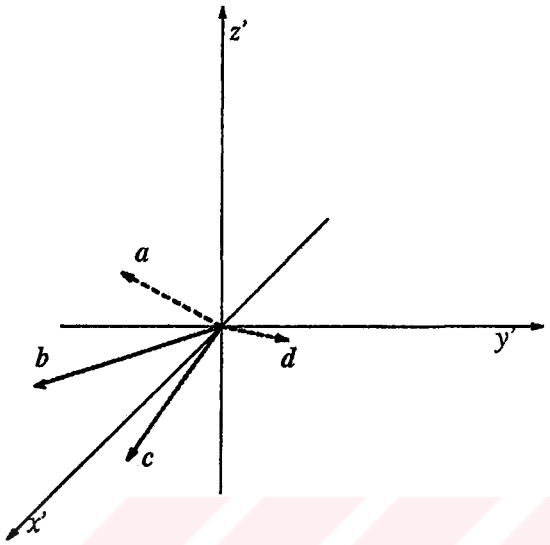

Figure 2.12: The magnetization vector dispersion due to the field inhomogenity. The positions of the magnetization vectors just before the 180° RF pulse are dispersed in the transverse plane. The vector $\boldsymbol{a}$ has a negative $\Delta\omega$, so it rotates in the clockwise direction and it has a large negative angle. $\boldsymbol{b}$ has also negative but smaller $\Delta\omega$, so the angle between the x axis and the magnetization vector b is smaller. On the other hand, the magnetization vectors $\boldsymbol{c}$ and $\boldsymbol{d}$ both have positive $\Delta\omega$ values.

derived. Using this imaging equation of the MRI, the Fourier transform imaging method will be explained.

2.2.1 The Instrument

The block diagram of the instrument is given in Figure 2.15. The instrument can be divided into four main categories: The magnet, the control block, the data acquisition unit, and the image generation unit. The control block generates five signals which control the magnetic field inside the magnet. The data acquisition unit was explained in Section 2.1.5. The signal digitized by the data acquisition unit is processed to obtain the magnetic resonance image in the image generation

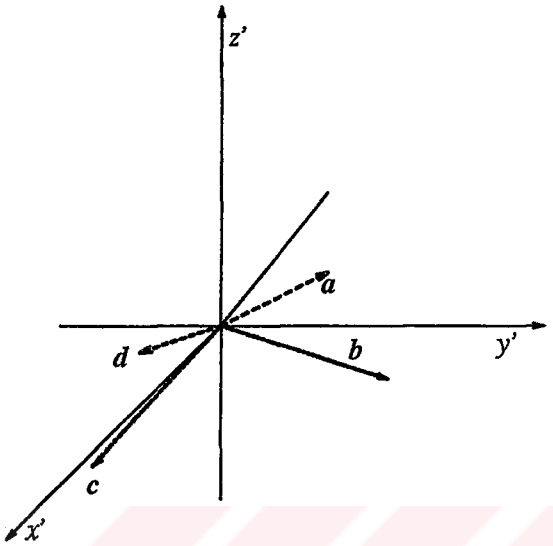

Figure 2.13: The positions of the magnetization vectors just after the 180° RF pulse. All the magnetization vectors are rotated around the x axis. All the spins are in the transverse plane, but the angles of the magnetization vector with x axis is negative of the angles just before the 180° RF pulse.

unit. The image generation algorithm will be explained later in this section. In this subsection, the magnet, which is the most important part of the instrument, will be explained.

The magnet has five or six coils: The main magnet coil, the x,y,z gradient coils, and the receive and transmit RF coils. In most systems, the receive and transmit coils are unified.

The main magnet generates a magnetic field along the z-direction (See Figure 2.16). Ideally, it is time and space invariant but because of the design difficulties the perfect time and space invariance cannot be achieved, but sufficiently good results can be obtained. Therefore the field generated by the main magnet can be written as a sum of a uniform field and the a perturbation position dependent magnetic field which is called *field inhomogenity.*

$$(H_0 + H_i(\boldsymbol{x}))\,\hat{\boldsymbol{z}}$$

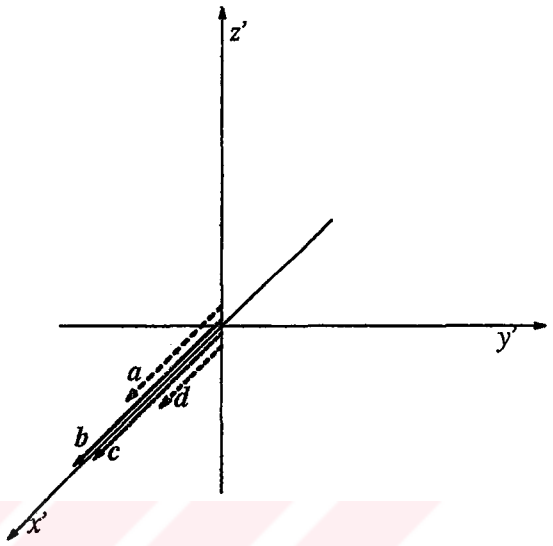

Figure 2.14: All the magnetization vectors align at the echo time, T_e, on the x axis.

where H_i stands for the field inhomogenity and $\boldsymbol{x}$ is the position vector, $[x, y, z]^T$. The field inhomogenity is measured in parts per million by comparing the maximum value of the inhomogeneous field to H_0. As the field inhomogenity increases the quality of the magnet decreases. Even for the highest quality magnets, the field inhomogenity can not be neglected.

The RF coil generates the RF field in the transverse plane. It has no component along the z-direction and the field is not space dependent but it is time variant. A typical RF coil was given in Figure 2.6. The RF coils can be used as a receiver or a transmitter. If an RF coil is used as an RF field generator, its field can be written as:

$$\mathcal{R}_z(\omega_0 t)\boldsymbol{q}(t)$$

where $\boldsymbol{q}(t) = [q_r(t), q_i(t), 0]^T$ and q_r and q_i are the real and the imaginary parts of the RF field envelope.

The gradient coils generate both space and time variant magnetic field along the z-direction. Ideally, there is no generated field in the other directions. The

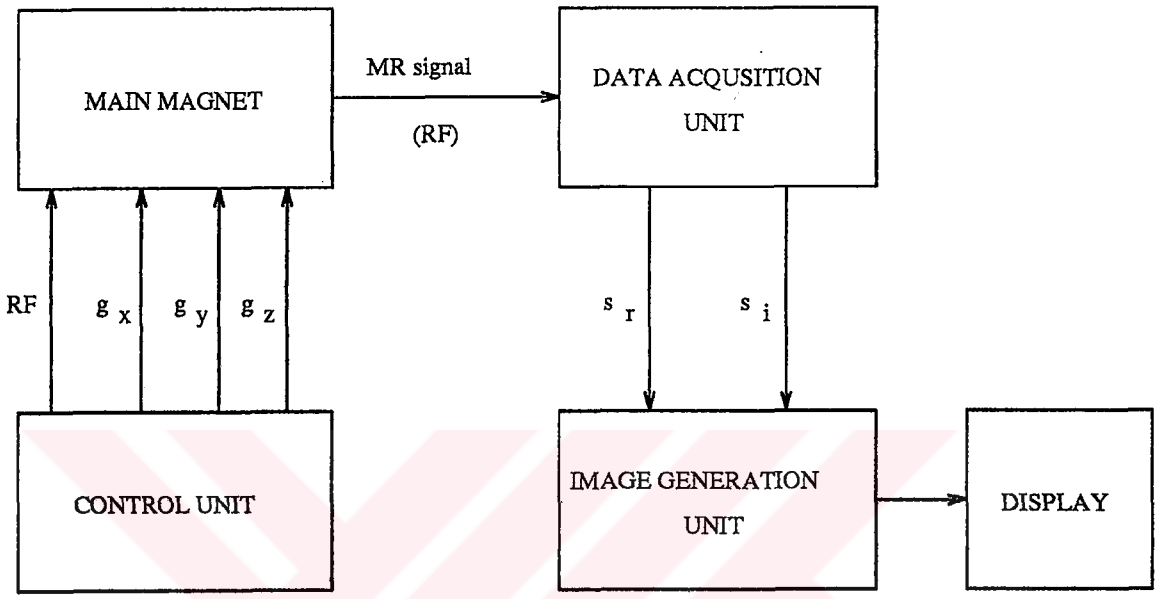

Figure 2.15: The block diagram of the magnetic resonance imaging instrument.

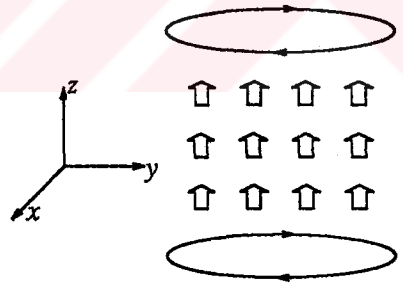

Figure 2.16: Typical main magnet coil. The coil generates uniform time invariant magnetic field in the z direction.

z-gradient is a magnetic field whose amplitude linearly varies with respect to z coordinate and there is no change along the x and y-directions. By controlling the current of the z gradient coil (See Figure 2.17), a time and space variant magnetic field may be obtained as:

$$g_z(t)z\hat{z} \tag{2.30}$$

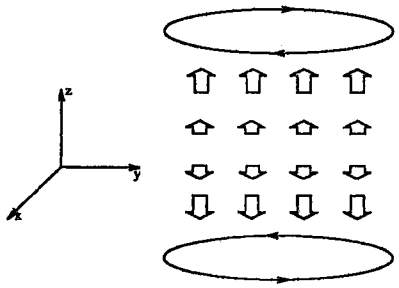

Figure 2.17: A typical z gradient coil. The coil generates magnetic field in the z direction. The field strength is linearly proportional with z and it can be any function of time.

In the above equation, g_z is the amplitude of the z-gradient. Similarly, x and y gradients are the fields in the z-direction whose amplitudes vary linearly with respect to x and y coordinates, respectively. Including all the gradients the following relation may be written:

$$(g_z(t)z + g_y(t)y + g_x(t)x)\,\hat{z} \tag{2.31}$$

where g_x and g_y are the amplitudes of the x and y gradients, respectively. Using vector notation. the above expression can be rewritten as:

$$\boldsymbol{g}^T(t)\boldsymbol{x}\hat{z} \tag{2.32}$$

where

$$\boldsymbol{g}(t) = [g_x(t), g_y(t), g_z(t)]^T.$$

The Larmor frequency in the magnet becomes time and space dependent as a consequence of the gradients. This time and space dependence can be controlled by q_r, q_i, g_x, g_y, and g_z inputs of the magnet. In general, the field generated by the magnet can be written as:

$$\boldsymbol{h}(t) = \left(H_0 + H_i(\boldsymbol{x}) + \boldsymbol{g}^T(t)\boldsymbol{x}\right)\hat{z} + \mathcal{R}_z(\omega_0 t)\boldsymbol{q}(t) \tag{2.33}$$

In the rotating frame, the effective magnetic field generated by the magnet is:

$$\boldsymbol{h}_{eff}(t) = \left(H_i(\boldsymbol{x}) + \boldsymbol{g}^T(t)\boldsymbol{x}\right)\hat{z} + \boldsymbol{q}(t) \tag{2.34}$$

In summary, in a magnetic resonance imaging instrument a uniform space and time invariant high magnetic field is perturbed by a small but space and time variant magnetic field. The perturbation is in the z direction and it is linear with respect to the space variables x, y, or z (if one ignores the effect of the field inhomogenity). In addition to these, there is a small RF field in the x-y plane. The RF field is time variant but space invariant. These small magnetic fields are controlled by the five signals: q_r, q_i, g_x, g_y, and g_z.

2.2.2 The Slice Selection Method

In this subsection, the slice selection method will be explained. The MR signal was equivalent to the total magnetization. But our aim is to find the magnetization at one point. As a first step to achieve this result, first, the magnetization vectors in a slice is excited and the magnetization vectors in the other slices are made stationary.

In Section 2.1.6, it is stated that the magnetization vectors can be tilted by an RF pulse if the RF frequency and the Larmor frequency exactly matches. If there is no gradient, all the points in the space will have the same Larmor frequency, therefore, an RF pulse in this frequency will tilt all of them.

Assume there is a non-zero z gradient when the RF pulse is applied. In this case, the Larmor frequency at each point will be different. If the Larmor frequency is ω_0 in the $z = 0$ plane, it will be either larger or smaller than ω_0 at other z values. So the magnetization vectors in the $z = 0$ plane will be tilted but all the vectors will remain in their steady state positions. Therefore, the transverse components of the total magnetization will be from the magnetization in the $z = 0$ plane. There will be no contribution from the other planes.

In this description of the slice selection, the slice thickness is infinitely small. The slice thickness can be controlled by applying an RF pulse which have a sinc envelope. Such an RF pulse and its frequency spectrum are shown in Figure 2.18. For such an RF pulse, the magnetization vectors which have Larmor frequencies between $\omega_0 - \Delta\omega/2$ and $\omega_0 + \Delta\omega/2$, will be tilted. If there is a z-gradient with

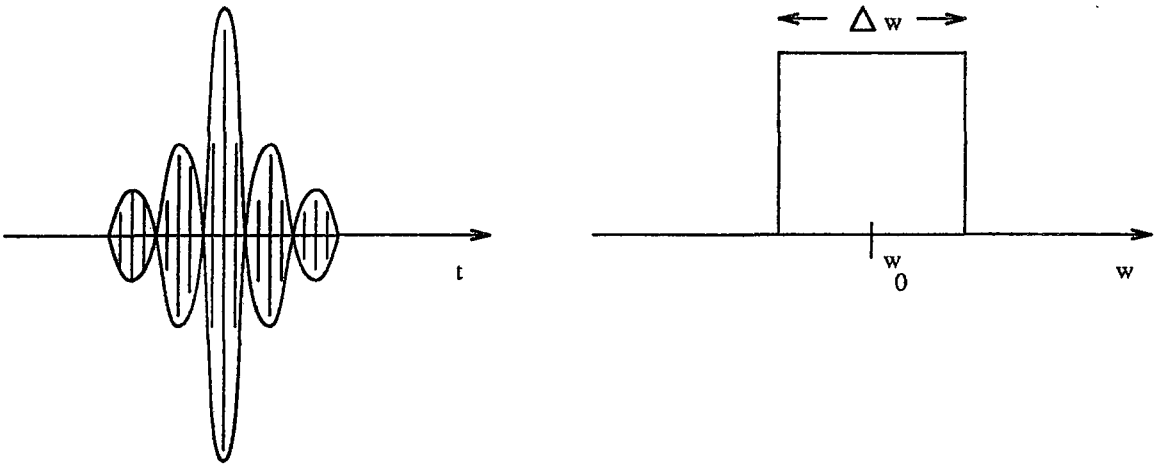

Figure 2.18: An RF pulse which has a sinc envelope and its Fourier transform

amplitude Q_z, the Larmor frequency distribution in space can be written as:

$$\omega = \omega_0 + \gamma Q_z z \tag{2.35}$$

The Larmor frequencies between $\omega_0 - \Delta\omega/2$ and $\omega_0 + \Delta\omega/2$ are in the slice $-D/2 < z < D/2$ where D is the slice thickness which can be found as:

$$D = \frac{\Delta\omega}{\gamma Q_z} \tag{2.36}$$

As a result, the magnetization vector in a slice which has a finite thickness can be excited. The slice thickness can be controlled by controlling the time between the zero crossing points of the sinc envelope.

For the slice selective RF pulse, the weight function, which is explained in Section 2.1.5, will be as:

$$w(\boldsymbol{x}) = W\text{rect}(z/D) \tag{2.37}$$

where

$$\text{rect}(u) = \begin{cases} 1 & \text{if } -1/2 < u < 1/2 \\ 0 & \textit{elsewhere} \end{cases} \tag{2.38}$$

It is common to assume that the proton density distribution is uniform along the z direction. The relation between the MR signal and the transverse

component of the magnetization (Eq. 2.19) may be modified for the signal generated by the selected slice:

$$s(t) = W \int_{-D/2}^{D/2} \iint_{ROI} m(\boldsymbol{x}; t) d\boldsymbol{x} \tag{2.39}$$

where ROI stands for region of interest. The region of interest is the selected slice in the volume of interest.

2.2.3 The Imaging Equation

The imaging equation that will be derived in this subsection is a relation between the proton density and the acquired signal. The subject covered until now is enough to derive the equation. Initially, the imaging equation for a special case will be derived, then the result will gradually be generalized. To get the simplest form of the imaging equation, assume that:

a. A 90° RF pulse is applied when all the magnetization vectors are in the steady state.

b. The 90° RF pulse is a slice selective one, and it selects a slice with a thickness of D.

c. There is only one 90° RF pulse which is applied at time 0, and the duration of the RF pulse (T_{RF} is negligibly small. This corresponds to $\boldsymbol{q}(t) = 0$ if $t \neq 0$.

d. There is no field inhomogenity.

e. There is no gradient.

Under these assumptions, $\boldsymbol{h}_{eff} = 0$, and therefore magnetization vectors will have the relaxation motion.

$$\boldsymbol{m}(t) = \begin{cases} M_0 \hat{\boldsymbol{z}} & \text{for } t < 0 \\ M_0 \left(1 - \exp(-t/T_1)\right) \hat{\boldsymbol{z}} + M_0 \exp(-t/T_2) \hat{\boldsymbol{x}} & \text{for } t > 0 \end{cases} \tag{2.40}$$

And the transverse component of the magnetization vector will be:

$$m(t) = \begin{cases} 0 & \text{for } t < 0 \\ M_0 \exp(-t/T_2) & \text{for } t > 0 \end{cases} \tag{2.41}$$

Now we may discard the assumptions (d) and (e), therefore, the gradients and the field inhomogenity are allowed. For this case,

$$\boldsymbol{h}_{eff}(t) = h(t)\hat{\boldsymbol{z}} \tag{2.42}$$

where

$$h(t) = \boldsymbol{g}^T(t)\boldsymbol{x} + H_i(\boldsymbol{x}).$$

To find the effect of $\boldsymbol{h}_{eff}$ to the magnetization vector, the basic NMR imaging for the rotating frame (Eq. 2.11) must be solved:

$$\frac{d\boldsymbol{m}'}{dt} = \gamma \boldsymbol{m}' \times \boldsymbol{h}_{eff}. \tag{2.43}$$

Finding the exact solution of Eq. 2.11 for the above $\boldsymbol{h}_{eff}$ is possible but it is not useful for the later discussion. But if one assumes that the variation in $\boldsymbol{h}$ is much less then the variation in $\boldsymbol{m}'$ then a simple solution for the motion of the magnetization vector can be obtained. The solution is based on the assumption that the first derivative of $\boldsymbol{h}_{eff}(t)$ is zero:

$$m(t) = M_0 \exp\left(j\phi(t)\right) \qquad \text{for } t > 0 \tag{2.44}$$

where

$$\begin{aligned} \phi(t) &= \int_0^t \omega(t')dt' \\ \omega(t) &= \gamma h(t). \end{aligned} \tag{2.45}$$

The derivation of the above equation is not included in the text but it can be found in the literature (See, for example [16]). In the above solution, the effect of the relaxation is not shown. If the relaxation of the spins were also considered, the following result would be obtained:

$$m(t) = M_0 \exp(-t/T_2) \exp\left(j\phi(t)\right) \qquad \text{for } t > 0 \tag{2.46}$$

When writing the above equation the phase of the magnetization at time 0 is assumed to be zero. In fact, this is true if time origin coincides with the moment when the RF pulse is applied (Note that after the 90° RF pulse, the magnetization vectors are in the x direction).

Until now only one 90° RF pulse is allowed [see assumption (c)]. From now on, the restriction on the RF pulse will be gradually released.

As a first step assume that there is one 180° RF pulse at time $T_e/2$ as in the spin echo pulse sequence. For this new case, the equation for the phase (Eq. 2.45) must be modified. Equation 2.45 is true until time $T_e/2$. Just after the RF pulse, the phase must be negated, i.e.:

$$\phi(t) = \begin{cases} \int_0^t \omega(t')dt' & \text{for } 0 < t < T_e/2 \\ -\int_0^{T_e/2} \omega(t')dt' + \int_{T_e/2}^t \omega(t')dt' & \text{for } t \geq T_e/2 \end{cases} \tag{2.47}$$

If there are more then one 180° RF pulses after the 90° RF pulse then the above equation must be divided into more sections because after each 180° RF pulse the phase must be negated. Let us define a function $\eta(t, t')$ which has a value 1 if the number of 180° RF pulses between time t' and t is even; else its value is -1. Using this function, the equation for phase may be simplified as:

$$\phi(t) = \int_0^t \omega(t')\eta(t, t')dt' \qquad \text{for } t > 0 \tag{2.48}$$

In magnetic resonance imaging usually one 90° RF pulse is not enough to obtain the data for the image reconstruction. Application of a train of 90° RF pulses is necessary. Each RF pulse may be numbered from $-N/2$ to $N/2 - 1$ where N is a positive even number. The time interval between the nth and $n+1$st 90° RF pulses is called the nth repetition interval and it is symbolized as $T_r[n]$. Although the repetition interval does not depend on n in most magnetic resonance imaging methods, the following formulations will be n dependent and it will cover all the special cases.

Let us define a relative time, τ, which is zero after each 90° RF pulse and increases until the next 90° RF pulse. Just after the new pulse the relative time becomes zero again. The actual time is defined with two parameters, $[\tau, n]$,

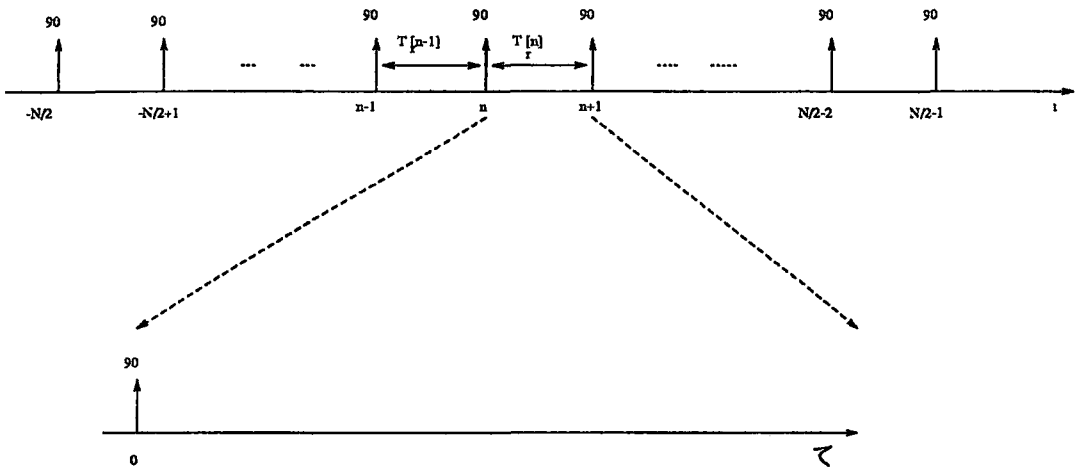

Figure 2.19: The description of the relative time concept. The absolute time is defined with respect to the 0th 90° RF pulse. On the other hand, the origin of the relative time is the starting point of the each repetition interval. In the figure, the nth repetition interval is shown in enlarged form.

where n is the RF pulse number, and τ is the relative time. Using this new time definition, one can write (See Figure 2.19):

$$t = [\tau, n] \stackrel{\text{def}}{=} \begin{cases} \tau + \sum_{i=0}^{n-1} T_r[i] & \text{for } n > 0 \\ \tau & \text{for } n = 0 \\ \tau - \sum_{i=n}^{-1} T_r[i] & \text{for } n < 0 \end{cases} \tag{2.49}$$

The trajectory of the magnetization vector will be the same as before if one assumes that

$$\min_n\{T_r[n]\} \gg \max\{T_1\} \tag{2.50}$$

For this case, the 90° RF pulses will tilt the magnetization vectors when applied in the steady state as before, so Eq. 2.46 will be valid with a little modification:

$$m([\tau, n]) = M_0 \exp(-\tau/T_2) \exp\left(j\phi([\tau, n])\right) \qquad \text{for } 0 < \tau < T_r[n] \tag{2.51}$$

where

$$\phi([\tau, n]) \;=\; \int_0^{\tau} \omega([\tau', n]) d\tau'$$

$$\omega(t) = \gamma h(t)$$

The combination of the above equation with Eq. 2.39 will give the relation between the steady state magnetization and the received MR signal:

$$s([\tau, n]) = W \int_{-D/2}^{D/2} \int_{ROI} M_0 \exp(-\tau/T_2) \exp\left(j\phi([\tau, n])\right) d\boldsymbol{x} \quad \text{for } 0 < \tau < T_r \tag{2.52}$$

The useful MR signal comes out in a very short interval. There will be no useful data outside this interval. This data is called *echo* or *FID* (Free Induction Decay). Assume the center of the echo is obtained at time T_e. Since t is very close to T_e, one may assume $\exp\left(-(\tau - T_e)/T_2\right)$ is equal to unity.

$$\exp(-\tau/T_2) = \exp(-T_e/T_2) \exp\left(-(\tau - T_e)/T_2\right) \approx \exp(-T_e/T_2) \tag{2.53}$$

With this assumption, the following relation can be written:

$$s([\tau, n]) = W \int_{-D/2}^{D/2} \int_{ROI} \rho(\boldsymbol{x}) \exp\left(j\phi([\tau, n])\right) d\boldsymbol{x} \qquad \text{for } \tau \approx T_e \tag{2.54}$$

where

$$\rho(\boldsymbol{x}) = M_0(\boldsymbol{x}) \exp(-T_e/T_2(\boldsymbol{x})) \tag{2.55}$$

The above equation is valid for a specific case. Here it is necessary to restate the assumptions which are used in the derivation of this equation:

a. A train of 90° and 180° RF pulses is applied.

b. All the RF pulses are slice selective, and they select the same slice which has a thickness of D.

c. All the magnetization vectors are at the steady state before the application of each 90° RF pulse.

Getting rid of the assumption (c) is also possible. The discussion will not be included here because it is pretty long and it is not necessary to know it to understand the rest of this dissertation. It must be stated that even if 90° RF pulses are applied when the magnetization vectors are not in the steady state,

the imaging equation (Eq. 2.54) will not change if the repetition rate of the pulses is constant but only the equation for ρ (Eq. 2.55) will be different. One should know that ρ is space dependent. And it is time invariant if the object is stationary during the data acquisition period.

The assumption (b) imposes a restriction on the shape of the RF pulses and the values of the gradients during the RF pulse application period. Since almost all pulse sequences which are used in the literature obeys this assumption, the restriction is not severe. In the 3-D imaging or some special applications, non selective RF pulses can be used. But this is a special case of the selective RF pulses because if one selects the slice thickness D as big as the size of the object, the selective RF pulse becomes a non-selective RF pulse, anyway.

The severe restriction of Eq. 2.54 is the assumption (a). Some new methods based on steady state free precession (SSFP) use RF pulses which have small tilt angles [22]. For such cases, it is not possible to explain the behavior of the magnetization vectors using Eq. 2.54. However the methods based on SSFP are not widely used in commercial MRI instruments. So, one can say that Eq. 2.54 is valid for almost all imaging methods.

2.2.4 Fourier Transform Imaging

The two-dimensional (2-D) Fourier Transform (FT) imaging is the most widely used MRI method. In this dissertation, only this imaging method will be considered. However, the extension to the other methods is possible.

In the FT method, the gradient and the RF pulses are arranged so that the uniform samples of $s(t)$ are the rectangular samples of the two dimensional Fourier transform of ρ. Therefore the imaging algorithm is very simple, after obtaining the rectangular samples from $s(t)$, the two dimensional (2-D) inverse FT will produce the ρ image.

In the FT imaging, the waveform shown in Figure 2.20 is repeated without any change except the y gradient. The shape of the waveform for the y gradient will be the same in each repetition but its amplitude will change. In the diagrams, usually the waveform of the gradients for a repetition interval is given. The

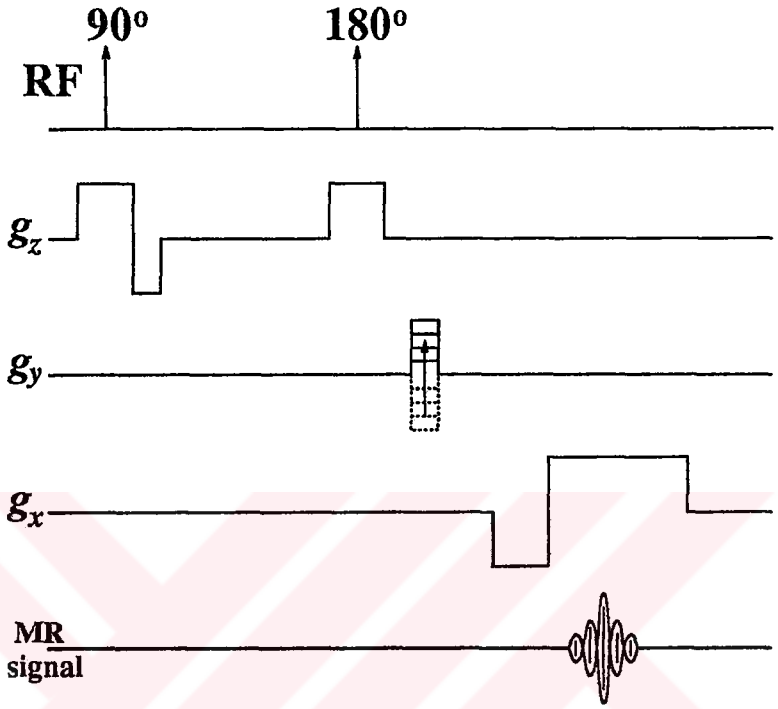

Figure 2.20: The standard FT MR imaging pulse sequence.

amplitude change in the y gradient is shown by an arrow as in Figure 2.20.

2.2.4.i Cancellation of the field inhomogenity

The pulse sequence shown in Figure 2.20 generates the spin echo at time $\tau = T_e$. In this sequence, there is a 90° RF pulse at time 0 and there is a 180° RF pulse at time $T_e/2$. With this pulse sequence the effect of the field inhomogenity is canceled at time $\tau = T_e$ and an echo appears.

Although the effect of the spin echo sequence is discussed verbally, it is possible to explain the phenomenon using the imaging equation. Let us combine the equations 2.2.3, and 2.48 and rewrite the expression for the phase in the imaging equation:

$$\phi([\tau, n]) = \gamma \int_0^{\tau} \left(\boldsymbol{g}^T([\tau', n])\boldsymbol{x} + H_i(\boldsymbol{x}) \right) \eta(\tau, \tau') d\tau' \tag{2.56}$$

Since the field inhomogenity is time independent, the equation reduces to the

following form:

$$\phi([\tau,n]) = \gamma \int_0^\tau \boldsymbol{g}^T([\tau',n])\eta(\tau,\tau')d\tau'\boldsymbol{x} + \gamma H_i(\boldsymbol{x}) \int_0^\tau \eta(\tau,\tau')d\tau' \tag{2.57}$$

If $\tau > T_e/2$, $\eta(\tau,\tau')$ will be:

$$\eta(\tau,\tau') = \begin{cases} -1 & \text{for } \tau' \in (0, T_e/2) \\ 1 & \text{for } \tau' \in (T_e/2, \tau) \end{cases} \tag{2.58}$$

Using this information, the second integral of Eq. 2.57 can be evaluated as:

$$\phi([\tau,n]) = \gamma \int_0^\tau \boldsymbol{g}^T([\tau',n])\eta(\tau,\tau')d\tau'\boldsymbol{x} + \gamma H_i(\boldsymbol{x})(\tau - T_e) \tag{2.59}$$

For $t \approx T_e$ (around the echo), the effect of the field inhomogenity will be canceled, and an approximate equation for the phase may be written as:

$$\phi(t) = \boldsymbol{G}^T(t)\boldsymbol{x} \tag{2.60}$$

where $\boldsymbol{G}$ is the phase gradient and it is defined as:

$$\boldsymbol{G}([\tau,n]) = \gamma \int_0^\tau \boldsymbol{g}([\tau',n])\eta(\tau,\tau')d\tau' \tag{2.61}$$

2.2.4.ii Slice selection

In the pulse sequence, the gradient $g_z(t)$ is designed so that there exists a non-zero gradient value when the RF pulses are applied, and

$$G_z([\tau,n]) = 0 \qquad \text{for } \tau \approx T_e \tag{2.62}$$

Therefore, the equation for ϕ can be simplified to get.

$$\phi(t) = G_x(t)x + G_y(t)y \tag{2.63}$$

where G_x, G_y and G_z are x, y and z components of the phase gradient $\boldsymbol{G}$. As it is seen in Eq. 2.63, the phase is independent form the space variable z. Therefore the imaging equation Eq. 2.54 can be modified as:

$$s([\tau,n]) = W \int_{ROI} \int_{-D/2}^{D/2} \rho(\boldsymbol{x})dz \exp\left(j\phi([\tau,n])\right) dxdy \qquad \text{for } \tau \approx T_e \tag{2.64}$$

In the 2-D MR imaging methods, it is common to assume that the proton density is uniform along the z direction in the selected slice:

$$\rho(\boldsymbol{x}_0) \approx \rho(\boldsymbol{x}) \qquad \text{for } z \in (-D/2, D/2) \tag{2.65}$$

where $\boldsymbol{x}_0 = [x, y, 0]^T$. This assumption is reasonable if the slice thickness is small enough. In the 2-D MR imaging, the slice thickness is usually in the range of 1cm to 0.5mm. In the microscopic MR imaging, the slice thickness reduces to the level of microns. So translational uniformity of the selected slice is not a bad assumption. In that case, the imaging equation becomes even simpler:

$$s([\tau, n]) = WD \int_{ROI} \rho(\boldsymbol{x}_0) \exp\left(jG_x x + jG_y y\right) dxdy \qquad \text{for } \tau \approx T_e. \tag{2.66}$$

To reduce the complexity of the notation, two dimensional vectors must be defined. Let $G_{(2)}$ and $\boldsymbol{x}_{(2)}$ be $[G_x, G_y]$ and $[x, y]$, respectively. And the proton density distribution at the $z = 0$ plane is defined as $\rho_{(2)}$. Using this notation the above imaging equation can be written as:

$$s([\tau, n]) = WD \iint \rho(\boldsymbol{x}_{(2)}) \exp\left(j\boldsymbol{G}_{(2)}^T \boldsymbol{x}_{(2)}\right) dxdy \qquad \text{for } \tau \approx T_e. \tag{2.67}$$

2.2.4.iii The Fourier transform relation between MR signal and ρ

It is interesting to observe that there is a FT relation between the MR signal and the proton density image for any MRI pulse sequence.

Let the continuous 2-D FT of $\rho(\boldsymbol{x})$[‡] be $P(\boldsymbol{\omega})$ where $\boldsymbol{\omega}$ is $[\omega_x, \omega_y]^T$. The relation can be written as:

$$\begin{aligned} P(\boldsymbol{\omega}) &= \mathcal{F}_{(2)}\{\rho(\boldsymbol{x})\} \\ &= \iint \rho(\boldsymbol{x}) \exp(-j\boldsymbol{\omega}^T \boldsymbol{x}) dxdy. \end{aligned} \tag{2.68}$$

Using the similarities of the equation 2.68 and 2.67 one can write the following important result.

$$s([\tau, n]) = WD\, P(-\boldsymbol{G}([\tau, n])) \qquad \text{for } \tau \approx T_e. \tag{2.69}$$

[‡]Here ρ and $\boldsymbol{x}$ are actually $\rho_{(2)}$ and $\boldsymbol{x}_{(2)}$. From now on the subscript (2) can be omitted when there is no possibility of confusion.

The above equation is the FT relation between the MR signal and the proton density, ρ.

2.2.4.iv Acquisition of the rectangular samples of P

As it can be seen in Eq. 2.69, if $\tau \approx T_e$ then the MR signal (s) will be equal to a point in P. The position of the point depends on the phase gradients G_x and G_y. As the time goes on, this point moves in the P space. While the point moves in the P domain, the samples of the MR signal can be acquired. In this way, the necessary samples of the P space can be obtained. Later these samples will be used to reconstruct the image.

In literature, there are many P space scanning methods. For example in the spiral scan, the P domain is scanned by a spiral trajectory of the P domain [23]. However, the most widely used scanning method is the raster scanning. In each repetition interval, only one horizontal line is scanned. By this way, it is very easy to obtain the rectangular samples on the P domain. And using the discrete FT of these samples the image of the proton density can be obtained.

Using the pulse sequence shown in Figure 2.20, the raster scan of P domain can be achieved. The characteristics of the x gradient waveform are:

- The waveform is the same in each repetition interval. In this way the lines are scanned exactly in the same manner.
- The amplitude of the gradient, Q_x, is constant during the data acquisition period. This property of the gradient makes the speed of the scan point constant.
- The waveform is arranged so that the phase gradient, G_x, is zero at the echo time. In this way, the center of the scan line is sampled at the echo time. Remember at the echo time the effect of the field inhomogenity is zero.

Using these rules, the phase gradient, G_x, can be calculated for $\tau \approx T_e$:

$$G_x([\tau, n]) = \gamma \int_0^{\tau} g_x(\tau')\eta(\tau, \tau')d\tau'$$

$$\begin{aligned} &= G_x([T_e, n]) + \gamma \int_{T_e}^{\tau} g_x(\tau')\eta(\tau, \tau')d\tau' \\ &= \gamma(\tau - T_e)Q_x \end{aligned} \tag{2.70}$$

On the other hand, some other rules for the y gradient are necessary. These can be stated as follows:

- The y gradient must be zero in during the data acquisition period
- In each repetition interval the value of G_y at the relative time T_e is an integer multiple of a constant number. In this way, the distance between each scan line will be constant.

Using these statements one can judge that the y gradient defines the vertical position of the horizontal lines. In most of the standard imaging methods the vertical position of each scan line increases in the y direction depending on the view number. The order of the position of the scan lines is not important if the object is stationary. In this chapter, the motion of the object during the data acquisition period is not considered. Because of this reason, the position of the scan lines is arbitrarily selected in the increasing order. In some other application which considers the motion of the object during the data acquisition period, the order of the position of the scan lines are different [24]. Assume that the amplitude of the y gradient waveform is increasing in each repetition interval as shown in Figure 2.20. For this special case, the phase gradient G_y can be calculated as:

$$\begin{aligned} G_y([\tau, n]) &= \gamma \int_0^{\tau} g_y(\tau')\eta(\tau, \tau')d\tau' \\ &= \gamma \frac{n}{N} t_y Q_y \end{aligned} \tag{2.71}$$

where $Q_y/2$ and t_y are the maximum amplitude and the period of the y gradient pulse, respectively, and N is the number of the repetition intervals in the total imaging period. It is important to note that G_y is τ independent but n dependent, for $\tau \approx T_e$.

As it can be seen from the above equations, the time parameter allows the scan of P in the horizontal direction. And in each repetition a new horizontal line

will be scanned. Therefore, the uniform samples of $s(t)$ correspond to rectangular samples of P.

2.2.4.v The MR image and the field of view

In the image reconstruction, the MR signal will be sampled and the discrete FT of the data will produce the desired discrete ρ image.

Let $s([\tau, n])$ be sampled at

$$\tau = \frac{m}{N} t_x + T_e \tag{2.72}$$

where m is an integer between $-N/2$ and $N/2 - 1$, and t_x is the sampling period. Therefore, the total sampling time in each repetition interval is t_x and the center of the sampling period is at the echo time. Thus the effect of the field inhomogenity is minimized.

An MR signal sample is defined with the numbers, n and m. When the sample (m, n) is acquired, the time will be $[\frac{m}{N} t_x + T_e, n]$, and the phase gradients at that time will be:

$$\begin{aligned} G_x([\frac{m}{N} t_x + T_e, n]) &= 2\pi \frac{m}{f_x} \\ G_y([\frac{m}{N} t_x + T_e, n]) &= 2\pi \frac{n}{f_y} \end{aligned} \tag{2.73}$$

where

$$\begin{aligned} f_x &= \frac{2\pi N}{\gamma t_x Q_x} \\ f_y &= \frac{2\pi N}{\gamma t_y Q_y} \end{aligned} \tag{2.74}$$

The parameters f_x and f_y are called the field of view.

Hence the relation between the MR signal samples and the P can be written as follows:

$$\begin{aligned} s_{k_y}(\frac{k_x}{N} t_x + T_e) &= WD\, P\Big(-\boldsymbol{G}\left([\frac{k_x}{N} t_x + T_e, k_y]\right)\Big) \\ &= WD\, P(\boldsymbol{\mathcal{V}k}) \end{aligned} \tag{2.75}$$

where

$$\boldsymbol{k} = [k_x, k_y]^T \tag{2.76}$$

and

$$\boldsymbol{\mathcal{V}} = \begin{bmatrix} \frac{2\pi}{f_x} & 0 \\ 0 & \frac{2\pi}{f_y} \end{bmatrix} \tag{2.77}$$

Here the matrix $\boldsymbol{\mathcal{V}}$ is called *the sampling matrix*. Let $P[k_x, k_y]$ be the samples of the $P(\omega_x, \omega_y)$:

$$P[\boldsymbol{k}] = WDP(\boldsymbol{\mathcal{V}}\boldsymbol{k}) \tag{2.78}$$

The inverse discrete Fourier transform (IDFT) of $P[\boldsymbol{k}]$ is a discrete image. The relation between the image and ρ can be found after some straightforward calculations:

$$\begin{aligned} IDFT(P[\boldsymbol{k}])[\boldsymbol{n}] &= \\ &\frac{1}{N^2} \sum_{k_x=-N/2}^{N/2} \sum_{k_y=-N/2}^{N/2} P[\boldsymbol{k}] \exp\left(j\frac{2\pi}{N}\boldsymbol{n}^T\boldsymbol{k}\right) \\ &= \frac{WD}{N^2} \sum_{k_x=-N/2}^{N/2} \sum_{k_y=-N/2}^{N/2} P\left(\boldsymbol{\mathcal{V}}\boldsymbol{k}\right) \exp\left(j\frac{2\pi}{N}\boldsymbol{n}^T\boldsymbol{k}\right) \\ &= \frac{WD}{N^2} \iint \rho(\boldsymbol{x}) \Gamma\left(\frac{n_x}{N} - \frac{x}{f_x}\right) \Gamma\left(\frac{n_y}{N} - \frac{y}{f_y}\right) dxdy \end{aligned} \tag{2.79}$$

where $\boldsymbol{n} = [n_x, n_y]^T$ and

$$\Gamma(v) = \sum_{k=-N/2}^{N/2-1} \exp\left(2\pi j k v\right) \tag{2.80}$$

Further simplification of the Γ function is possible:

$$\begin{aligned} \Gamma(v) &= \sum_{k=0}^{N-1} \cos\left(2\pi k v - \pi\frac{v}{N}\right) - j\sin(\pi\frac{v}{N}) \\ &= \operatorname{cotan}\left(\pi v\right)\sin(\pi v N) - j\sin(\pi v N) \end{aligned} \tag{2.81}$$

The Γ function is very similar to an impulse train (See Figure 2.21). The peaks can be observed at the integer values. For the large N values the Γ function may

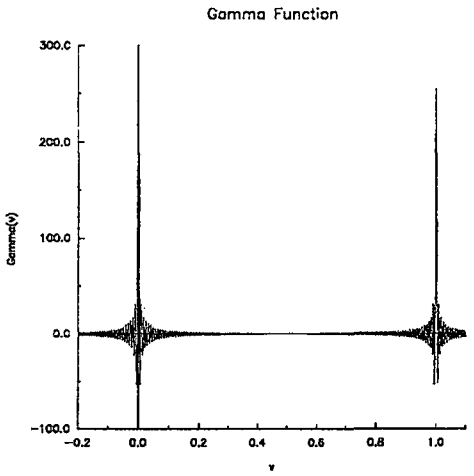

Figure 2.21: The plot of the Γ function for $N = 256$.

be approximated by:

$$\Gamma(v) \approx \sum_{l} \delta(v - l) \tag{2.82}$$

where δ is the impulse function. Using the sifting property of the impulse function, Eq. 2.79 may be simplified:

$$IDFT(P[\boldsymbol{k}])[\boldsymbol{n}] = \frac{WD}{N^2} \sum_{l_x} \sum_{l_y} \rho\Big((\frac{n_x}{N} - l_x)f_x, (\frac{n_y}{N} - l_y)f_y\Big) \tag{2.83}$$

If the ρ distribution is bounded in space, i.e.:

$$\rho(\boldsymbol{x}) = 0 \qquad \text{for } -f_x/2 > x \text{ or } x > f_x/2 \text{ or } -f_y/2 > y \text{ or } y < f_y/2 \tag{2.84}$$

then, the summation will have only one non-zero entry for $l_x = l_y = 0$. So, the desired solution can be obtained by letting l_x and l_y zero and killing the summations as:

$$IDFT(P[\boldsymbol{k}])[\boldsymbol{n}] = \frac{WD}{N^2} \rho\Big(\frac{n_x}{N} f_x, \frac{n_x}{N} f_y\Big) \tag{2.85}$$

If the object dimensions do not fit the bound given in Eq. 2.84, there will be aliasing.

Chapter 3

MOTION ARTIFACT SUPPRESSION METHODS: A LITERATURE SURVEY

In magnetic resonance imaging, the image degradation due to the motion of the body during the data acquisition period is an important problem. The data acquisition period is in the order of 10 minutes for the standard MR imaging methods. In this period there may be many kinds of physiological motion of the body: Heart beat, flow of the blood, and respiration are some of these. In addition to these types of motion, the leg, arm, eye, head and body may move. Although this is the case, it is common to assume that the object is stationary during the data acquisition period. Because of this reason the effect of the motion can be observed on the image. The image degradation due to motion of the body is called the motion artifact. The motion artifact usually appears as the ghost like replicas of the moving structure. In addition, the blurring effect of the motion can be observed. The motion artifact decreases the utility of the magnetic resonance images as a diagnostic tool.

There are various studies on the diagnostic quality of the images. In this chapter, a literature survey on the motion artifact reduction methods will be carried out. Since the number of the studies on the motion artifact suppression

methods is very high, all the magnetic resonance imaging motion artifact suppression methods can not be covered here. Instead, the ones that are most commonly used and related to the studies carried out in this dissertation will be summarized.

3.1 Motion Artifact Suppression using Motion Compensated Pulse Sequences

The studies on the motion artifact suppression methods are usually on finding specific imaging pulse sequences so that the effect of the motion on the acquired MR signal is minimized. By this way, the discrete FT of the MR signal samples will give motion artifact free (or reduced) images.

If the motion of the body is slow, it is acceptable to assume that the body stays still between the 90° RF pulse and the echo time[‡]. If this is the case, the body motion can be observed from one 90° RF pulse to another[‡]. This type of motion is called the view-to-view motion.

In all the view-to-view motion artifact suppression methods in the literature, the RF pulse application time is modified according to the motion. Some of these methods are presented below.

3.1.1 Gating

Gating is a very frequently used method [25]. Although it is based on a very simple idea, the motion suppression capability is very high [26],[27]. If a sinusoidal waveform is sampled at with the same frequency of the oscillation then the samples will be identical, and the fluctuation in the function can not be observed. In a similar way, when the heart image is required, if the data is sampled at the

[‡]This time interval can take different values depending on the used pulse sequence. It may be in the range of 5msec to 100msec.

[‡]The typical repetition time in the conventional imaging methods ranges from 300msec to 2.5sec

Figure 3.1: A typical ECG waveform. This ECG signal is supplied by the medical center of Middle East Technical University.

same phase of the heart (for example at the diastole), then the heart will seem to have no motion. The image obtained in this way belongs to this phase of the heart. Therefore, in the gating method, the T_r is selected so that it exactly matches with the period of the motion. In the case of quasi periodic motion, the repetition interval can be changed with the change of the period of the motion. There are two main gating methods: the electrocardiogram (ECG) gating, the respiratory gating.

The ECG gating is used in obtaining the image of the heart and the vessels. The ECG signal has a one-to-one relation with the heart motion and the motion of the blood in the vessels. A typical ECG signal is shown in Figure 3.1. At the peak of this waveform (R wave) the heart contracts (the systole). If one acquires the data at the same time with the occurrence of the R wave, then the image will belong the contracted heart.

The respiratory gating is used to suppress the motion artifact due to the respiratory motion of the body. The chest wall and liver as well as many other organs move with the effect of respiration. In the inspiration period, the motion is minimum. If one acquires the data in this period and suspends the data acquisition during the expiration, the motion of the chest will not be observed.

Although the method is very effective in the suppression of the motion artifact,

it has several disadvantages. First the data acquisition period increases. Longer data acquisition period means higher cost. The second disadvantage is that it restricts the RF pulse repetition interval. However, the duration of the repetition intervals may be changed to obtain different tissue contrast.

3.1.2 Respiratory Ordered Phase Encoding: ROPE

There are various ways of eliminating the ghost artifact by changing the acquisition order [28],[29]. Here, only the respiratory ordered phase encoding (ROPE)[24] will be explained.

It is known that the main reason of getting the image which has ghost artifact is the periodicity of the motion. If the motion were a non-periodic one, the ghost effect would not be observed. ROPE is a method which converts the periodic motion to a non periodic one.

In the standard FT imaging method, the amplitude of the y gradient increases one step after each repetition interval. Because of this reason, the data acquired in each repetition interval belongs to a different row. And the position of the row in the k-space moves towards to the positive direction as the time increases. But to get the rectangular samples on the k-domain it is not necessary to obtain the samples in the increasing order, instead the samples can be acquired in the mixed order. In the respiratory ordered phase encoding method, the acquisition order of the rows is arranged according to the motion of the body. Assume an object is moving sinusoidally as shown in Figure 3.2. If one gets the MR signal in the increasing order, the phase distortion in the k-domain will be sinusoidal. On the other hand, if one gets the k-domain rows in the mixed order as shown in Figure 3.2, and sort them, the periodic motion appears as a non-periodic motion. The phase distortion due to non-periodic motion cause blurring, but the ghost artifact on the image is removed.

3.2 Suppression of the Signals Generated by the Moving Structures

Another simple solution to the motion problem is the suppression of the outgoing signals from the moving structures [30]. This can be used in the imaging of the non-moving parts. In this method, firstly, the moving part of the body is selected by a highly selective RF pulse. This RF pulse does not select the stationary part of the body. The magnetization vectors of the moving structures fall in the transverse plane, while the others stay in their steady state condition. The gradient which is applied just after this selective RF pulse disperses the magnetization vectors in the transverse plane. By this way, the MR signal coming from the moving structures is suppressed. Using another 90° RF pulse, the standard imaging sequence starts. But the acquired signal will belong to only the stationary parts of the object.

Since there is no signal coming out from the moving structure, the motion artifact can not be observed. This simple and excellent idea finds its application if the position of the moving parts are known. To get this information, first an image which has the motion artifact must be acquired. Then after finding the place of the moving structure, this pulse sequence may be applied. This long procedure makes this method impractical.

3.3 The Gradient Moment Nulling: GMN

The gradient moment nulling [31] is a very effective method in suppression of the artifact due to the motion in the MR signal preparation period (i.e. the period between the 90° RF pulse and the echo time.) The motion in this period is called intraview motion. As opposed to gating and ROPE, GMN assumes that there is no motion between 90° RF pulses but there is motion in the MR signal preparation period. At first glance, this assumption seems to be an unrealistic one, but if one uses this method with the gating and ROPE at time same time, the artifact due to all kinds of motions (view-to-view and intraview motions) will

be suppressed.

In the gradient moment nulling, the protons are assumed to have constant velocity during the MR signal preparation period. It is a very good approximation because usually the acceleration of the protons is not enough to change their speeds considerably in this period. Under this assumption, it can be shown that if the first moments of the gradient waveforms are zero, the velocity of the protons will have no contribution to the MR signal. This fact is explained in the next section.

There are many studies on the comparison of GMN with the other methods [32],[33]. In their study, it is shown that GMN is very effective in the suppression of the intraview motion but it has no effect on the view-to-view motion.

3.4 Post Processing Methods

The motion artifact reduction studies explained above are concentrated on finding a new imaging pulse sequence. There is not much effort on the reduction of the artifact after the acquisition of the data. The main reason of this is the difficulty of the problem.

The motion artifact suppression techniques which are proposed in this dissertation are post-processing methods. Two new post-processing methods which are proposed by Haacke *et. al.* [34] and Mitsa *et. al.* [35] are closely related with the proposed methods. In all of these techniques, the MR data is assumed to be acquired using the standard MR imaging method. And then the data is processed to obtain the image of a static object. These methods will be discussed in Chapter 5.

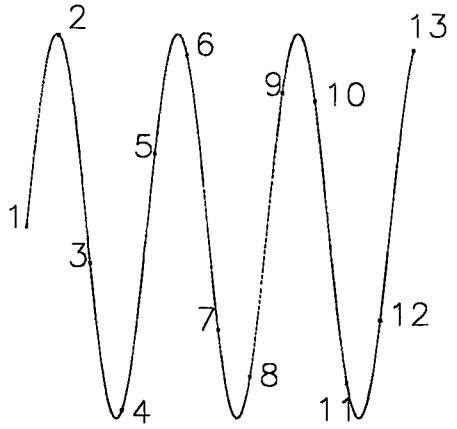

a) The data acquisition order for the standard imaging method.

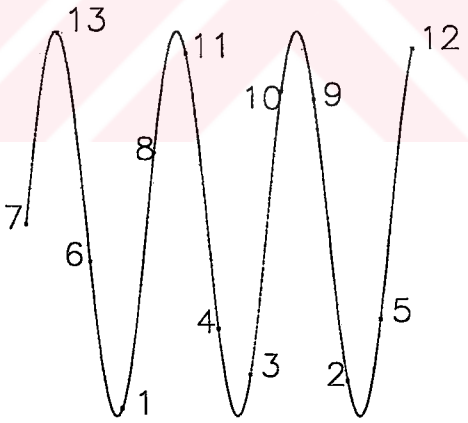

b) The data acquisition order for ROPE.

Figure 3.2: The data acquisition methods for the standard imaging and ROPE methods. The sinusoidal waveforms are the displacement functions of the chest wall during the data acquisition periods.

Chapter 4

THE EFFECT OF MOTION ON THE MR IMAGES

In the second chapter the basics of the magnetic resonance imaging are discussed assuming that the object is stationary during the data acquisition time. However, this assumption fails for *in vivo* magnetic resonance imaging. Many different kinds of motion may be observed. Therefore, the relation between the moving proton density distribution and the MR signal (the imaging equation) should be derived.

In this chapter, the effect of the motion of the body to the MR signal will be analyzed. The imaging equation for the moving body will be derived. Various motion types will be analyzed, and the effect of the translational, rotational and expansion/shrinkage motion will be formulated. And in the last section of the chapter, the appearance of the ghost artifact on the image will be interpreted.

4.1 The Imaging Equation for the Moving Body

Let the proton density be a function of both space and time:

$$\tilde{\rho} = \tilde{\rho}(\boldsymbol{x}; t) \tag{4.1}$$

where $\boldsymbol{x}$ is the space coordinate $[x, y, z]^T$. In the static imaging of a moving object a slice of the proton density distribution at an arbitrary time, say $t = 0$, will be monitored. Hence

$$\rho_s(x, y) \stackrel{\text{def}}{=} \tilde{\rho}(\boldsymbol{x}_0; 0) \tag{4.2}$$

where ρ_s is *the static proton density distribution* that we want to image, and $\boldsymbol{x}_0$ is $[x, y, 0]^T$.

The protons may move from one place to another but they can not be destroyed or generated. This very important conservation property will be the basis of all the following formulations. The proton motion can be shown by a trajectory vector. Every proton may have different trajectories. Since we are talking about the proton density distribution instead of the individual protons, the trajectory vector must be defined for an infinitesimal volume element. Consider an infinitesimal volume element at the position $\boldsymbol{x}$ at time t_0 and let $\boldsymbol{r}$ be its trajectory vector. At time t, the new position of the protons in this volume element can be found as:

$$\boldsymbol{r} = \boldsymbol{r}(t; \boldsymbol{x}, t_0) \tag{4.3}$$

$\boldsymbol{r}$ is the three dimensional trajectory vector whose components are r_x, r_y, and r_z. This may be treated as a time varying coordinate transformation. A rectangular grid shown in Figure 4.1 is transformed to a curve-linear coordinate system at time t.

Three important properties of this trajectory function will be used in the following paragraphs. The first one is the identity property of the function:

$$\boldsymbol{x} = \boldsymbol{r}(t; \boldsymbol{x}, t) \tag{4.4}$$

The above relation means that the position of a volume element does not change if time does not change, too. The second property of the function $\boldsymbol{r}$ is the transitivity: If

$$\boldsymbol{x}' = \boldsymbol{r}(t'; \boldsymbol{x}, t) \tag{4.5}$$

and,

$$\boldsymbol{x}'' = \boldsymbol{r}(t''; \boldsymbol{x}', t') \tag{4.6}$$

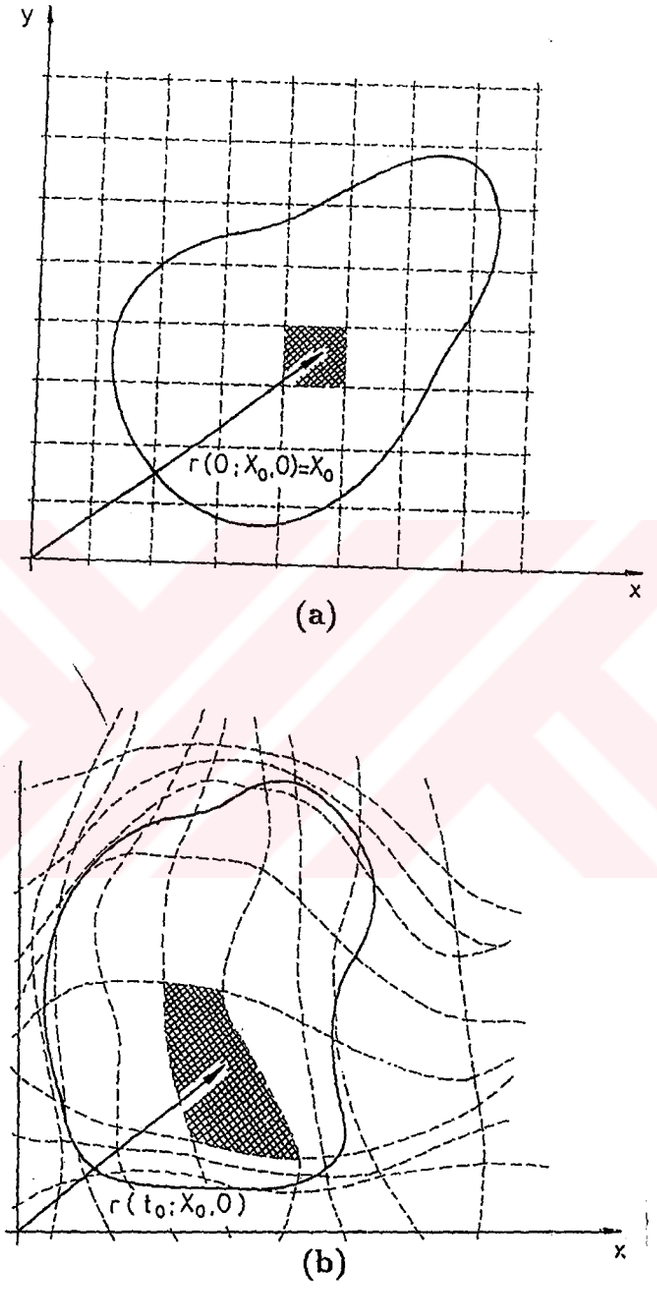

Figure 4.1: A time-varying proton density distribution. **(a)** The proton density distribution at time $t = 0$, $\tilde{\rho}(\boldsymbol{x}; 0)$. **(b)** The proton density distribution at time t, $\tilde{\rho}(\boldsymbol{x}; t)$. The shaded region shown in **(a)** lies at position $\boldsymbol{x}$. The protons in this region move to another position $\boldsymbol{r}(t; \boldsymbol{x}, 0)$ at time t. The new region covering these protons is the shaded region shown in **(b)**.

then

$$\boldsymbol{x}'' = \boldsymbol{r}(t''; \boldsymbol{x}, t) \tag{4.7}$$

The verbal explanation of the above relation is: If the protons inside a volume element moves from $\boldsymbol{x}$ to $\boldsymbol{x}'$ and continue their movement by altering the position to $\boldsymbol{x}''$, then one may forget about the intermediate position and say the protons inside the volume element moved from $\boldsymbol{x}$ to $\boldsymbol{x}''$. As a last property, if the position of the proton volume at the present time is known, its position at a previous and at a future time can be found using the trajectory vector. In other words $r(t'; \boldsymbol{x}, t)$ is defined for $t' > t$ and $t' < t$.

Let us find the phase of the magnetization of the protons which are at position $\boldsymbol{x}$ at time $[\tau, n]$. If the protons were stationary, then the phase would be found as (See Eq. 2.48):

$$\phi([\tau, n]; \boldsymbol{x}) = \gamma \int_0^{\tau} \left(H_i(\boldsymbol{x}) + \boldsymbol{g}(t)^T \boldsymbol{x}\right) \eta(\tau, \tau') d\tau' \tag{4.8}$$

where $H_i(\boldsymbol{x})$, $\boldsymbol{g}$ are the magnetic field inhomogenity and magnetic field gradient vectors, respectively; and $\phi(t; \boldsymbol{x})$ is the phase of the magnetization at the same place and time. But the protons are moving. In this case, Eq. 4.8 will be invalid. To find out the magnetic field that influences the phase of the magnetization, one should move with the proton volume and observe the effective field. Let us analyze the proton volume which is at position $\boldsymbol{x}$ at time $[\tau, n]$. At an earlier time, say $[\tau', n]$, the position of the same volume was $\boldsymbol{r}([\tau', n]; \boldsymbol{x}, [\tau, n])$. At that time the magnetic field that effects the protons in this volume element was:

$$H_i\left(\boldsymbol{r}([\tau', n]; \boldsymbol{x}, [\tau, n])\right) + \boldsymbol{g}(t)^T \boldsymbol{r}([\tau', n], \boldsymbol{x}, [\tau, n]) \tag{4.9}$$

and the angular velocity of these protons was:

$$\gamma \left(H_i\left(\boldsymbol{r}([\tau', n]; \boldsymbol{x}, [\tau, n])\right) + \boldsymbol{g}(t)^T \boldsymbol{r}([\tau', n], \boldsymbol{x}, [\tau, n])\right) \tag{4.10}$$

In addition, it is known that at time $[0, n]$ the phase of the magnetization is zero. Therefore, the phase at point $\boldsymbol{x}$ at time $[\tau, n]$ will not be as it is stated in Eq. 4.8 but:

$$\phi([\tau, n]; \boldsymbol{x}) = \gamma \int_0^{\tau} \left(H_i\left(\boldsymbol{r}([\tau', n]; \boldsymbol{x}, [\tau, n])\right) + \boldsymbol{g}(t)^T \boldsymbol{r}([\tau', n], \boldsymbol{x}, [\tau, n])\right) \eta(\tau, \tau') d\tau' \tag{4.11}$$

The last step before writing the imaging equation of the moving body is to find the RF weight function. In the previous chapter, it is shown that only the protons which are effected by the 90° RF pulses will have the contribution to the magnetic resonance signal. With this purpose a weight function w is defined (See Eq. 2.37). For the slice selective RF pulses, the function w has the value W in the selected slice and 0 elsewhere. In the case of moving body, the protons which were in the slice $-D/2 < z < D/2$ when the 90° RF pulse was applied may move to another position afterwards. In this new position (the position may be out of the selected slice), these protons will still have a contribution to the MR signal. Therefore, to check if there is any contribution of a proton to the MR signal, the position of the proton when the RF pulse is applied must be found. If at that time, the proton is in the $-D/2 < z < D/2$ slice it will have contribution, otherwise there will be no contribution from this proton to $s(t)$. So the weight function of the moving body is both time and space dependent. Using the above discussion, we may write the weight function, w, as:

$$w(\boldsymbol{x};[\tau,n]) = W\text{rect}\left(r_z([0,n];\boldsymbol{x},[\tau,n])/D\right) \tag{4.12}$$

where $\boldsymbol{r}([0,n];\boldsymbol{x},[\tau,n])$ is the position of the proton when the RF pulse is applied.

Using all the above information, one can immediately write the imaging equation of the moving object as:

$$s(t) = \int \tilde{\rho}(\boldsymbol{x};t)\exp\left(j\phi(t;\boldsymbol{x})\right)w(\boldsymbol{x};t)d\boldsymbol{x} \tag{4.13}$$

One can get rid of the function w by a change of variable. Let us replace $\boldsymbol{x}$ with $\boldsymbol{r}(t;\boldsymbol{x},[0,n])$:

$$\begin{aligned} s(t) \;=\; & \int \tilde{\rho}\left(\boldsymbol{r}(t;\boldsymbol{x},[0,n]);t\right) \\ & \exp\left(j\phi\left(t;\boldsymbol{r}(t;\boldsymbol{x},[0,n])\right)\right)w\left(\boldsymbol{r}\left(t;\boldsymbol{x},[0,n]\right);t\right)\mathcal{J}(t;\boldsymbol{x},[0,n])d\boldsymbol{x} \end{aligned} \tag{4.14}$$

where $\mathcal{J}$ is the Jacobian of $\boldsymbol{r}$ with respect to $\boldsymbol{x}$:

$$\mathcal{J} = \det\begin{bmatrix} \frac{\partial r_x}{\partial x} & \frac{\partial r_x}{\partial y} & \frac{\partial r_x}{\partial z} \\ \frac{\partial r_y}{\partial x} & \frac{\partial r_y}{\partial y} & \frac{\partial r_y}{\partial z} \\ \frac{\partial r_z}{\partial x} & \frac{\partial r_z}{\partial y} & \frac{\partial r_z}{\partial z} \end{bmatrix} \tag{4.15}$$

See [36] for further information on the Jacobian operator. To simplify the new form of the imaging equation, the terms in the integral will be analyzed term by term. Using the transitivity and the identity properties of $\boldsymbol{r}$ function one may simplify the weight function as:

$$\begin{aligned} w(\boldsymbol{r}(t;\boldsymbol{x},[0,n]);t) &= W\text{rect}\left(\frac{r_z([0,n];\boldsymbol{r}(t;\boldsymbol{x},[0,n]),t)}{D}\right) \\ &= W\text{rect}\left(\frac{r_z([0,n];x,[0,n])}{D}\right) \\ &= W\text{rect}(z/D) \end{aligned} \tag{4.16}$$

In the imaging equation 4.14, the $\tilde{\rho}\mathcal{J}$ product is equal to $\tilde{\rho}(\boldsymbol{x},[0,n])$. This equality can be proved as follows:

Assume an infinitesimal cubic volume element, which has a width of dx, a depth of dy and a height of dz, located at point $\boldsymbol{x}$. At time t', the protons inside this volume element is (See the shaded region in Figure 4.1.a):

$$\tilde{\rho}(\boldsymbol{x};t')d\boldsymbol{x} \tag{4.17}$$

where

$$d\boldsymbol{x} = dxdydz.$$

As the time goes these protons may move. The region which contains these protons may not be cubic. At time t, the position and the volume of this differential region will be $\boldsymbol{r}(t;\boldsymbol{x},t')$ and $\mathcal{J}(t;\boldsymbol{x},t')d\boldsymbol{x}$, respectively (See the shaded region in Figure 4.1.b).Therefore, the total number of the protons inside this new volume will be:

$$\tilde{\rho}(\boldsymbol{r}(t;\boldsymbol{x},t');t)\,\mathcal{J}(t;\boldsymbol{x},t')d\boldsymbol{x} \tag{4.18}$$

Since the number of protons is preserved, Eq. 4.17 and 4.18 must be equal. This equality gives the desired relation:

$$\tilde{\rho}(\boldsymbol{x};t') = \tilde{\rho}(\boldsymbol{r}(t;\boldsymbol{x},t');t)\,\mathcal{J}(t;\boldsymbol{x},t') \tag{4.19}$$

Using these simplifications, Eq. 4.14 can be written as:

$$s(t) = W\int_{-D/2}^{D/2}\iint \tilde{\rho}(\boldsymbol{x},[0,n])\exp(j\phi(t;\boldsymbol{r}(t;\boldsymbol{x},[0,n])))\,dxdydz \tag{4.20}$$

As it is done in obtaining the imaging equation of the stationary body, assume the proton density is uniform in the z-direction. This assumption will not cause any important problem if the slice thickness D is small enough. In other words,

$$\tilde{\rho}(\boldsymbol{x};[0,n]) \approx \tilde{\rho}(\boldsymbol{x}_0;[0,n]) \qquad \text{for } -D/2 < z < D/2 \tag{4.21}$$

where $\boldsymbol{x}_0 = (x, y, 0)$. In this case $\tilde{\rho}$ in Eq. 4.20 will be independent of z, so

$$s(t) = W \iint \tilde{\rho}\,(\boldsymbol{x},[0,n]) \left\{ \int_{-D/2}^{D/2} \exp\left(j\phi\left(t;\boldsymbol{r}(t;\boldsymbol{x},[0,n])\right)\right) dz \right\} dxdy \tag{4.22}$$

The above equation is a relation between the proton density distribution and the MR signal. But the distribution is time varying. Our final aim is to find a relation between the static proton density distribution and the MR signal. This result can not be obtained if the motion has no restrictions.

4.1.1 In-plane Motion of the Protons

Until now, there is no major assumption on the motion. Further simplification of the above equation for all kinds of motion is not possible. In this subsection, the motion in the selected plane, that is called *in-plane motion*, will be analyzed. In this type of motion, the excited protons (the protons whose magnetization vectors are tilted by the 90° RF pulses) are allowed to move within the selected slice, but they can never leave that slice. In other words, there is no motion along the z direction. Mathematically speaking,

$$r_z(t;\boldsymbol{x},0) = z \tag{4.23}$$

Remember $\boldsymbol{x} = [x, y, z]^T$. The in-plane motion can be observed in the respiratory motion (expansion/ shrinkage) of the chest, and the whole body motions (the translational and rotational motion). Under this restriction, the imaging equation (the relation between the static proton density distribution and the MR signal) can be found.

Let us return to Eq. 4.13:

$$s(t) = \int \tilde{\rho}(\boldsymbol{x};t) \exp\left(j\phi(t;\boldsymbol{x})\right) w(\boldsymbol{x};t) d\boldsymbol{x} \tag{4.24}$$

Changing the variable $\boldsymbol{x}$ with $\boldsymbol{r}(t;\boldsymbol{x},0)$, the following equation can be obtained:

$$s(t) = \int \tilde{\rho}\left(\boldsymbol{r}(t;\boldsymbol{x},0);t\right) \exp\left(j\phi\left(t;\boldsymbol{r}(t;\boldsymbol{x},0)\right)\right) w(\boldsymbol{r}\left(t;\boldsymbol{x},0\right);t)\, \mathcal{J}(t;\boldsymbol{x},\mathbf{0}) d\boldsymbol{x} \quad (4.25)$$

For the body which has only the in-plane motion w can be simplified as:

$$\begin{aligned} w(\boldsymbol{r}\left(t;\boldsymbol{x},0\right);t) &= W\text{rect}\left(\frac{r_z([0,n];\boldsymbol{r}(t;\boldsymbol{x},0),t)}{D}\right) \\ &= W\text{rect}\left(\frac{r_z([0,n];\boldsymbol{x},0)}{D}\right) \\ &= W\text{rect}(z/D) \end{aligned} \quad (4.26)$$

In the above simplification the transitivity property of $\boldsymbol{r}$ and Eq. 4.23 are used. With the same arguments used in the simplification of Eq. 4.13, the product $\tilde{\rho}\mathcal{J}$ term in Eq. 4.25 can be replaced by $\tilde{\rho}(\boldsymbol{x},0)$. And after same straight forward manipulations, the following result can be written:

$$s(t) = W \int_{-D/2}^{D/2} \iint \tilde{\rho}\left(\boldsymbol{x};0\right) \exp\left(j\phi\left(t;\boldsymbol{r}(t;\boldsymbol{x},0)\right)\right) d\boldsymbol{x}. \quad (4.27)$$

As in the previous cases, assume that the proton density distribution is independent of z within the selected slice. Therefore,

$$\tilde{\rho}(\boldsymbol{x};0) \approx \tilde{\rho}(\boldsymbol{x}_0;0) = \rho_s(x,y) \qquad \text{for } -D/2 < z < D/2. \quad (4.28)$$

Using the above equation and Eq. 4.27, the imaging equation which describes the in-plane motion case can be written as:

$$s(t) = W \iint \rho_s\left(x,y\right) \left\{ \int_{-D/2}^{D/2} \exp\left(j\phi\left(t;\boldsymbol{r}(t;\boldsymbol{x},0)\right)\right) dz \right\} dxdy. \quad (4.29)$$

4.1.2 Three Dimensional Motion of the Protons

The imaging equation for the moving object (See Eq. 4.29) has some restrictions: There must be no motion in the z direction and, the object must stay in the region of interest during its motion.

If there is motion in the z direction, after each 90° RF pulse a different set of protons will be selected. So, data in every data acquisition period will belong to

a different proton density distribution. Although this is the case, it is possible to write an imaging equation which is similar to Eq. 4.29 for a special case.

If we go back to the derivation of Eq. 4.29, the equation is obtained using the relation

$$r_z([0,n];\boldsymbol{x},0) = z \tag{4.30}$$

This statement is less restrictive then Eq. 4.23. Therefore the same imaging equation can be obtained if one allows the z motion at any time except $t \neq [0,n]$. It means the z motion is allowed only if the protons returns back to the selected slice before the next 90° RF pulse is applied. This funny motion becomes reality when the gated imaging technique is used [25]. In that technique, the RF pulses are applied when all the protons return back their original positions.

Using a simple argument, the imaging equation 4.29 can be made true for even less restrictive three dimensional motion. In this assumption, the main idea is that the MR signal need not be originated from the same protons. But the protons may be replaced by the others. This special motion case can be explained with an example. Assume that there is a constant blood flow along the z-direction, and there is no other kinds of motion. In this case, the proton density at a z plane will be stationary although there is a motion, because the outgoing blood from the selected slice is equal to the incoming blood (See Figure 4.2). Therefore, at any time the amount of blood in the selected plane will be the same. In the derivation of the imaging equation, Eq. 4.30 is used. But this equation is not true for the motion described here. To make it true, before the application of the 90° RF pulse the trajectory vector must point the replaced proton. And the new trajectory will be defined with respect to this new proton. As a result, if *outgoing protons are replaced by the incoming protons*, a new trajectory concept may be defined and Eq. 4.29 can be used as the imaging equation.

This pseudo three dimensional motion defined in this subsection is a special case of the true three dimensional motion, but still it is more general than the in-plane motion. And it is useful because it may be used in the formulation of the blood flow.

An important point should be clarified. The imaging equations for the moving

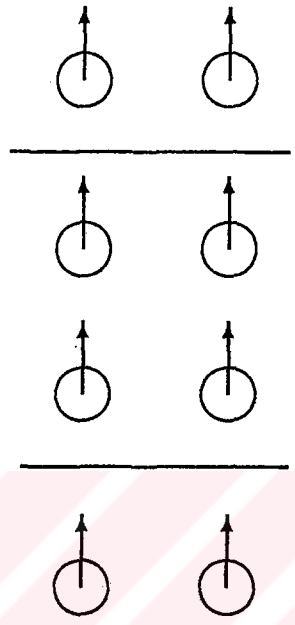

Figure 4.2: Protons moving along the z-direction. The outgoing protons must be replaced by the incoming ones.

object will not be correct if the motion is not bounded in the volume of interest (VOI). In the MRI instrument design, the RF coils generate uniform RF magnetic field in the VOI. The gradient coils generate linearly varying magnetic field in the same volume. But outside this volume, the linearity of the gradient field and the uniformity of the RF field are not guaranteed. Therefore, all the above discussion will fail if the object moves outside the volume of interest.

4.1.3 The Displacement Vector and the Undesired Component of the Imaging Equation

The imaging equation for the moving object can be converted into a very useful form using *the displacement vector*. This vector shows the amount of displacement

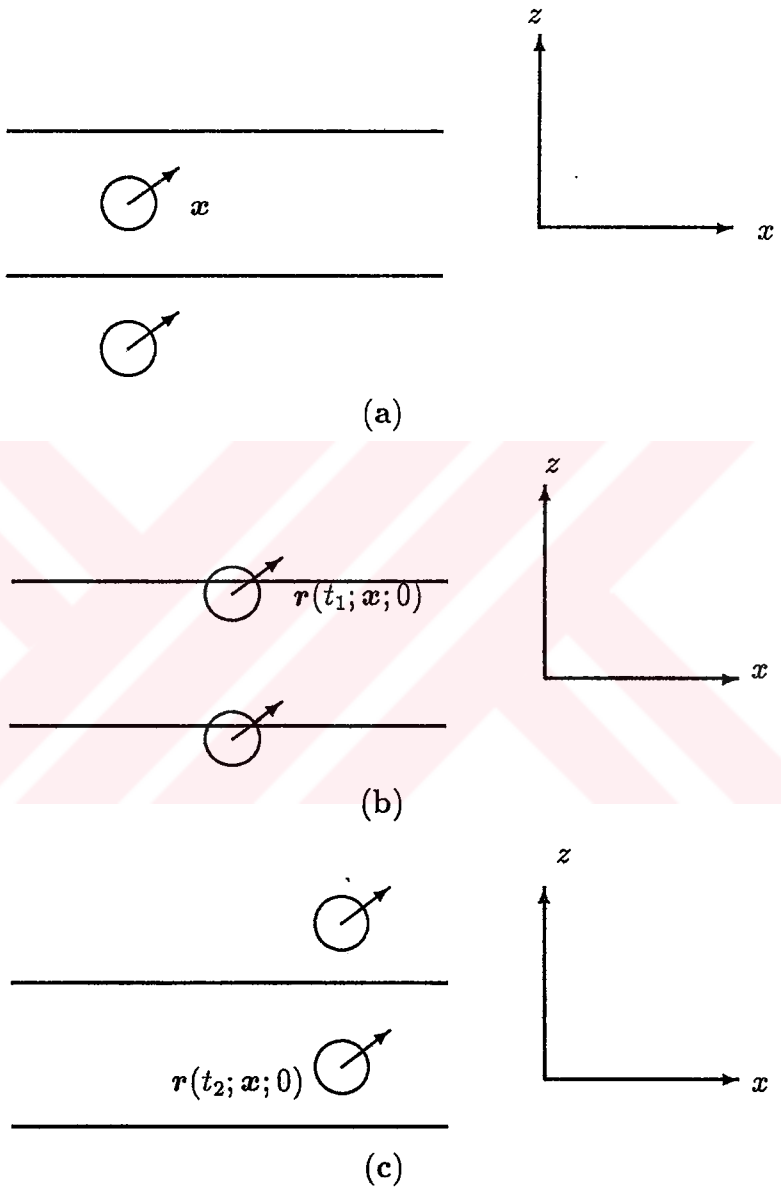

Figure 4.3: The trajectory of the moving protons at time (a) 0, (b) t_1, and (c) t_2. The trajectory vector of the moving protons shows the position of the protons as long as it stays in the selected plane (See (a) and (b)). But the protons leave the selected plane the trajectory vector points the position of the incoming proton [See (c)]

of the protons from their positions at time 0.

$$\boldsymbol{d}(t;\boldsymbol{x}) = \boldsymbol{r}(t;\boldsymbol{x},0) - \boldsymbol{x} \tag{4.31}$$

For a stationary object the displacement vector is 0. Using this new vector the integral term of the imaging equation 4.29 can be decomposed into the desired and undesired parts. Let us recall the definition of $\phi([\tau,n],\boldsymbol{x})$:

$$\phi([\tau,n];\boldsymbol{x}) = \gamma \int_0^\tau \left(H_i\left(\boldsymbol{r}([\tau',n];\boldsymbol{x},[\tau,n])\right) + \boldsymbol{g}(t)^T \boldsymbol{r}([\tau',n],\boldsymbol{x},[\tau,n])\right) \eta(\tau,\tau')d\tau' \tag{4.32}$$

In Eq. 4.29, the phase appears as $\phi\left(t;\boldsymbol{r}(t;\boldsymbol{x},0)\right)$. Using the transitivity property of $\boldsymbol{r}$ and above equation the following relation can be obtained:

$$\phi\left([\tau,n];\boldsymbol{r}([\tau,n];\boldsymbol{x},0)\right) = \gamma \int_0^\tau \left(H_i\left(\boldsymbol{r}([\tau',n];\boldsymbol{x},0)\right) + \boldsymbol{g}(t)^T \boldsymbol{r}([\tau',n],\boldsymbol{x},0)\right) \eta(\tau,\tau')d\tau' \tag{4.33}$$

The above equation can be decomposed into two parts as:

$$\phi\left(t;\boldsymbol{r}(t;\boldsymbol{x},0)\right) = \phi_d(t;\boldsymbol{x}) + \phi_u(t;\boldsymbol{x}) \tag{4.34}$$

where ϕ_d and ϕ_u are the desired and the undesired phases which are given as:

$$\phi_d([\tau,n];\boldsymbol{x}) = \gamma \left\{ \int_0^\tau \boldsymbol{g}^T([\tau',n])\eta(\tau,\tau')d\tau' \right\} \boldsymbol{x} \tag{4.35}$$

$$\begin{aligned} \phi_u([\tau,n];\boldsymbol{x}) &= \gamma \int_0^\tau \boldsymbol{g}^T([\tau',n])\boldsymbol{d}([\tau',n];\boldsymbol{x})\eta(\tau,\tau')d\tau' \\ &\quad + \gamma \int_0^\tau H_i\left(\boldsymbol{x} + \boldsymbol{d}([\tau',n];\boldsymbol{x})\right)\eta(\tau,\tau')d\tau' \end{aligned} \tag{4.36}$$

If there were no motion, d would be zero and therefore the undesired phase would be zero. The desired phase is independent of the motion. As it is in the analysis of the imaging equation for the stationary body (See Eq. 2.67), the desired phase is equal to:

$$\phi_d(t;\boldsymbol{x}) = G_x(t)x + G_y(t)y \qquad \text{for } \tau \approx T_e \tag{4.37}$$

Note that, ϕ_d is independent of z. Using this decomposition method one can rewrite the imaging equation of the moving object as:

$$s(t) = WD \iint \rho(\boldsymbol{x}_{(2)}) \exp\left(j\boldsymbol{g}^T\boldsymbol{x}\right) \lambda(t;\boldsymbol{x})dxdy. \tag{4.38}$$

where

$$\lambda(t;\boldsymbol{x}) = \frac{1}{D}\int_{-D/2}^{D/2} \exp\left(j\phi_u(t;\boldsymbol{x})\right) dz. \tag{4.39}$$

If there were no motion λ would be equal to unity.

If one samples the MR signal $s(t)$ as in the case of MR imaging of the stationary object, the relation between the MR samples and the proton density distribution will be as follows:

$$\tilde{P}[\boldsymbol{k}] = WD\iint \rho(\boldsymbol{x}) \exp\left(-j\boldsymbol{k}^T\mathcal{V}\boldsymbol{x}\right) \Lambda(\boldsymbol{k};\boldsymbol{x}) dxdy. \tag{4.40}$$

where

$$\Lambda(\boldsymbol{k};\boldsymbol{x}) = \lambda\left([k_x t_x/N + T_e, k_y], \boldsymbol{x}\right) \tag{4.41}$$

The above equation will be the basis of the artifact analysis due to the expansion/shrinkage, rotation and translation type of motions.

4.2 Intraview and View-to-view Motion

In the magnetic resonance imaging, usually data are acquired in bursts. The Fourier domain of the image (k-domain) is sampled on a line by line basis. After each 90° RF pulse, a line of the k-domain is sampled. The data acquisition time is very short compared to the 90° RF pulse repetition time.

The motion of the protons between the 90° RF pulse and the data acquisition is called *the intraview motion.* On the other hand the motion of the protons between the 90° RF pulses are called *the view-to-view motion.* In the view-to-view motion, the motion of the protons between the 90° RF pulse and the data acquisition period is ignored.

$$\boldsymbol{r}_v([\tau,n];\boldsymbol{x},0) = \boldsymbol{r}([0,n];\boldsymbol{x},0) \tag{4.42}$$

where $\boldsymbol{r}_v$ is the trajectory vector for the view-to-view motion. On the other hand, for the intraview motion, the proton distribution of the body is assumed to be the same after each 90° RF pulse, but the protons move in the data acquisition period:

$$\boldsymbol{r}_i([\tau,n];\boldsymbol{x},0) = \boldsymbol{r}([\tau,n];\boldsymbol{x};[0,n]) \tag{4.43}$$

These two kinds of motion have very different characteristics. But they usually appear at the same time. In a few special cases one of them may be ignored. At a first glance, one may think that the intraview motion can be ignored for slow motions. But the magnetic resonance imaging method is very sensitive to these type of motions. So one must be careful before ignoring it. On the other hand, if the respiratory and/or ECG gating is used, the view-to-view motion may be ignored. In the following subsections, these motions will be analyzed separately.

4.2.1 The View-to-view Motion

In this subsection, the intraview motion of the protons will be ignored and the imaging equation for the view-to-view motion will be derived.

The undesired phase was found in the previous section (See Eq. 4.36) as:

$$\begin{aligned}\phi_u([\tau,n];\boldsymbol{x}) &= \gamma\int_0^\tau \boldsymbol{g}^T([\tau' n])\boldsymbol{d}([\tau',n];\boldsymbol{x})\eta(\tau,\tau')d\tau' \\ &\quad +\gamma\int_0^\tau H_i\left(\boldsymbol{x}+\boldsymbol{d}([\tau',n];\boldsymbol{x})\right)\eta(\tau,\tau')d\tau' \end{aligned} \tag{4.44}$$

Since there is only view-to-view motion, then

$$\begin{aligned}\boldsymbol{r}_v([\tau,n];\boldsymbol{x},0) &= r_v([0,n];\boldsymbol{x},0) \\ \boldsymbol{d}([\tau,n];\boldsymbol{x}) &= d([0,n];\boldsymbol{x})\end{aligned} \tag{4.45}$$

Using these equations one may convert the undesired phase into the following form:

$$\begin{aligned}\phi_u([\tau,n];\boldsymbol{x}) &= \gamma\left\{\int_0^\tau \boldsymbol{g}^T([\tau',n])\eta(\tau,\tau')d\tau'\right\}\boldsymbol{d}\left([0,n];\boldsymbol{x}\right) \\ &\quad +H_i\left(r([0,n];\boldsymbol{x},0)\right)\int_0^\tau \eta(\tau,\tau')d\tau'\end{aligned} \tag{4.46}$$

As it is discussed for the no motion case, if $t \approx T_e$, the above equation can be simplified as:

$$\phi([\tau,n],\boldsymbol{x}) = d_x\left([0,n];\boldsymbol{x}\right)G_x([\tau,n]) + d_y\left([0,n];\boldsymbol{x}\right)G_y([\tau,n]) \tag{4.47}$$

(See Eq. 2.61 for the definition of G_x and G_y.) It is assumed that the proton density distribution along the z-direction is independent of z. This assumption is valid if the slice thickness is small enough. This argument may be extended to the displacement vector. So let us assume that d_x and d_y are independent of z. As a direct consequence of this assumption, ϕ is also independent of z:

$$\phi([\tau, n], \boldsymbol{x}) = d_x\left([0, n]; \boldsymbol{x}_0\right) G_x([\tau, n]) + d_y\left([0, n]; \boldsymbol{x}_0\right) G_y([\tau, n]) \tag{4.48}$$

Remember $\boldsymbol{x} = [x, y, z]^T$ and $\boldsymbol{x}_0 = [x, y, 0]^T$. This is a very important result because the z integral in Eq. 4.39 can be evaluated, and the undesired component for a body which has view-to-view motion becomes:

$$\lambda(t; \boldsymbol{x}) = \exp\left(j\phi(t; \boldsymbol{x})\right) \tag{4.49}$$

Actually, we do not need to be surprised with the above result. By the definition, there is no view-to-view z motion and for this analysis the intraview motion is ignored. Therefore, we do not have any z motion and the result is independent of z.

4.2.2 The Intraview Motion

In the previous subsection, the intraview motion is ignored and the imaging equation for view-to-view motion is formulated. In this subsection, the view-to-view motion will be ignored and the imaging equation for the intraview motion will be derived.

The basic assumption of the intraview motion is:

$$\boldsymbol{r}_i([0, n]; \boldsymbol{x}; 0) = \boldsymbol{x} \tag{4.50}$$

Here, $\boldsymbol{r}_i$ shows the trajectory of the motion of the protons between the time $[0, n]$ (the time when nth 90° RF pulse is applied) and $[\tau, n]$. The data will be collected around the echo time, T_e. Usually, the echo time is less than 200 milliseconds. Since the motion of the protons after collecting the data is not important, the effect of the intraview motion is seen in the interval of 200 milliseconds.

In most intraview motion artifact reduction methods [31], the velocity of the protons is assumed to be a constant between the time of the application of the 90° RF pulse and the echo. Actually, this is a realistic assumption. Surely, the protons have acceleration, and even time dependent acceleration. But this acceleration never reaches to a point that it can considerably change the speed of the protons in this short interval. Note that even though the velocities of the protons are not time independent, they may be space dependent. The protons in different places may have different velocities in different directions. The Taylor expansion of $\boldsymbol{r}$ with respect to the relative time τ can be written as:

$$\boldsymbol{r}_i([\tau, n]; \boldsymbol{x}; [0, n]) = \boldsymbol{x} + \tau \boldsymbol{v}(\boldsymbol{x}, n) + \text{Higher Order Terms} \tag{4.51}$$

where $\boldsymbol{v}$ is the velocity of the protons:

$$\boldsymbol{v}(\boldsymbol{x}, n) = \frac{d}{d\tau} \boldsymbol{r}_i([\tau, n]; \boldsymbol{x}, [0, n])\Big|_{\tau=0}$$

Here, the velocity of the protons are both space and n dependent, but it is independent of the relative time, τ. Here the higher order terms represent the acceleration, the velocity of the acceleration etc. of the protons.

Equation 4.51 can be written using the displacement vector as:

$$\boldsymbol{d}([\tau, n]; \boldsymbol{x}) = \tau \boldsymbol{v}(\boldsymbol{x}, n) + \text{Higher Order Terms} \tag{4.52}$$

If the higher order terms in Eq. 4.52 are ignored, the undesired phase term of the imaging equation 4.40 can be written as:

$$\phi_u([\tau, n]; \boldsymbol{x}) = \boldsymbol{g}_{(1)}^T(t) \boldsymbol{v}\,(\boldsymbol{x}, n) + \gamma \int_0^\tau H_i\left(\boldsymbol{x} + \tau \boldsymbol{v}([\tau', n]; \boldsymbol{x})\right) \eta(\tau, \tau') d\tau' \tag{4.53}$$

where

$$\boldsymbol{g}_{(i)}([\tau, n]) = \gamma \int_0^\tau \boldsymbol{g}([\tau, n]) \tau^i \eta(\tau, \tau') d\tau. \tag{4.54}$$

Here $G_{(i)}$ is the ith moment of the gradient vector. Since the field inhomogenity is a smooth function of space, H_i will not vary on the path of the protons:

$$H_i\left(\boldsymbol{x} + \boldsymbol{v}(\boldsymbol{x}, n)t\right) \approx H_i(\boldsymbol{x}) \tag{4.55}$$

Using this approximation, H_i is made independent of time, and the integral term of Eq. 4.53 will vanish as $t \approx T_e$, so:

$$\phi_u = \boldsymbol{g}_{(1)}^T(t)\boldsymbol{v}\,(\boldsymbol{x}, n) \tag{4.56}$$

The undesired phase, ϕ_u can be eliminated by just arranging gradients so that their first moments are zero around the echo time. In the literature, this undesired phase elimination method is called *the gradient moment nulling* (GMN) [31]. In the intraview motion studies it is shown that GMN is a very effective way of eliminating the motion artifact [32],[33].

If T_e is long so that the constant velocity assumption for the proton movement fails, the acceleration term may be added to the formulation. In this case, the second moments of the gradients must be nulled as well as their first moments.

4.3 Space Domain Analysis of the Motion

In the previous section, the motion of the body is categorized with respect to time. In that analysis the space dependence of the motion is arbitrary. In this section, the whole body (rotational and block) and expansion/shrinkage motions will be analyzed. Imaging equation for each specific case will be derived.

Before going into the details of the space domain analysis of the motion, let us summarize one important result of the previous section. In both view to view and intraview motion cases, the field inhomogenity has (almost) no contribution. If the field inhomogenity with respect to the space parameter $\boldsymbol{x}$ is a smooth function, then it is reasonable to assume that:

$$H_i\left(\boldsymbol{r}([\tau, n]; \boldsymbol{x}; 0)\right) \approx H_i\left(\boldsymbol{r}([0, n]; \boldsymbol{x}; 0)\right) \tag{4.57}$$

After this assumption, the contribution of the field inhomogenity to the undesired phase can be neglected for $\tau \approx T_e$:

$$\begin{aligned} \phi_u([\tau, n]; \boldsymbol{x}) \;=\; & \gamma \int_0^\tau \boldsymbol{g}^T([\tau' n])\boldsymbol{d}([\tau', n]; \boldsymbol{x})\eta(\tau, \tau')d\tau' \\ & + \gamma \int_0^\tau H_i\left(\boldsymbol{x} + \boldsymbol{d}([\tau', n]; \boldsymbol{x})\right)\eta(\tau, \tau')d\tau' \end{aligned}$$

$$
\begin{aligned}
&= \gamma \int_0^\tau \boldsymbol{g}^T([\tau' n])\boldsymbol{d}([\tau', n]; \boldsymbol{x})\eta(\tau, \tau')d\tau' \\
&\quad +\gamma H_i\left(\boldsymbol{x} + \boldsymbol{d}([0, n]; \boldsymbol{x})\right) \int_0^\tau \eta(\tau, \tau')d\tau' \\
&= \gamma \int_0^\tau \boldsymbol{g}^T([\tau' n])\boldsymbol{d}([\tau', n]; \boldsymbol{x})\eta(\tau, \tau')d\tau' \qquad (4.58)
\end{aligned}
$$

If the function $\boldsymbol{d}$ (proton displacement function) is a smooth function of space, then the Taylor expansion with respect to space variables will open a new direction for the analysis of the effect of the motion.

$$\boldsymbol{d}(t; \boldsymbol{x}) = \boldsymbol{d}(t; 0) + \mathcal{J}_0(t)\boldsymbol{x} + \boldsymbol{d}_{ho}(t; \boldsymbol{x}) \qquad (4.59)$$

where $\mathcal{J}_0$ is the Jacobian matrix of $\boldsymbol{d}$ with respect to space variable $\boldsymbol{x}$ which is evaluated at the origin (0):

$$\mathcal{J}_0(t) = \left.\frac{\partial \boldsymbol{d}}{\partial \boldsymbol{x}}\right|_{\boldsymbol{x}=0} = \det \left[\begin{array}{ccc} \frac{\partial d_x}{\partial x} & \frac{\partial d_x}{\partial y} & \frac{\partial d_x}{\partial z} \\ \frac{\partial d_y}{\partial x} & \frac{\partial d_y}{\partial y} & \frac{\partial d_y}{\partial z} \\ \frac{\partial d_z}{\partial x} & \frac{\partial d_z}{\partial y} & \frac{\partial d_z}{\partial z} \end{array}\right]_{(x,y,z)=(0,0,0)} \qquad (4.60)$$

and $\boldsymbol{d}_{ho}$ represents the higher order terms.

Ignoring the higher order terms in the Taylor expansion of the displacement corresponds to assuming that there are only block, linear expansion/shrinkage or rotational motions. In practice, pure block, expansion/shrinkage or rotational motions can not be observed. And in most cases it is impossible to ignore the higher order motion types. Although this is a fact, higher order motion types will be ignored. In the next chapter, the image reconstruction methods based on the following analysis will be derived, and, the effect of the higher order terms of the motion will be analyzed.

After assuming that the higher order terms are equal to zero, the undesired phase 4.58 can be modified as:

$$\phi_u(t; \boldsymbol{x}) = \gamma \int_0^\tau \boldsymbol{g}^T([\tau', n])\left(\boldsymbol{d}([\tau', n]; 0) + \mathcal{J}_0([\tau', n])\boldsymbol{x}\right)\eta(\tau, \tau')d\tau' \qquad (4.61)$$

Arranging the $\boldsymbol{x}$ dependent and independent terms yields the following result:

$$\phi_u(t; \boldsymbol{x}) = \phi_0(t) + \boldsymbol{\Delta G}(t)^T\boldsymbol{x} \qquad (4.62)$$

where ϕ_0 is the $\boldsymbol{x}$ independent phase, and $\boldsymbol{\Delta G}$ is the coefficient vector.

$$\begin{aligned}\phi_0([\tau,n]) &= \gamma\int_0^\tau \boldsymbol{g}([\tau',n])^T\boldsymbol{d}([\tau',n];0)\eta(\tau,\tau')d\tau' \\ \boldsymbol{\Delta G}([\tau,n]) &= \gamma\int_0^\tau \mathcal{J}_0([\tau',n])^T\boldsymbol{g}([\tau',n])\eta(\tau,\tau')d\tau' \end{aligned} \tag{4.63}$$

For this simple form of the undesired phase, ϕ_u, the integral of Eq. 4.39 can be easily evaluated. Let ΔG_x, ΔG_y, and ΔG_z be the first, second, and third elements of the vector $\boldsymbol{\Delta G}$, then

$$\begin{aligned}\lambda(t;\boldsymbol{x}) &= \frac{1}{D}\exp(j\phi_0)\exp(j\Delta G_x x + j\Delta G_y y)\int_{-D/2}^{D/2}\exp\left(j\Delta G_z z\right)dz \\ &= \exp(j\phi_0)\exp(j\Delta G_x x + j\Delta G_y y)\frac{sin(\Delta G_z D/2)}{\Delta G_z D/2}\end{aligned} \tag{4.64}$$

With these new variables, the imaging equation can be written as:

$$\begin{aligned}s(t) &= \zeta(t)\int\!\!\int \rho_s(x,y)\cdot \\ &\qquad \exp\left(j\left(G_x(t)+\Delta G_x(t)\right)x + j\left(G_y(t)+\Delta G_y(t)\right)y\right)dxdy\end{aligned} \tag{4.65}$$

where $\zeta(t)$ represents the phase and amplitude distortion:

$$\zeta(t) = WD\exp\left(j\phi_0(t)\right)\frac{sin(\Delta G_z(t)D/2)}{\Delta G_z(t)D/2} \tag{4.66}$$

If the MR signal is sampled using the conventional sampling method then the imaging equation turns into the following form:

$$\tilde{P}[\boldsymbol{k}] = \xi[\boldsymbol{k}]\int\!\!\int \rho_s(\boldsymbol{x})\exp\left(j(\boldsymbol{k}-\Delta\boldsymbol{k})^T\boldsymbol{\mathcal{V}}\boldsymbol{x}\right)dxdy \tag{4.67}$$

where

$$\Delta\boldsymbol{k} = -\frac{f_x}{2\pi}\Delta G_x([k_x t_x/N + T_e, k_y]) - \frac{f_y}{2\pi}\Delta G_y([k_x t_x/N + T_e, k_y]) \tag{4.68}$$

$$\xi[\boldsymbol{k}] = \zeta([k_x t_x/N + T_e, k_y]) \tag{4.69}$$

The above form of the imaging equation can be used in the reconstruction of the static image of a moving object. To obtain the above equation, the motion is linearized with respect to space variables. Note that in the above equation, the time dependence of the motion is arbitrary. In the following subsections, some special cases of the above formulation will be explained. In this way, the importance of the above formulation will be clarified.

4.3.1 Block Motion

If a body moves as a whole block along an arbitrary direction with any velocity, the motion of the body is called "*the block motion*". The block motion may be any function of time, the velocity and the direction of the motion may be time varying. The rotation of the block is not allowed. The rotational motion will be analyzed in another subsection. This type of motion may be observed as the conscious body motion. The leg, arm and head motions may be some examples of the block motions. The motion of the gradient coils can be treated as a block motion. The gradient coils are affected by the high magnetic field changes, they may vibrate or displace during the data acquisition period. Since the image of the body is acquired with respect to the frame defined by these coils, the motion of these coils is equivalent to the motion of the body in the reverse direction.

To visualize the effect of the block motion to the acquired MR signal a short discussion will be carried out (See Appendix B for an example). After this discussion, the mathematical background will be given.

In the static imaging of a moving object, our final aim is to find the proton density distribution at the $t = 0$. The sample of the MR signal at this time corresponds to a sample on the k-domain. However, at time t, there may be a shift in the position of the protons. From the properties of the FT it is known that if there is a shift in the space domain, then there will be a linear phase change in the k-domain. Therefore, the sample of the MR signal at time t corresponds to a phase distorted sample on the k-domain. The amount of phase distortion depends on the amount of shift.

In the above discussion, the effect of the block motion to the acquired MR signal during the MR signal preparation period (the intraview motion) is ignored. If this effect is included, a very similar result will be obtained. In the following formulation of the block motion both the intraview and view-to-view motions are considered.

For the block motion, the displacement vector $\boldsymbol{d}$ is independent from $\boldsymbol{x}$:

$$\boldsymbol{d}(t;\boldsymbol{x}) = \boldsymbol{b}(t) \tag{4.70}$$

And therefore, the Jacobian matrix, $\mathcal{J}_0$, is equal to zero. Since $\Delta \boldsymbol{k}$ is a linear function of $\mathcal{J}_0$, it will be zero, too. On the other hand, $\xi[\boldsymbol{k}]$ will have a contribution to the imaging equation:

$$\tilde{P}[\boldsymbol{k}] = \xi[\boldsymbol{k}] \iint \rho_s(\boldsymbol{x}) \exp\left(j\boldsymbol{k}^T \mathcal{V}\boldsymbol{x}\right) dxdy \tag{4.71}$$

where

$$\begin{aligned} \zeta([\tau, n]) &= WD \exp\left(j\gamma \int_0^\tau g([\tau', n])^T \boldsymbol{b}([\tau', n])\eta(\tau, \tau')d\tau'\right) \\ \xi[\boldsymbol{k}] &= \zeta([k_x t_x/N + T_e, k_y]) \end{aligned} \tag{4.72}$$

The integral in Eq. 4.71 gives the rectangular samples of the proton density distribution of the object:

$$\tilde{P}[\boldsymbol{k}] = \xi[k] P_s(\mathcal{V}\boldsymbol{k}) \tag{4.73}$$

Therefore, the block motion causes phase distortion on the imaging equation. The motion of the block may be along any direction, and there is almost no restriction on the trajectory of the motion (Only restriction is that the object must stay in the volume of interest).

The above formulation of the block motion includes the motion of the body along the z-direction. But one should be careful in using the equation along the z-direction, because the basic assumption of the z-motion: *The outgoing protons must be filled by the incoming ones.* For the block motion case, if there is a motion along the z-direction then the outgoing part of the block must be equal to the incoming part of the block. This corresponds to the uniformity of the body along the z direction. If the amplitude of the motion along the z-direction is low, then the assumption may be correct, but if the motion amplitude is high, the basic assumption will fail, and the imaging equation for the moving object must be in a completely different form.

4.3.2 In-plane Expansion/Shrinkage Motion

The subject of this subsection is the expansion/shrinkage motion of the body in the selected plane. This type of motion can be observed in the respiratory motion

of the chest. There are many studies on the respiratory motion [26],[27], but in most of them the motion is analyzed in the time domain and almost none of them utilizes the expansion/shrinkage behavior of the motion.

As in the previous subsection, first, the effect of the expansion/shrinkage will be discussed and after that the mathematical formulation of the motion will be given.

Again the FT relation between the MRI data and the proton density distribution will be used to explain the effect of this kind of motion. An expansion on the space domain corresponds to a shrinkage on the k-domain (Fourier transform domain), and similarly a shrinkage on the space domain corresponds to an expansion on the k-domain. Therefore if the object is expanded (or shrunk) then a sample will be acquired from the shrunk (or expanded) k-domain (See Figure 4.4). The position of a sample on the shrunk k-domain corresponds to another position in the k-domain of the static object. Because of these sample position shifts, the k-domain of the static object will be sampled non-rectangularly (See Appendix B for an example).

If the center of the expansion is not the origin, then the expansion/shrinkage motion may be decomposed to an expansion/shrinkage motion at the center and a block motion. Therefore, if the expansion/shrinkage motion is off-centered then there will be a phase distortion on the MRI sample as well as the sample position change.

The expansion/shrinkage motion will be formulated in the following paragraphs. The expansion of the body can be easily described using the displacement vector:

$$\boldsymbol{d}(t;\boldsymbol{x}) = \boldsymbol{\mathcal{A}}(t)\,(\boldsymbol{x}-\boldsymbol{c}) \tag{4.74}$$

where $\boldsymbol{c}$ is the center of expansion, and $\boldsymbol{\mathcal{A}}$ is the expansion/shrinkage percentage matrix:

$$\boldsymbol{\mathcal{A}}(t) = \begin{bmatrix} A_x(t) & 0 & 0 \\ 0 & A_y(t) & 0 \\ 0 & 0 & A_z(t) \end{bmatrix} \tag{4.75}$$

Here, A_x, A_y, and A_z are the percentage expansion/shrinkage factors along the

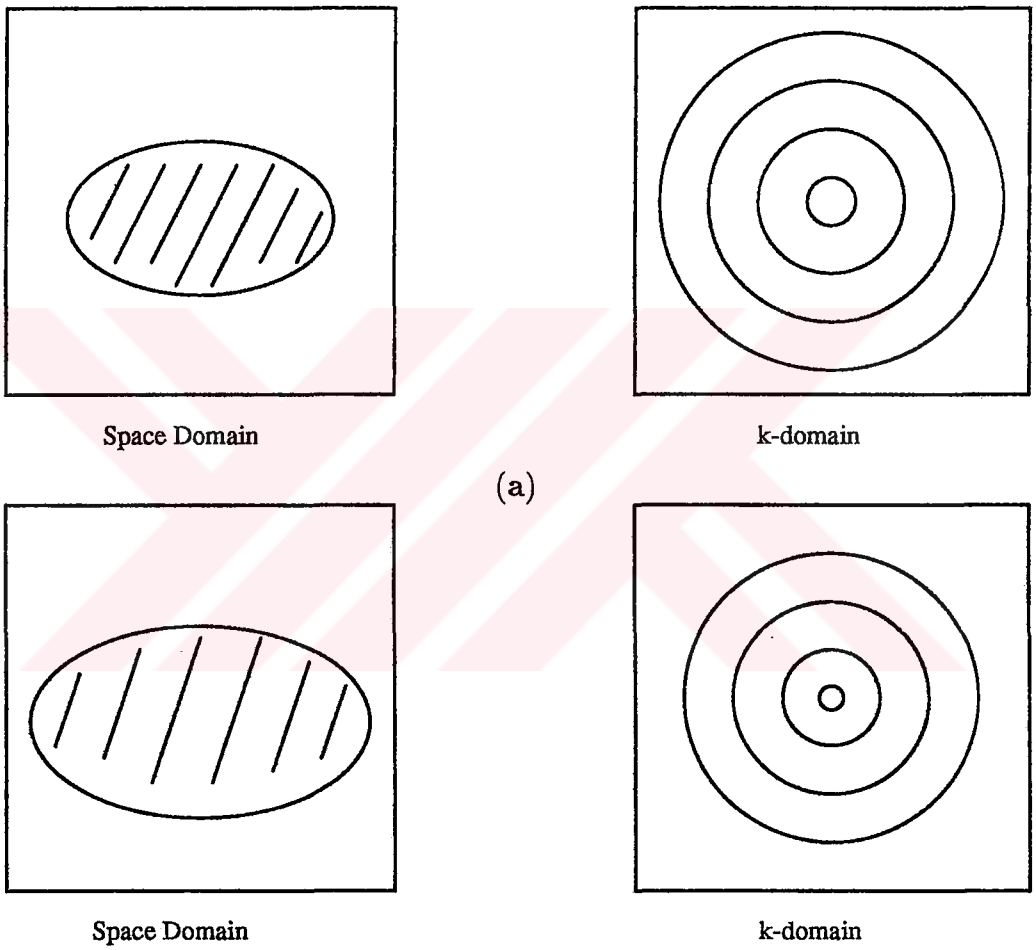

Figure 4.4: An expansion over the space domain corresponds to a shrinkage over the k-domain. (a) An elliptic object and its 2-dimensional Fourier transform. (b) The expanded version of the object and its Fourier transform.

x, y and z directions. For example, if A_x is equal to 0.10 then there is an expansion of 10% along the x-direction. To show the amount of shrinkage minus values of A_x must be used. For example, if A_y is equal to -0.05, a decrease of 5% will be observed in the height of the object. Since this discussion is on the in-plane expansion/shrinkage motion, the expansion/shrinkage factor along the z-direction (A_z) will be assumed to be equal to zero. The non-zero A_z case will be discussed in another subsection.

Comparing the expansion equation for the in-plane motion (Eq. 4.74) and Eq. 4.59 gives the following relations:

$$\begin{aligned} \boldsymbol{d}(t;0) &= -\boldsymbol{\mathcal{A}}(t)\boldsymbol{c} \\ \boldsymbol{\mathcal{J}}_0(t) &= \boldsymbol{\mathcal{A}}(t) \end{aligned} \tag{4.76}$$

Therefore, the imaging equation of a body which has the in-plane expansion/shrinkage motion will be in the form of Eq. 4.65 but since there is no motion along the z direction, the z motion related parts of the expansion/shrinkage motion will disappear:

$$s(t) = \zeta(t) \int\int \rho_s(\boldsymbol{x}) \exp\left(j\left(\boldsymbol{g}(t) + \boldsymbol{\Delta G}(t)\right)^T \boldsymbol{x}\right) dxdy \tag{4.77}$$

where

$$\begin{aligned} \boldsymbol{\Delta G}([\tau, n]) &= \gamma \int_0^{\tau} \boldsymbol{\mathcal{A}}([\tau', n])\boldsymbol{g}([\tau', n])\eta(\tau, \tau')d\tau' \\ \zeta(t) &= WD \exp\left(-j\boldsymbol{\Delta G}(t)^T \boldsymbol{c}\right) \end{aligned}$$

Using the FT sampling method (See Section 2.2.4), the relation between the MR signal samples and the continuous Fourier transform of the proton density distribution (k-domain) can be written as:

$$\tilde{P}[\boldsymbol{k}] = \exp\left(j\Delta \boldsymbol{k}^T \boldsymbol{\mathcal{V}} \boldsymbol{c}\right) P_s(\boldsymbol{\mathcal{V}}(\boldsymbol{k} - \Delta \boldsymbol{k})) \tag{4.78}$$

where

$$\Delta \boldsymbol{k} = \boldsymbol{\mathcal{V}}^{-1} \boldsymbol{\Delta G}\left([\frac{k_x}{N} t_x + T_e, k_y]\right) \tag{4.79}$$

The above formulation assumes that there is no motion along the z direction. The body has only the expansion/shrinkage type of motion, the amount of expansion/shrinkage and the center of the expansion can be any function of time.

As a conclusion, in the standard Fourier transform magnetic resonance imaging the acquired MR signal samples do not correspond to the rectangular samples over the k-domain, but to the non-rectangular ones. In addition, the samples will be phase distorted. If the center of expansion is at the center of the image, the non-rectangular samples will have no phase distortion.

4.3.3 Rotation of the Body

The rotational motion of a body in three dimension during the data acquisition period can be formulated. But here a very important point must be emphasized. When we are dealing with the three-dimensional motion, we should remember the basic assumption for the motion along the z-direction: *The incoming protons must be filled with the outgoing protons.* For the rotation around the x or y axes, if the rotating object has no circular symmetry around the rotation axis, the assumption will fail, and the discussion on the rotation will be wrong. The formulation may be a good approximation if the angle of the rotation is low enough. However, if the rotation axis is parallel to z then the motion will be an in-plane motion. Since there are no protons going out of or coming into the plane, the basic assumption will be true and the imaging equation for the rotation will be correct. Because of these facts, it is believed that the formulation for the rotational motion around the x and y axes are not useful. Although the formulation for the rotation around any axis can be done easily, only the rotation around the z axis will be considered.

In this analysis, the center of the rotation need not be the origin but it may be anywhere and even the position of this center may be time varying. In addition, the angular velocity of the rotation may also be time varying.

For the in-plane rotation, the trajectory vector can be written as:

$$\boldsymbol{r}(t;\boldsymbol{x},0) = \mathcal{R}_z\left(\beta(t)\right)(\boldsymbol{x}-\boldsymbol{c}) + \boldsymbol{c} \tag{4.80}$$

Here, $\mathcal{R}_z(\beta)$ is the three-dimensional rotation matrix which cause β radians rotation around the z-axis, and $\boldsymbol{c}$ is the center of the rotation. After some simple manipulations one can get the relation:

$$s(t) = \zeta(t) \int\int \rho_s(\boldsymbol{x}) \exp\left(j\boldsymbol{G}_r(t)^T\boldsymbol{x}\right) dxdy \tag{4.81}$$

where

$$\begin{aligned} \boldsymbol{G}_r([\tau, n]) &= \gamma \int_0^\tau \mathcal{R}\left(-\beta([\tau', n])\right) \boldsymbol{g}([\tau', n])\eta(\tau, \tau')d\tau' \\ \zeta(t) &= WD \exp\left(j(\boldsymbol{G}(t) - \boldsymbol{G}_r(t))^T\boldsymbol{c}\right) \end{aligned}$$

Therefore, the samples of the MR signal of a rotating object which has time varying angular velocity are the phase distorted non-rectangular sample of P_s as in the case of the expansion/shrinkage motion:

$$\tilde{P}[\boldsymbol{k}] = \xi[\boldsymbol{k}] P_s\left(\boldsymbol{\mathcal{V}}\boldsymbol{k}_r\right) dxdy \tag{4.82}$$

where

$$\xi[\boldsymbol{k}] = WD \exp\left(j(\boldsymbol{k} - \boldsymbol{k}_r)^T\boldsymbol{\mathcal{V}}\boldsymbol{c}\right) \tag{4.83}$$

where

$$\boldsymbol{k}_r[k_x, k_y] = \boldsymbol{\mathcal{V}}^{-1}\boldsymbol{G}_r([k_x t_x/N + T_e, k_y]) \tag{4.84}$$

If the center of rotation coincides with the center of the image, then there will be no phase distortion but the samples will still be acquired non-rectangularly. To visualize the effect of rotational motion see the example given in Appendix B.

4.3.4 The Expansion/Shrinkage Motion Along the z-direction

The expansion/shrinkage motion along the z-direction has a completely different effect on the imaging equation. The basic imaging equation which is derived for the moving object fails to explain the expansion/shrinkage motion along the z-direction, because in this equation it is assumed that *the number of the protons which are entering to the slice is equal to the number of the protons which are*

going out. But if there is expansion, the protons in the slice will be decreased and there will be some outgoing protons, but no incoming ones.

The effect of the z expansion/shrinkage motion is complex. To simplify the analysis, the intraview and view-to-view expansion/shrinkage motions are examined separately. In both cases, assume that there is expansion/shrinkage motion along the z-direction but there are no other kinds of motions, and the proton density is uniform along the z-direction.

4.3.4.i The intraview expansion/shrinkage motion along the z-direction

As a first step of the analysis of the z expansion/shrinkage motion, assume there is an expansion/shrinkage motion along the z-direction after a 90° RF pulse, but before the next 90° RF pulse all the protons return to their original positions. This strange motion can be observed in the respiratory gated data acquisition. In this method, the 90° RF pulse application time is synchronized with the respiratory motion. Therefore, at the time of application of each RF pulse, the protons are at the same positions. For this type of motion (intraview expansion/shrinkage motion along the z-direction), the imaging equation 4.65 is valid. The displacement vector can be written as follows:

$$\boldsymbol{d}(t, \boldsymbol{x}) = [0, 0, A_z(t)(z - c_z)]^T \tag{4.85}$$

where A_z and c_z are the percentage expansion factor and the center of expansion, respectively. From the definition of the intraview expansion/shrinkage motion, all the protons must return to their original positions after each 90° RF pulse, therefore:

$$A_z([0, n]) = 0 \qquad \text{for all } n. \tag{4.86}$$

For this condition, using the relation between Eq. 4.85 and Eq. 4.59, the imaging equation can be written as follows:

$$s(t) = \zeta(t) \int\int \rho_s(x, y) \exp\left(jG_x(t)x + jG_y(t)y\right) dxdy \tag{4.87}$$

where $\zeta(t)$ represents the phase and amplitude distortion,

$$\begin{aligned} \zeta(t) &= WD\frac{sin(\Delta G_z(t)d/2)}{\Delta G_z(t)d/2} \\ \Delta G_z([\tau,n]) &= \gamma\int_0^\tau g_z([\tau',n])A_z([\tau',n])\eta(\tau,\tau')d\tau' \end{aligned} \tag{4.88}$$

The above equation explains only the intraview part of the z expansion/shrinkage motion.

4.3.4.ii The view-to-view expansion/shrinkage motion along the z-direction

If there is a view-to-view expansion/shrinkage motion, the protons in the selected plane will be decreased/increased.

Assume a strip which has an infinitesimal volume in the selected plane whose height, width and length are D, dx, dy. If uniformity along the z direction is assumed then the protons inside this volume at time 0 (Remember $\rho_s(x,y)$ is the proton density on the $z=0$ plane at time 0, at any other time the proton density may change) is:

$$\rho(x,y)Ddxdy \tag{4.89}$$

If the object expands along the z-direction, then the number of the protons inside the volume decreases. If the displacement vector is given as:

$$d_z([\tau,n],\boldsymbol{x}) = A_z([0,n])\,(z-c_z) \tag{4.90}$$

then, at time t the height of the volume containing the same number of protons increases by A_z percent. Therefore, in the strip whose dimensions are $dx\times dy\times D$, the total number of the protons will be

$$\rho_s(x,y)\frac{D}{1+A_z([0,n])}dxdy \tag{4.91}$$

Therefore, the imaging equation for the expanding object along the z direction will be the same with the imaging equation for the static object except replacing $\rho_s Ddxdy$ by $\rho_s\frac{D}{1+A_z([0,n])}dxdy$:

$$s(t) = \zeta(t)\int\int \rho_s(x,y)\exp(jG_x(t)x + jG_y(t)y)dxdy \tag{4.92}$$

where

$$\zeta([\tau, n]) = \frac{DW}{1 + A_z([0, n])} \tag{4.93}$$

Note that in the above explanation of the expansion/shrinkage motion, the uniformity along the z direction is assumed. This assumption will be valid for a reasonable amount of expansion/shrinkage motion.

4.3.4.iii The view-to-view and intraview expansion/shrinkage motion along the z-direction

The imaging equation under both the intraview and the view-to-view expansion/shrinkage motion of the object can be formulated. The effect of the view-to-view motion is the change in the number of protons in the selected slice. The intraview motion is the motion of the protons after the 90° RF pulse is applied. Since there is also view-to-view motion, some amount of expansion when the 90° RF pulse is applied, (at time $[0, n]$), must be observed. For the intraview effect, the amount of expansion with respect to the original positions of the protons is not important but the amount of expansion after the application of the RF pulse must be considered.

Assume a strip which has a height of a unit length. At time $[0, n]$, its length will be $1 + A_z([0, n])$. At another time in the same repetition interval, say at time $[\tau, n]$ its length will be $1 + A_z([\tau, n])$. Therefore the relative expansion of the strip between time $[0, n]$ and $[\tau, n]$ is:

$$\begin{aligned} A'_z([\tau, n]) &= \frac{1 + A_z([\tau, n]}{1 + A_z([0, n])} - 1 \\ &= \frac{A_z([\tau, n]) - A_z([0, n])}{1 + A_z([0, n])} \end{aligned} \tag{4.94}$$

Using the new definition of the displacement along the z direction, the imaging equation can be written as:

$$s(t) = \zeta(t) \int\int \rho_s(x, y) \exp\left(j\boldsymbol{g}(t)^T \boldsymbol{x}\right) dxdy \tag{4.95}$$

where $\zeta(t)$ represents the phase and amplitude distortion,

$$\begin{aligned} \zeta(t) &= \frac{WD}{1+A_z([0,n])} \frac{sin(\Delta G_z(t)D/2)}{\Delta G_z(t)D/2} \\ \Delta G_z([\tau,n]) &= \gamma \int_0^\tau g_z([\tau',n]) A'_z([\tau',n]) \eta(\tau,\tau') d\tau' \end{aligned} \tag{4.96}$$

If the standard FT MR imaging pulse sequence is used, the relation between the k-domain of the proton density distribution and the samples of the MR signal will be the amplitude distorted samples of the k-domain:

$$\tilde{P}[\boldsymbol{k}] = \xi[\boldsymbol{k}] P_s(\boldsymbol{\mathcal{V}k}) \tag{4.97}$$

where

$$\xi[\boldsymbol{k}] = \frac{WD}{1+A_z([0,k])} \text{sinc}(\Delta k_z) \tag{4.98}$$

$$\Delta k_z = \frac{D}{2\pi} \Delta G_z([k_x t_x/N + T_e, k_y]) \tag{4.99}$$

4.4 The Effect of the Periodic Motion: The Ghost Artifact

Until now, the effect of the motion to the imaging equation is analyzed. Here, the effect of motion to the reconstructed images will be discussed.

In the standard imaging methods, the motion of the body is ignored and the image of moving body is reconstructed as if there is no motion. Because of this reason, the motion artifact on the reconstructed images appears These artifacts can be seen as the ghost-like replicas of the moving object. Mostly, the physiological motion of the body is quasi-periodic[‡]. And it is known that the periodicity of the motion is the actual source of the ghosts on the image.

Wood and Henkelman [37] gave a very good analysis of the problem. In their work, an impulse proton density distribution is considered. And they assumed that the impulse proton density distribution moves in x, y and z directions with

[‡]The quasi-periodicity means the periodicity of the motion may be violated for a short time, but in most of the time, the periodicity rule is satisfied.

a sinusoidal time function. They obtained the image of the moving object using the standard data acquisition method. And they showed that the ghost artifact on the image is related to the periodicity of the motion. In addition to the ghost artifact, there is blurring. The amount of blurring depends on the amplitude, and the direction of the motion. On the other hand the position of the ghost depends on the frequency of the oscillation.

In the following paragraphs, the effect of the motion for any periodic signal will be derived and the effect of the quasi-periodicity to the image will be shown.

4.4.1 The Effect of Motion to the Image

Since the motion of the protons is space dependent, the effect of the motion appears as a space dependent artifact. Because of this reason the analysis will be carried out assuming that there is a block motion. In other kinds of motions, the appearance of the motion artifact on the image is almost the same.

For the block motion, the relation between the MR signal samples and the proton density distribution was derived in a previous section as (See Eq. 4.73):

$$\tilde{P}[\boldsymbol{k}] = \xi[\boldsymbol{k}] P_s(\mathcal{V}\boldsymbol{k}) \tag{4.100}$$

and P_s is the continuous FT of ρ_s. As it is stated previously, using the conventional methods the image is obtained by taking the IDFT of these samples.

$$\tilde{I}[\boldsymbol{n}] = IDFT\left(\tilde{P}[\boldsymbol{k}]\right) \tag{4.101}$$

where I is the image which will have the motion artifact. The relation given in Eq. 4.100 can be used in the calculation of the IDFT.

$$\tilde{I}[\boldsymbol{n}] = WD \sum_{k_x=-N/2}^{N/2-1} \sum_{k_y=-N/2}^{N/2-1} \xi[\boldsymbol{k}] P_s(\mathcal{V}\boldsymbol{k}) \exp\left(j\frac{2\pi}{N}\boldsymbol{k}^T\boldsymbol{n}\right) \tag{4.102}$$

Since P is the continuous FT of ρ_s, one can rewrite the above equation in the following form:

$$\tilde{I}[\boldsymbol{n}] \;=\; WD \iint \rho_s(\boldsymbol{x}) \cdot$$

$$\left\{ \sum_{k_x=-N/2}^{N/2-1} \sum_{k_y=-N/2}^{N/2-1} \xi[\boldsymbol{k}] \exp\left(j\frac{2\pi}{N}\boldsymbol{k}^T\boldsymbol{n}\right) \exp\left(-j\boldsymbol{k}^T\mathcal{V}\boldsymbol{x}\right) \right\} dxdy \quad (4.103)$$

Let us define a new two dimensional continuous function:

$$\xi(\omega_x, \omega_y) = \zeta(\omega_x t_x/N + T_e + \omega_y T_r) \quad (4.104)$$

This function is the continuous version of the discrete function, $\xi[\boldsymbol{k}]$.

$$\begin{aligned} \xi[k_x, k_y] &= \zeta([k_x t_x/N + T_e, k_y]) \\ &= \zeta(k_x t_x/N + T_e + k_y T_r) \\ &= \xi(k_x, k_y) \end{aligned} \quad (4.105)$$

Let $\Xi[\boldsymbol{u}]$ be the continuous FT of $\xi(\boldsymbol{\omega})$:

$$\xi(\boldsymbol{\omega}) = \frac{1}{4\pi^2} \int\int \Xi(\boldsymbol{u}) \exp\left(j\boldsymbol{\omega}^T\boldsymbol{u}\right) du_x du_y \quad (4.106)$$

where $\boldsymbol{u}$ is equal to $[u_x, u_y]$. One can substitute the above equation into Eq. 4.103 and after some manipulation the following result can be obtained:

$$I[\boldsymbol{n}] = \frac{WD}{4\pi^2} \int\int \int\int \rho_s(\boldsymbol{x})\Xi(\boldsymbol{u})\Gamma(\frac{n_x}{N} - \frac{x}{f_x} + u_x)\Gamma(\frac{n_y}{N} - \frac{y}{f_y} + u_y)du_x du_y dxdy \quad (4.107)$$

where Γ is defined in Eq. 2.81. The above equation is basically the convolution of three functions. Γ function is related to the sampling method. It appears in the imaging equation of the stationary object, too. While N goes to infinity Γ can be approximated by an impulse train (See Figure 2.21):

$$\Gamma(u) \approx \sum_l \delta(u - l) \quad (4.108)$$

where $\delta(u)$ is the Dirac delta function. For large N values the above assumption is acceptable, if one substitutes the above equation to Eq. 4.107, the two integrals can be evaluated and finally the following result is obtained:

$$I[\boldsymbol{n}] = \frac{WD}{4\pi^2} \int\int \rho_s(\boldsymbol{x}) \left\{ \sum_{l_x} \sum_{l_y} \Xi\left(\frac{\mathcal{V}\boldsymbol{x}}{2\pi} - \frac{\boldsymbol{n}}{N} + \boldsymbol{l}\right) \right\} dxdy \quad (4.109)$$

where $\boldsymbol{l}$ is equal to $[l_x, l_y]$. The right hand side of the above equation is a convolution integral. The function Ξ becomes an impulse function in the case of MR imaging of a static object and therefore the summation turns out to be an impulse train function. The convolution integral will be killed by these impulses, and the relation between the proton density distribution and the image of the static object can be obtained. On the other hand, if the object is moving Ξ may be any arbitrary function. It is impossible to say something more on the behavior of the summation. However the motion of the human body is usually periodic. Therefore analysis of the periodic motions has a special importance.

4.4.2 The Artifact due to Periodic Motion

In the previous subsection, the effect of the block motion to the imaging equation is derived. In the following lines a special case of the motion: the periodic motion will be analyzed.

Since the complete derivation for the effect the periodic motion artifact is already done in [37], only the results will be discussed here.

Wood and Henkelman formulated a sinusoidal motion along the x direction:

$$b_x(t) = A sin(2\pi t/T_p + \theta_x) \tag{4.110}$$

where A, T_p, and θ_x are the amplitude, the period and the phase of the sinusoidal motion. After some calculations (all of the steps are shown in [37]), it can be shown that:

$$\Xi(\boldsymbol{x}) = \sum_m \exp(jm\theta_x) \left\{ \delta\left(x - \frac{t_x f_x m}{NT_p}\right) *_x B_m(x) \right\} \delta(y + m y_G) \tag{4.111}$$

where

$$y_G = \frac{T_r}{T_p} f_y$$

$$B_m(x) = \begin{cases} \frac{t_x f_x (-j)^m T_m(x/A)}{\pi N (A^2 - x^2)^{1/2}} & |x| < A \\ 0 & |x| > A \end{cases}$$

Here T_m represents the mth-order Chebyshev polynomial [38] and $*_x$ is the convolution operator with respect to the space variable x. The above complicated

equation is a very important result. First it shows that the moving object has ghost artifact in both x and y directions. The separation between the object and its first replica is y_G along the y direction and $\frac{t_x}{NT_p} f_x$ along the x direction. The replica of the image along the x direction can not be seen because the sampling period, t_x/N, is very short compared to the period of the motion. The replicas along the x direction overlaps and it appears as a blurring artifact. Another source of the blurring is the B_m function. The moving protons have an effect on their image which is very similar to the blurring effect of a moving light source to its photograph. The blurring effect of the protons can be seen only in the region of the movement. The intensity increases in the places where the protons stay more. The most important property of this type of motion is the ghost like replicas in the y-direction. The repetition time and the period of the motion are in the same order. So the separation between the image and its first replica is not a short distance. Actually, the ghost like replicas in the y-direction is the characteristic of the periodic motion.

If one analyses the MR images of the moving objects, some ghosts whose separations from the original image are not multiples of y_G can be seen. These ghost images appear as a result of the overlapping effect of the summation of Ξ. As it is already derived, the image of the moving object is the convolution of the static image with the summation of shifted Ξ functions (See Eq. 4.109). The intensity of the ghost decreases as the separation between the ghost and the object increases. The overlapping occurs for these low intensity ghosts.

The motion in the y and z directions has almost the same characteristic. The difference of the ghost artifact due to the motion in these directions can be seen in the blurring function. Since the path which protons are moving is different the effect is also different. In the x-motion, the blurring function, B_m, is non-zero only in a limited range in the x-direction. Although the derivation is not given here, the motion along the y-direction causes blurring along the y-direction.

Chapter 5

MOTION ARTIFACT FREE IMAGE RECONSTRUCTION ALGORITHMS

In the previous chapter the effect of the motion to the imaging equation is analyzed. The aim of this chapter is to explain some motion artifact reduction methods which are based on the space domain analysis.

5.1 The Block Motion

Reconstruction of an artifact free image of an object which has the block motion is relatively easy. Before taking the inverse discrete Fourier transform phase correction of the acquired MR signal samples is enough to obtain a good quality image.

To explain the way of evaluating the amount of phase distortion, let us rewrite 4.73:

$$\tilde{P}[\boldsymbol{k}] = \xi[\boldsymbol{k}] P_s(\mathcal{V}\boldsymbol{k}) \tag{5.1}$$

This is the relation between FT of the static proton density distribution and the acquired MR data when there is block motion. Here $\tilde{P}[\boldsymbol{k}]$ represents the acquired MR data set, $P_s(\boldsymbol{\omega})$ is the FT of the static proton density distribution and $\mathcal{V}$

is the sampling matrix which is defined in Section 2.2.4.v (See Eq. 2.77). In the above equation, $\xi[\boldsymbol{k}]$ stands for the phase distortion. Remember the phase distortion, $\xi[\boldsymbol{k}]$, is given as (See Eq. 4.72):

$$\xi[\boldsymbol{k}] = WD \exp\left(j\gamma \int_0^{k_x t_x/N+T_e} \boldsymbol{g}([\tau', n])^T \boldsymbol{b}([\tau', n])\eta(T_e, \tau')d\tau' \right) \tag{5.2}$$

In the above relation, $\boldsymbol{g}$, t_x, N, T_e, η, D, and W are the parameters related to the applied pulse sequence. Since the applied pulse sequence is known, all these parameters are known. $\boldsymbol{b}(t)$ represents the block motion (See Eq. 4.70). Therefore, if the function $\boldsymbol{b}(t)$ is known, the phase distortion, $\xi[\boldsymbol{k}]$ can be found by evaluating the above integral.

Using the calculated phase distortion and the acquired MR signal data set, the rectangular samples of the k-domain can be evaluated as:

$$P_s(\mathcal{V}\boldsymbol{k}) = \tilde{P}[\boldsymbol{k}]\xi^{-1}[\boldsymbol{k}] \tag{5.3}$$

And the motion artifact free image can be obtained by the calculating the inverse discrete Fourier transform of this calculated data.

There is no approximation in the reconstruction algorithm. So if the object motion exactly fits to the block motion model and if $\boldsymbol{b}(t)$ is exactly known then a perfect image reconstruction is possible. The above image reconstruction technique is applicable to the block motion with any function of time. A constant velocity block motion version of this reconstruction technique was previously proposed by Korin et al [39].

5.2 The In-plane Expansion/Shrinkage Motion

The in-plane expansion/shrinkage motion is observed in the transaxial chest imaging as a consequence of the respiratory motion. Although the motion of the chest is a non-linear function with respect to space, the expansion/shrinkage model for the motion is quite a good approximation.

There are some studies on the suppression of the respiratory motion artifact. Two of them are closely related to the reconstruction algorithm that will be explained in this section. Both of these works are carried out by the same group at the Case Western Reserve University ([40] and [34]).

In the first study [40], the in-plane expansion/shrinkage (they call the "*dilation*") motion artifact is reduced by changing the amplitudes of the x and y gradients depending on the amount of expansion. By this way, they obtained the rectangular samples of P_s, directly. This method is based on two assumptions: the expansion/shrinkage motion is a view-to-view motion, and the center of expansion is also the center of the image. Although the first assumption is a reasonable assumption, they could not suppress the motion artifact completely because of the misregistration of the center of expansion. Because of the difference between the center of expansion and the center of the image, the block motion artifact is observed. This will be explained in Section 5.2.3.ii.

In the second study [34], the in-plane expansion/shrinkage motion is reduced by an iterative post-processing method. Their method is based on the projection onto convex sets (POCS). This reconstruction method requires many iterations before converging to a motion artifact reduced image. Because of the computational cost of the method, it has no practical usage. However, their method can be used in any kind of non-linear motion although their sample solution is based on an expansion/shrinkage model.

The reconstruction algorithm which is developed in this dissertation is also a post-processing technique [41]. Since the method is not iterative the computational cost is much less than the POCS method.

5.2.1 The Reconstruction Algorithm

As it is shown in Eq. 4.78, the samples of the MR signal are the non-rectangular samples of the continuous Fourier transform of ρ. Furthermore, the phases of the samples are also distorted. The phase error of the samples are compensated using the equation

$$\overline{P[\boldsymbol{k}]} = \tilde{P}[\boldsymbol{k}] \exp(-j\Delta \boldsymbol{k}^T \boldsymbol{\mathcal{V}} \boldsymbol{c}) \tag{5.4}$$

Here the entries of $\overline{P[\boldsymbol{k}]}$ are the phase compensated versions of the samples of the MR signal, $\tilde{P}[\boldsymbol{k}]$. $\Delta\boldsymbol{k}$ is defined as (See Eq. 4.79):

$$\Delta\boldsymbol{k} = \gamma\mathcal{V}^{-1}\int_0^{k_x t_x/N+T_e} \mathcal{A}([\tau', k_y])\boldsymbol{g}([\tau', k_y])\eta(T_e, \tau')d\tau' \tag{5.5}$$

where $\mathcal{A}$ stands for the expansion/shrinkage percentage matrix and $\boldsymbol{c}$ is the center of expansion. Referring to Eq. 4.78 and 5.4, it is possible to write:

$$\overline{P[\boldsymbol{k}]} = P_s(\mathcal{V}(\boldsymbol{k} - \Delta\boldsymbol{k})) \tag{5.6}$$

Here the entries of $\overline{P[\boldsymbol{k}]}$ correspond to the non-rectangular samples of the Fourier transform of ρ. To reconstruct the image, it is necessary to recover the rectangular samples of P_s from its non-rectangular samples. The 2-dimensional discrete inverse Fourier transform of the recovered rectangular samples will be the motion artifact free image.

In the reconstruction method, the most difficult and the most important part is the recovery of the rectangular samples of the continuous Fourier transform of the image, P_s from its non-rectangular samples. This can be achieved by the some interpolation methods. In the following section, the interpolation methods will be explained.

5.2.2 The Interpolation Methods

The positions of the rectangular samples are not arbitrary. In almost all the imaging pulse sequences the y-gradient (g_y) is zero during each data acquisition period. In this period the x-gradient (g_x) has a non-zero value. For the no motion case, the acquired data in each acquisition period correspond to the samples of P_s on a straight line ($\omega_y = \omega_{y_0}$). Similarly if there is motion, the samples are taken on a straight line located at a different position and the samples on this line are taken non-uniformly.

This can be shown easily. The equation Eq. 4.68 can be written as:

$$\Delta k_x = \frac{2\pi\gamma}{f_x}\int_0^{k_x t_x/N+T_e} A_x([\tau', k_y])g_x([\tau', k_y])\eta(\tau, \tau')d\tau' \tag{5.7}$$

$$\Delta k_y = \frac{2\pi\gamma}{f_y}\int_0^{k_x t_x/N+T_e} A_y([\tau', k_y])g_y([\tau', k_y])\eta(\tau,\tau')d\tau' \tag{5.8}$$

Since there is no y-gradient and no 180° RF pulse during the data acquisition period, the above equation for Δk_y may be modified as:

$$\Delta k_y = \frac{2\pi\gamma}{f_y}\int_0^{T_e} A_y([\tau', k_y])g_y([\tau', k_y])\eta(\tau,\tau')d\tau' \tag{5.9}$$

As a result Δk_y is k_x independent.

$$\Delta k_x = \Delta k_x[k_x, k_y] \tag{5.10}$$

$$\Delta k_y = \Delta k_y[k_y] \tag{5.11}$$

Therefore the sample positions on P_s will look like as in Figure 5.1. Using this property, the recovery of the rectangular samples from the non-rectangular samples is reduced to two one dimensional problems. First, for each k_y, a one-dimensional signal is defined as:

$$P_x^{(k_y)}(\omega_x) = P_s\left(\omega_x, \frac{2\pi}{f_y}(k_y + \Delta k_y)\right) \tag{5.12}$$

This new signal is the FT of the proton density distribution at line $\omega_y = \frac{2\pi}{f_y}(k_y + \Delta k_y)$. At the k_y'th repetition interval, the samples are acquired on this line non-uniformly:

$$\overline{P[k_x, k_y]} = P_x^{(k_y)}\left(\frac{2\pi}{f_x}(k_x + \Delta k_x)\right) \tag{5.13}$$

where $\tilde{P}[\boldsymbol{k}]$ stands for the acquired MR data set. Note that, if the above two equations are combined Eq. 5.6 can be obtained.

The first one-dimensional problem is the recovery of the rectangular samples of $P_x^{(k_y)}(\omega_x)$ from its non-uniform samples. The non-uniform samples are located at

$$\omega_x = \frac{2\pi}{f_x}(k_x + \Delta k_x)$$

The uniform samples at the positions

$$\omega_x = \frac{2\pi}{f_x}k_x$$

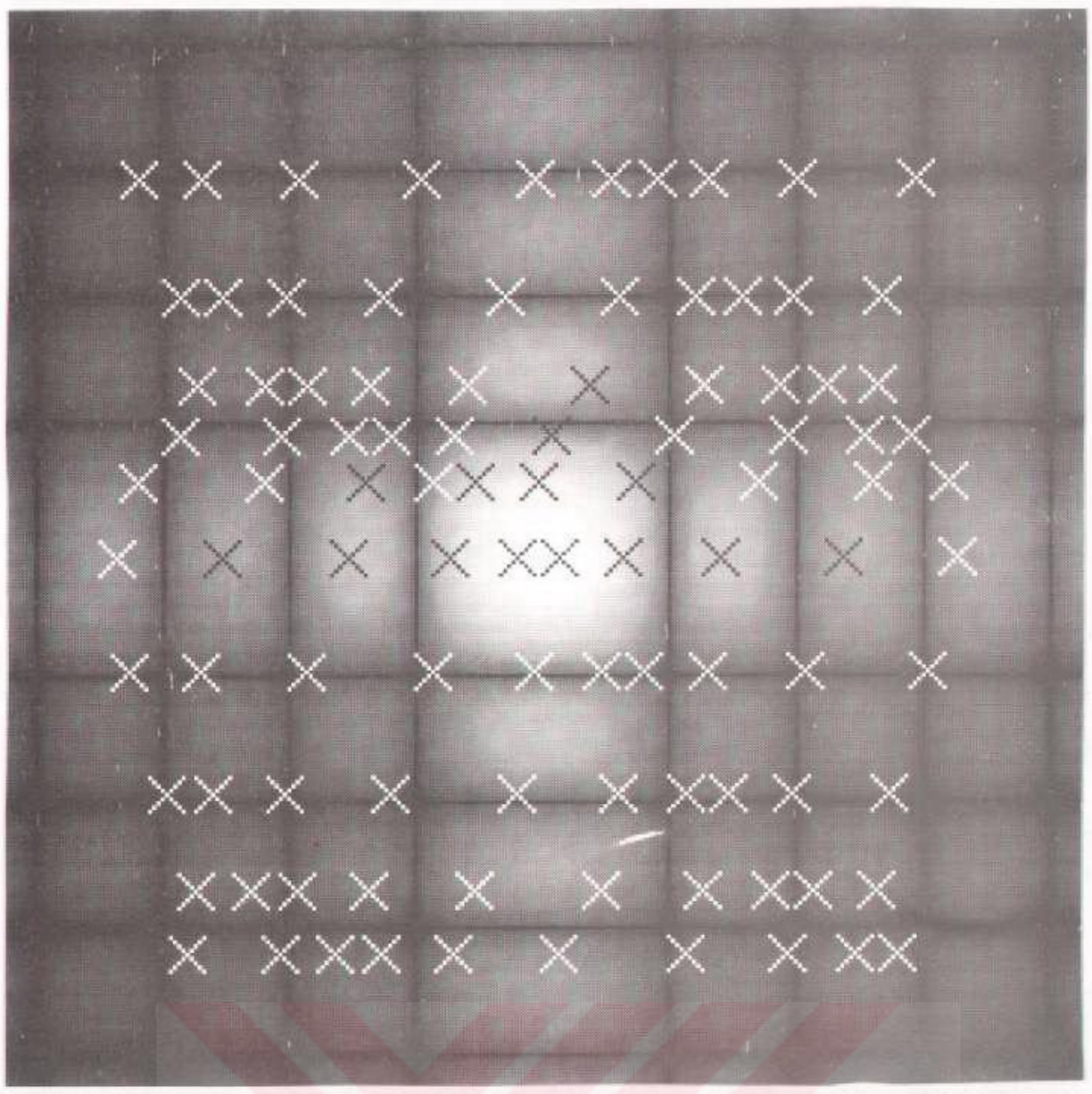

5.1: A sample distribution of the non-rectangular sample positions in ω_x, ω_y) plane. In this example there are 10 repetition intervals and in each on 10 samples are acquired. The positions of the samples are marked by ns. The positions of samples acquired in each repetition interval lie on a al line. This type of sampling is the result of the respiratory motion.

alculated using one dimensional interpolation methods. After the interpo- $P_x^{(k_y)}(\frac{2\pi}{f_x}k_x)$ are evaluated. These values correspond to $P_s\left(\frac{2\pi}{f_x}k_x, \frac{2\pi}{f_x}(k_y + \Delta k_y)\right)$. r this step, the second one-dimensional problem must be solved. For each her one-dimensional signal is defined.

$$P_y^{(k_x)}(\omega_y) = P_s\left(\frac{2\pi}{f_x}k_x, \omega_y\right) \tag{5.14}$$

$P_y^{(k_x)}(\omega_y)$ corresponds to a vertical line on the k-domain. After the previous interpolation, some non-uniform samples of $P_y^{(k_x)}$ are evaluated. These samples are at the positions $\frac{2\pi}{f_y}(k_y + \Delta k_y)$. Using the interpolation, the uniform samples at $\frac{2\pi}{f_y}k_y$ can be calculated. These uniform samples of $P_y^{(k_x)}(\omega_y)$ correspond to

the rectangular samples of P_s. Therefore the two-dimensional non-rectangular to rectangular sample conversion problem can be solved by solving two one-dimensional interpolation problems.

There are many studies on one-dimensional non-uniform sampling. In 1956, Yen proved that the recovery of a bandlimited signal form its non-uniform samples is possible if there are sufficient number of data [42]. Both $P_y^{(k_x)}(\omega_y)$ and $P_x^{(k_y)}(\omega_x)$ satisfy the requirement because P_s is the Fourier transform of a space limited signal. Here, a method for the recovery of the uniform samples of $P_y^{(k_x)}(\omega_y)$ from its non-uniform samples will be introduced. The uniform samples of $P_x^{(k_y)}(\omega_x)$ can be obtained in the same manner.

Using the sinc interpolation, $P_y^{(k_x)}(\omega_y)$ can be recovered from its uniform samples as [43]:

$$P_y^{(k_x)}(\omega_y) = \sum_k P_y^{(k_x)}(\frac{2\pi}{f_y}k)\text{sinc}\left(\frac{f_y\omega_y}{2\pi} - k\right) \tag{5.15}$$

The above summation is defined for all integer k values. But $P_y^{(k_x)}(\frac{2\pi}{f_y}k)$ is assumed to be zero for $k \notin [-\frac{N}{2}, \frac{N}{2})$ for some N. It is enough to carry out the summation for the non-zero k values. But $P_y^{(k_x)}(\omega_y)$ is sampled non-uniformly at the instances $\frac{2\pi}{f_y}(k_y + \Delta k_y)$. Therefore the relation between the non-uniform samples and the uniform samples can be written as:

$$P_y^{(k_x)}\left(\frac{2\pi}{f_y}(k_y + \Delta k_y)\right) = \sum_{k\in[-\frac{N}{2},\frac{N}{2})} P_y^{(k_x)}(\frac{2\pi}{f_y}k)\text{sinc}(k_y + \Delta k_y - k) \tag{5.16}$$

The above equation can be converted to matrix form as:

$$\vec{P}_y^{(k_x)}(k_y + \Delta k_y) = \mathcal{S}\vec{P}_y^{(k_x)}(k) \tag{5.17}$$

where $\vec{P}_y^{(k_x)}(k_y + \Delta k_y)$ and $\vec{P}_y^{(k_x)}(k)$ are the non-uniform and the uniform sample vectors, and $\mathcal{S}$ is the transformation matrix. The elements of the matrix are $\text{sinc}(k_y + \Delta k_y - k)$ where k is the column and k_y is the row.

To calculate the uniform samples from the non-uniform samples the matrix $\mathcal{S}$ must be inverted.

$$\vec{P}_y^{(k_x)}(k) = \mathcal{S}^{-1}\vec{P}_y^{(k_x)}(k_y + \Delta k_y) \tag{5.18}$$

If the number of non-uniform samples are equal to the number of the rectangular samples then the $\mathcal{S}$ matrix will be a square alternant matrix. And after some mathematical manipulations it can be proved that the $\mathcal{S}$ matrix is invertible for any set of distinct $k_y + \Delta k_y$'s [44].

The matrix $\mathcal{S}$ may be practically singular if some non-uniform samples are too close to each other or if there is no sample around a uniform sample location. Unfortunately, this occurs frequently. To overcome this problem the well-known singular value decomposition method is used and the uniform samples are calculated by multiplication of the pseudo inverse of $\mathcal{S}$ with the non-uniform sample vector. See rf. [45] for the details of the singular value decomposition and the pseudo inversion.

Instead of solving the problem by the pseudo inversion of the matrix, some approximate methods may be proposed. The linear and the third order Lagrange, and cubic spline interpolation methods can be used if a fast image reconstruction algorithm is required. See Appendix C for the details of the above interpolation methods. The performances of the methods are compared and tested in the next subsection.

As a summary, in this subsection an expansion/shrinkage motion artifact free image reconstruction algorithm is proposed. The rectangular samples over the k-domain of the proton density distribution are interpolated after the phase compensation of the acquired data. And then the inverse Fourier transform of the calculated data gives the artifact free image.

5.2.3 Simulations and Results

In this study, some simulations are carried out to see the properties of the proposed image reconstruction method. Firstly, a fictitious phantom is selected as a test object. This object is assumed to have a respiratory motion. The MR signal is simulated under these conditions. The reconstruction method is tested with this MR signal. The reconstructed image has almost no blurring or motion artifact. Different interpolation methods are used to recover the uniform samples from the non-uniform samples and their performances in terms of the image

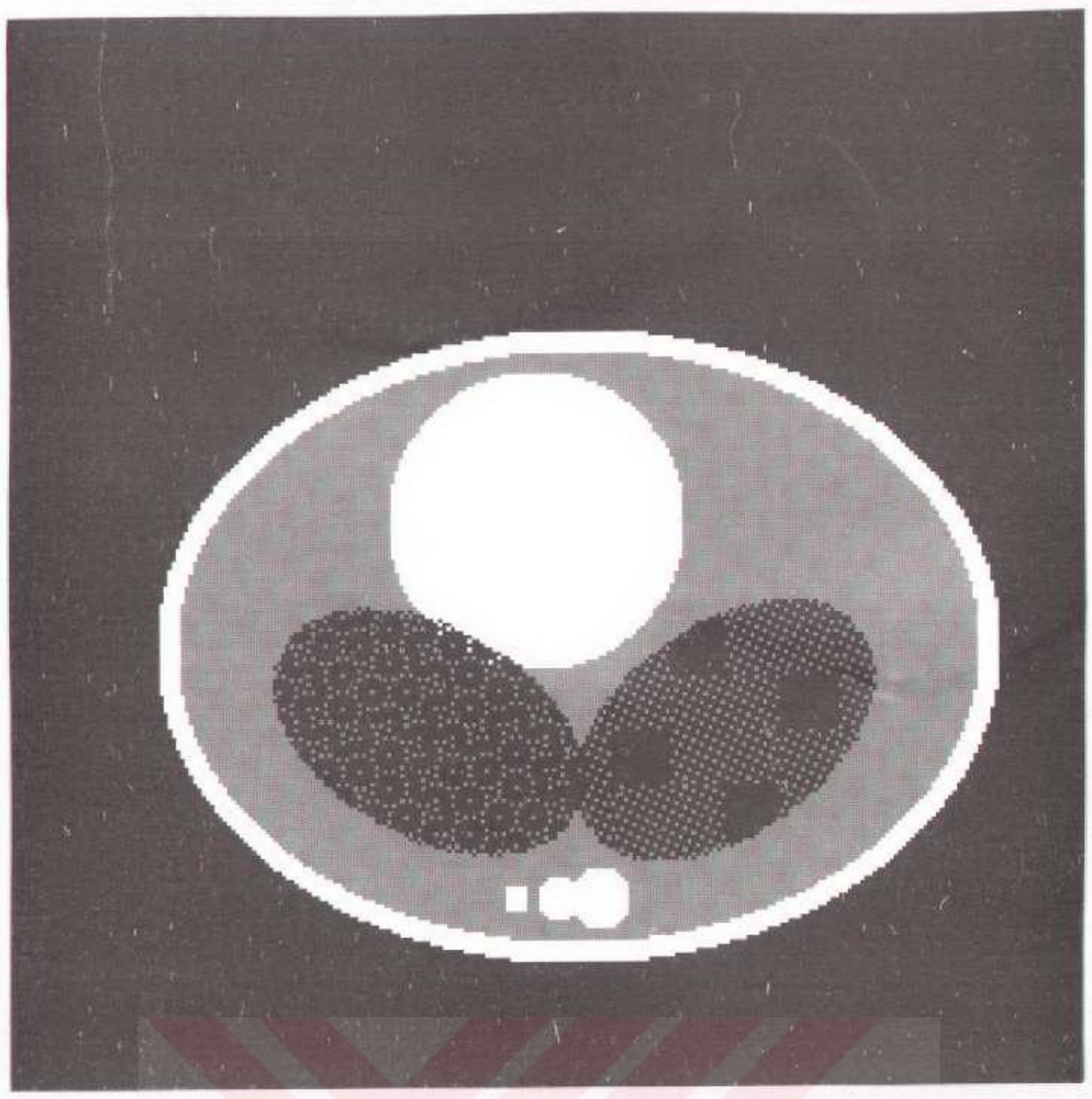

Figure 5.2: The 2-dimensional mathematical chest phantom. The white circular object represents the heart. The small circular objects stand for the backbone. The lungs are represented by two elliptic objects which have different internal structures. The thin layer covering the phantom stands for the fat around the body. The proton density is given in arbitrary units. The circular objects have 1 unit of proton density, whereas the lungs have 0.1 unit. The other parts of the phantom are assumed to be filled with 0.5 units of proton density. The field of view (f_x, f_y) is $(256mm, 256mm)$.

quality are observed. The new reconstruction method is tested with incorrect values of the model parameters. It is shown that if the errors in the model parameters are reasonable then a substantial amount of motion artifact reduction in the reconstructed image will be observed. In other words, the new method is robust with respect to to the model parameters.

Let the mathematical phantom object shown in Figure 5.2 be the test object. Assume that the object moves as defined in the expansion/shrinkage motion

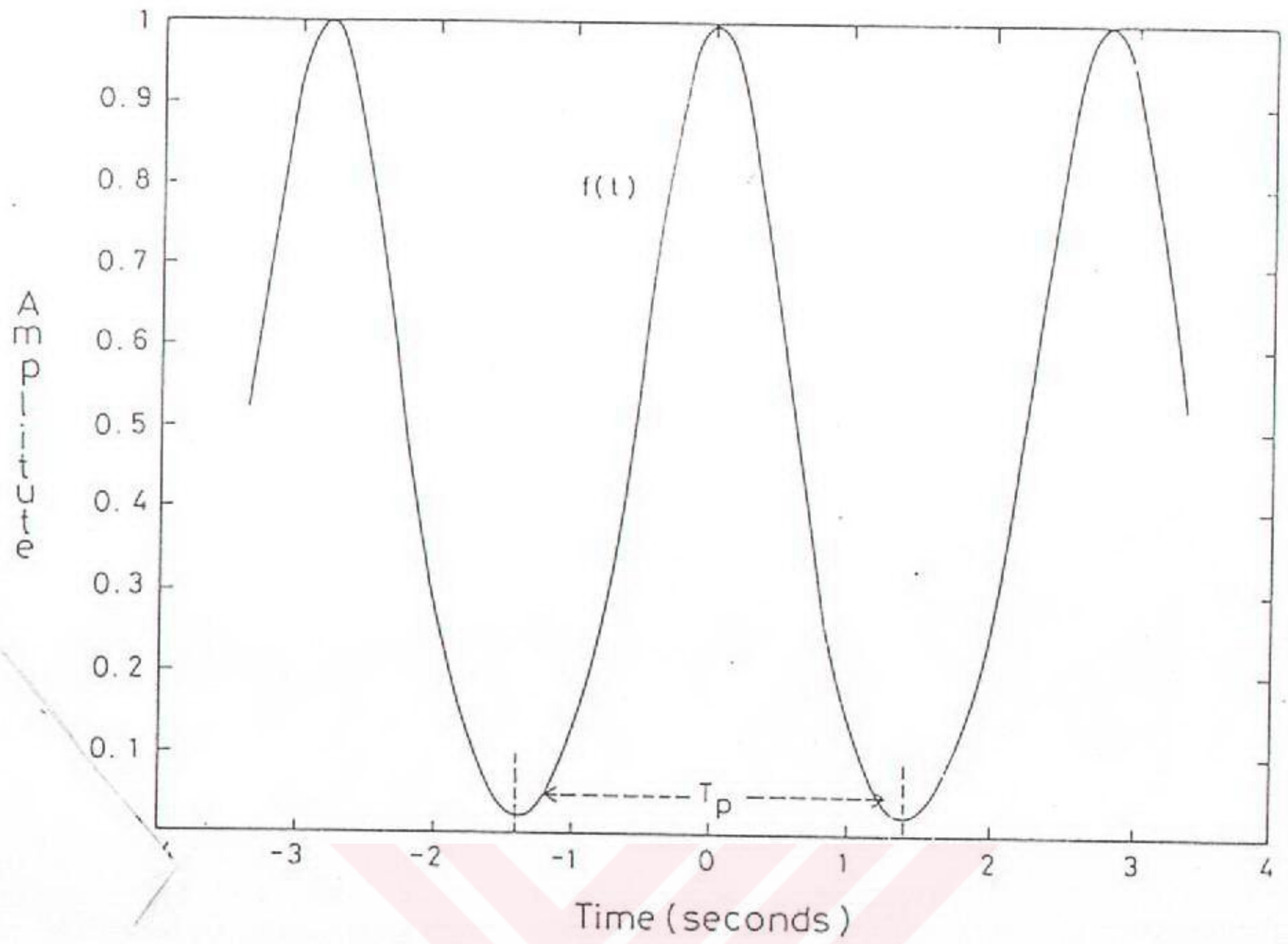

Figure 5.3: The respiratory fluctuation function which is used in the simulations. It is a periodic function with a period of $T_p = 2800msec.$ The function is equal to $\exp(-16t^2/T_p^2)$ for $-T_p/2 < t \leq T_p/2$.

model (see equation Eq. 4.74). Let the parameter $\boldsymbol{c}$ (the center of the expansion) be positioned near the backbone of the phantom. The diagonal percentage expansion matrix is assumed to be:

$$\mathcal{A}(t) = \begin{bmatrix} a_x f(t) & 0 \\ 0 & a_y f(t) \end{bmatrix} \tag{5.19}$$

Here, the fluctuation function $f(t)$ is periodic (see Figure 5.3):

$$f(t + nT_p) = \exp\left(-16\left(\frac{t}{T_p}\right)^2\right) \quad \text{for } -\frac{T_p}{2} \leq t < \frac{T_p}{2} \tag{5.20}$$

The amplitudes of the fluctuation function in x and y directions, a_x and a_y, are selected as 4% and 10% for the simulations, respectively. The motion period, T_p, is assumed to be $2800msec.$

During the study a simulated standard spin-warp imaging pulse sequence is applied to the test object (see Figure 2.20). In each simulation experiment a fixed repetition interval is used with $T_r = 1500msec$. Total of 256 repetition intervals are carried out. In each repetition interval, 256 samples are acquired with a $20\mu sec$ sampling period. Therefore the data acquisition period $t_y = 5.12msec$. The echo time, T_e, is $30msec$. The phase encoding (x) gradient application period, t_x, is $3msec$. The gradient pulse amplitudes are arranged so that a region which has a size of $256mm \times 256mm$ is viewed.

If the inverse Fourier transform were directly applied to the simulated MR signal which is taken from this moving object, then the image would have the respiratory motion artifact (see Figure 5.4). The same data is reconstructed using the proposed method (see Figure 5.5). The motion artifacts and blurring due to the motion are significantly suppressed.

The practical difficulty of the proposed image reconstruction method is the computation time. The most time consuming part of the method is the interpolation from non-rectangular samples to rectangular samples. As it was explained in the previous section, to find the rectangular samples from the non-rectangular samples it is required to calculate the pseudo inverses of (256×256) matrices using the singular value decomposition (SVD) method where 256 is the dimension of the image. The distribution of the non-uniform samples in each row is different. Therefore 256 different S matrices must be decomposed. On the other hand, the positions of the non-uniform samples in each column are the same. Therefore only one SVD is enough for the interpolation in the y direction. Total of 257 SVD are required. In SUN-3 160 system which has a floating point accelerator (fpa), each SVD takes approximately 13 CPU minutes. Therefore an image reconstruction time is approximately 56 hours.

Much quicker image reconstruction can be achieved by some other interpolation methods. The linear interpolation method requires much less computation time. Firstly, the non-uniform samples are sorted with respect to the sampling positions. And the rectangular samples are taken from an imaginary piecewise linear curve the corners of which are on the non-uniform samples. This method

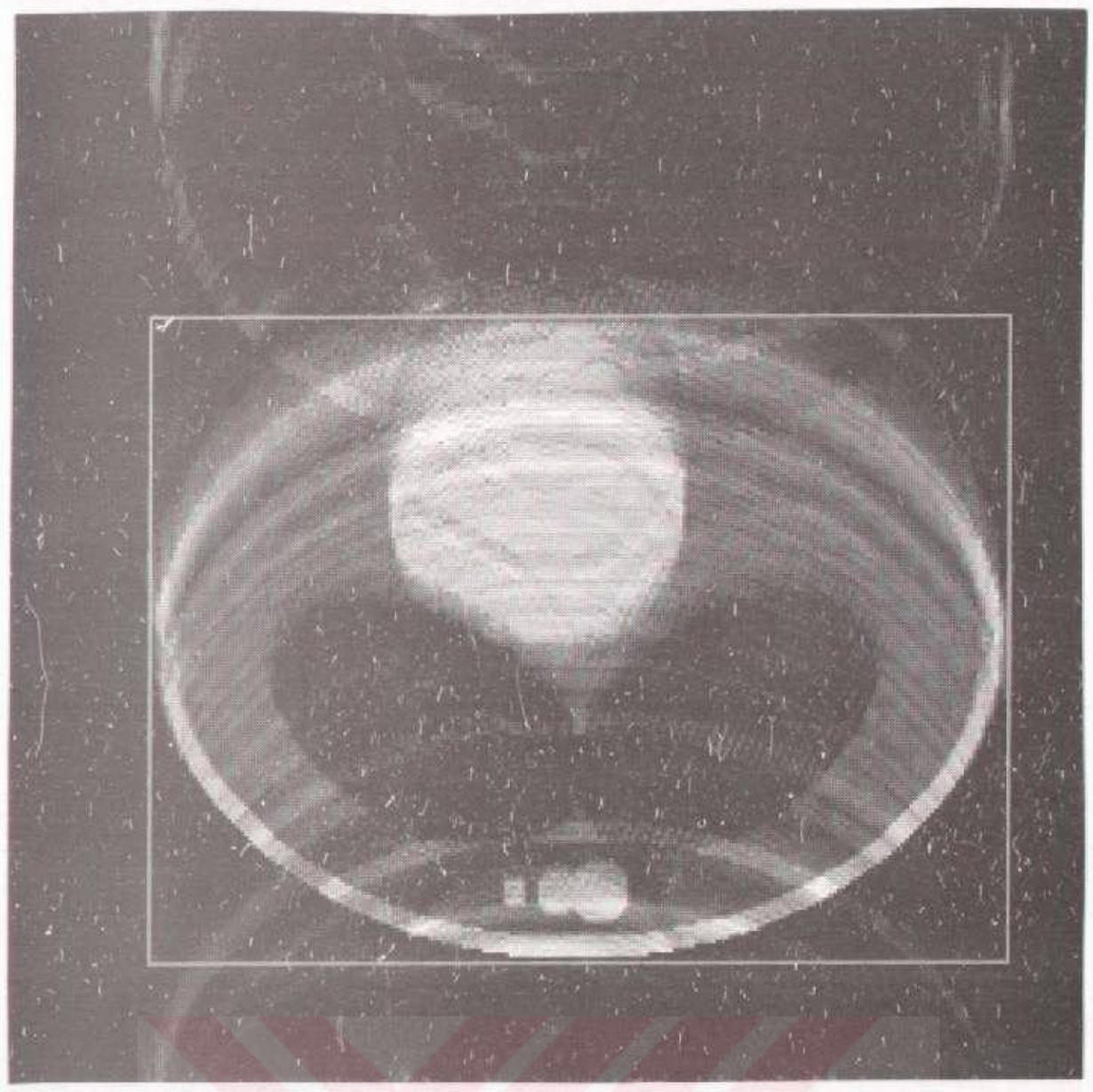

Figure 5.4: An image of the object with a simulated respiratory motion if the standard FT reconstruction method is used. The motion model parameters a_x, a_y, c_x, and c_y are 4%, 10%, $7mm$ and $98mm$, respectively. The respiratory motion artifact can be observed on the image. As a measure of the image quality, the average of the intensity levels at the outside of the region of interest, e, is evaluated as 0.121 units. The region of interest (ROI) is inside the rectangle shown in the figure.

adds a total of 10 seconds to the conventional reconstruction time. The image obtained by this method is also acceptable (see Figure 5.6). The linear interpolation is useful for the reconstruction of the images which do not have strong motion artifact.

The third order Lagrange and the cubic spline interpolation methods are also used. It is observed that these interpolation methods fail if there are very closely located samples. The noise on the neighbor samples may cause very high swings on the interpolated data. So the samples which are closer than a threshold are

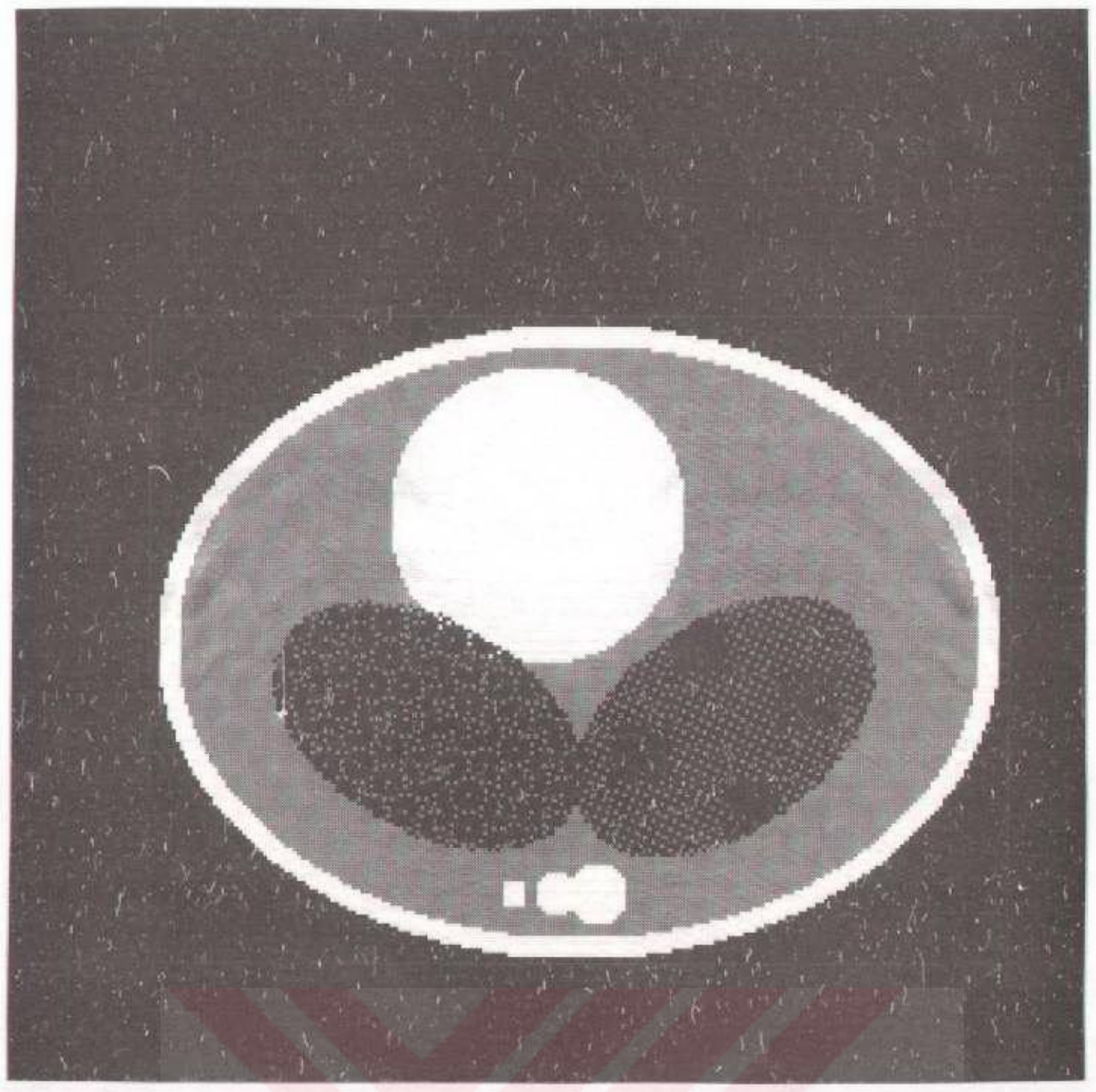

Figure 5.5: An image using the proposed reconstruction method. Almost all the motion artifact is suppressed. Exact motion model is assumed to be known. The rectangular samples are calculated using the pseudo inverses of 257 different matrices. The average of the intensity levels at the outside of the ROI, e, is 0.0217 units.

replaced with their averages. In a sense this corresponds to removing singularities in the $\mathcal{S}$ matrix. In this way, the interpolation method is stabilized.

The third order Lagrange interpolation is applied after sorting the samples and removing the singularities as explained in the previous paragraph (see Figure 5.7). The quality of the images which are obtained using the third order Lagrange interpolation is better compared to the images obtained using the linear interpolation. The Lagrange interpolation adds a total of 15 seconds to the conventional reconstruction time. The cubic spline interpolation method is the best among these quick interpolation methods (see Figure 5.8). The overhead of the cubic spline method is approximately the same as the Lagrange interpolation

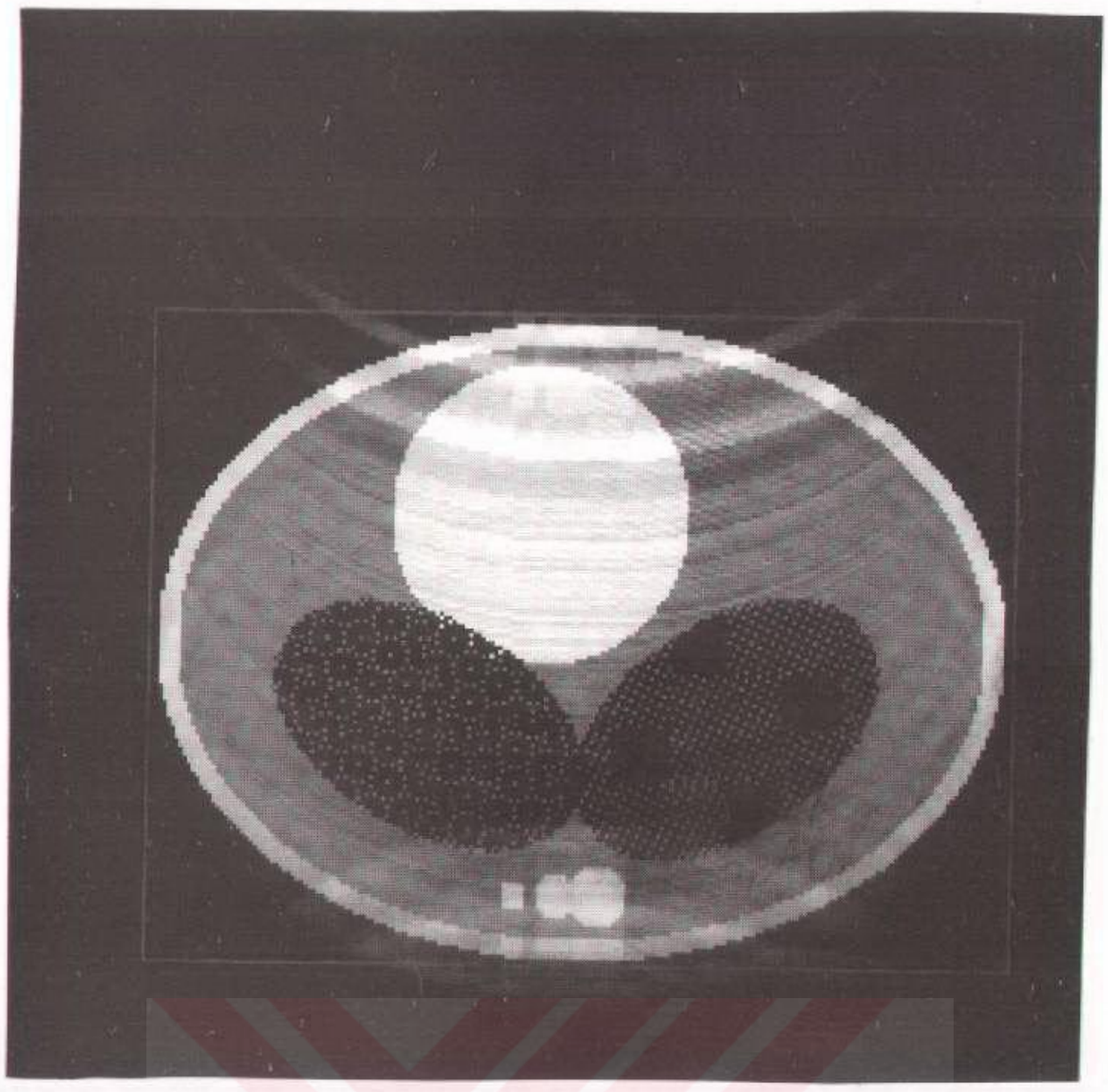

Figure 5.6: An image using the linear interpolation. The rectangular samples are calculated using the linear interpolation of the non-rectangular samples. The motion artifact is reduced. The remaining motion artifact is due to the errors in the interpolation method. The average of the intensity levels at the outside of the region of interest is 0.0548 units.

method (15 seconds).

As a fifth interpolation method, a composite interpolation method is used. The motion in the x direction is compensated using the cubic spline interpolation method and the motion in the y direction is compensated by the singular value decomposition. The result is almost as good as the image obtained by the motion artifact suppression using SVD in both directions (see Figure 5.9). But it is much quicker (approximately 15 minutes).

The selection of the interpolation method among these five methods depends on the quality of the image one wants to obtain and the amount of time that can be afforded for the reconstruction of the images.

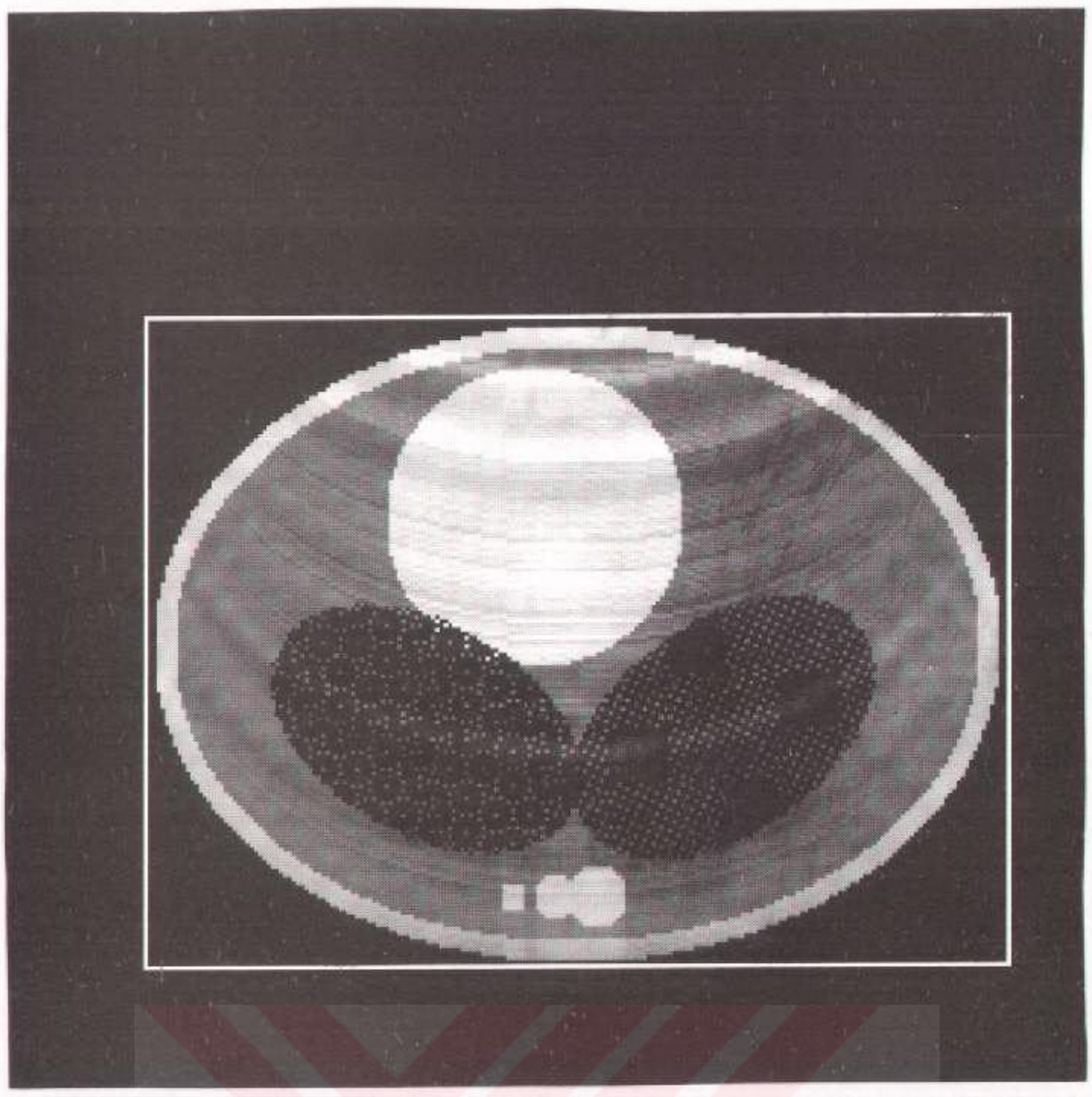

Figure 5.7: An image using the third order Lagrange interpolation. The rectangular samples are calculated using the third order Lagrange interpolation of the non-rectangular samples. Before the interpolation, 12×256 samples which are too closely located to some other samples are removed from the non-rectangular sample set. The average of the intensity levels at the outside of the region of interest is 0.0464 units.

In all the above image reconstruction methods the exact motion model is assumed to be known. If the exact motion model is not known, then the reconstructed image will still have some motion artifact. The important point is that even if an approximate expansion/shrinkage motion model is used the reconstructed image would still be better then the image which is reconstructed by the standard methods. To test this fact some simulations are conducted with incorrect a_x, a_y, c_x, c_y and $f(t)$ values to observe the sensitivity of the reconstruction technique to these parameters. The cubic spline method is used in all these simulations.

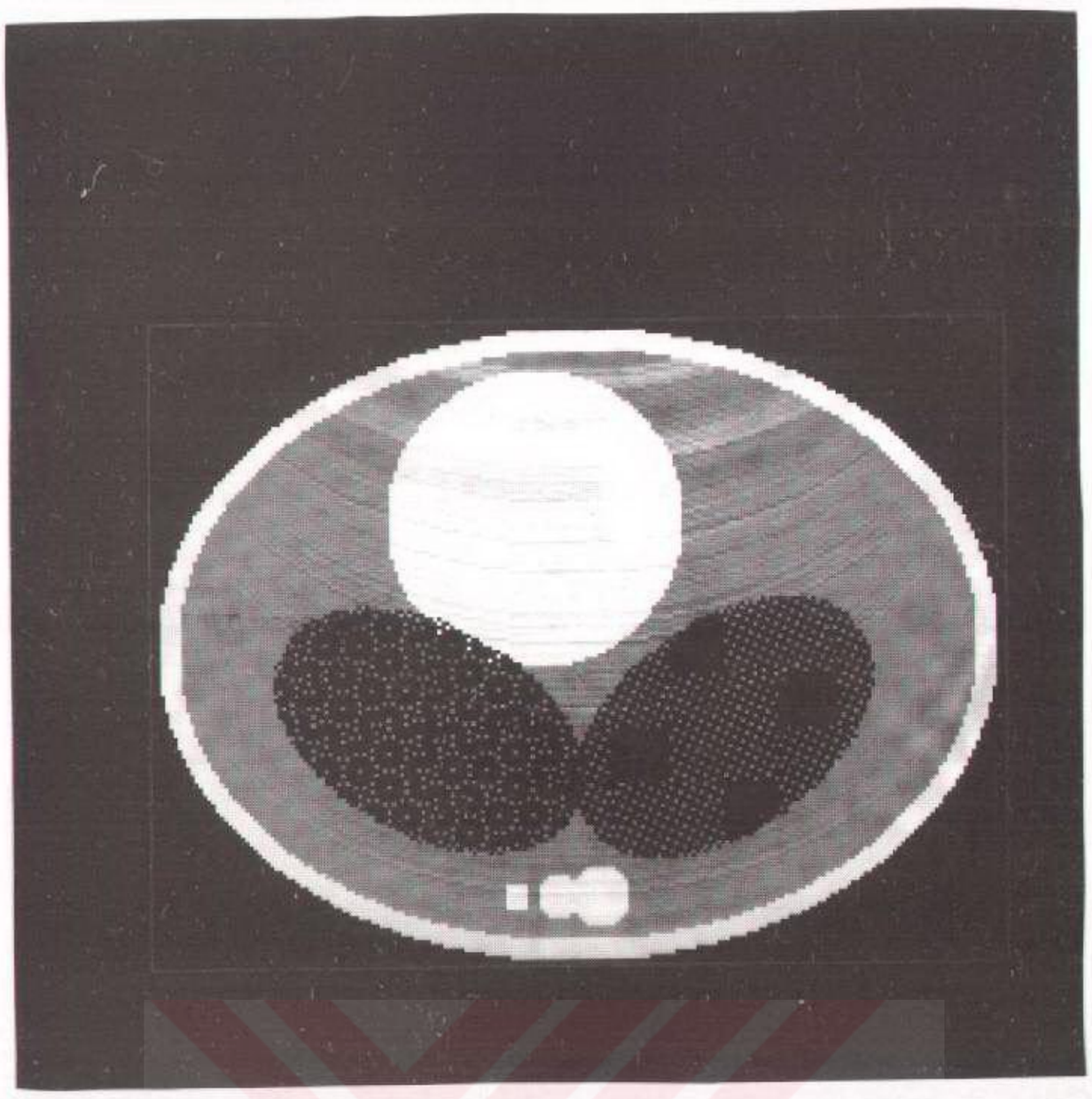

Figure 5.8: An image using the cubic spline interpolation. The rectangular samples are calculated using the cubic spline interpolation of the non-rectangular samples. Before the interpolation, 12×256 samples which are too closely located to some other samples are removed from the non-rectangular sample set. The average of the intensity levels at the outside of the region of interest is 0.0396 units.

5.2.3.i Sensitivity of the reconstruction method to the fluctuation function

In reality, it is not possible to measure or estimate the percentage expansion matrix, $\mathcal{A}(t)$, exactly. The image must be reconstructed using an approximate value for $\mathcal{A}(t)$. The proposed reconstruction method is not very sensitive to this parameter. If one reconstructs the image of a moving object using $\tilde{\mathcal{A}}(t)$ instead of $\mathcal{A}(t)$ then the reconstructed image will have a similar artifact of the image of the object under a respiratory motion with the parameter $\left(\mathcal{A}(t) - \tilde{\mathcal{A}}(t)\right)$. If the

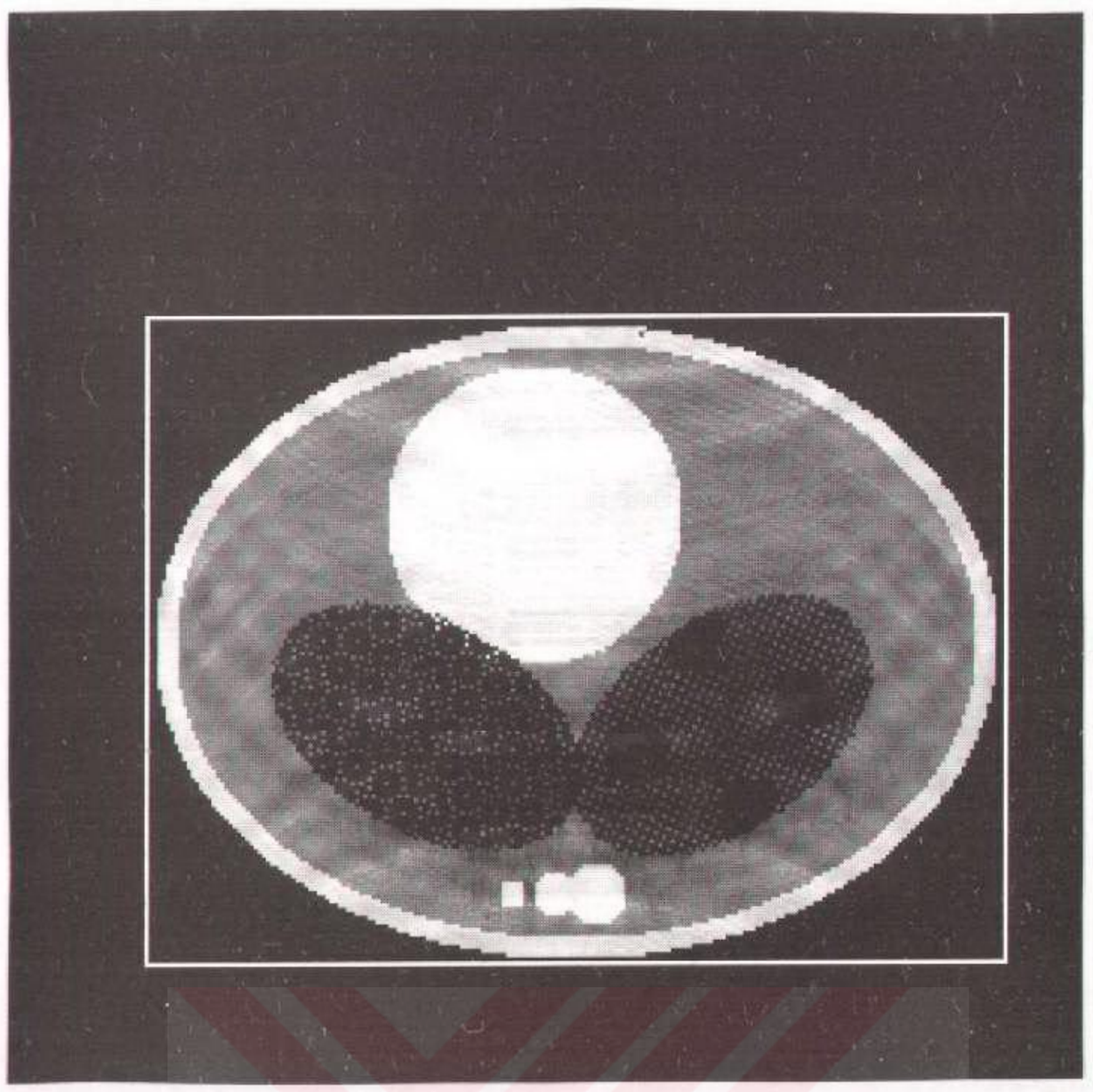

Figure 5.9: An image using the composite interpolation. The motion in the x direction is compensated using the cubic spline interpolation. In this direction there were no too closely located samples, so all the samples are used. In the y direction, the motion is compensated by the pseudo matrix inversion. To find the pseudo inverse, 24 eigen-values of the $\mathcal{S}$ matrix are set to 0. The average of the intensity levels at the outside of the region of interest is 0.0321 units.

measurement error, $\left(\mathcal{A}(t) - \tilde{\mathcal{A}}(t)\right)$, is reasonable then a substantial amount of image artifact reduction is expected. This fact is justified both experimentally and theoretically.

Three simulations are carried out to observe the effect of the measurement error. $\mathcal{A}(t)$ has three parameters: $f(t)$, a_x and, a_y. The measurement error on these parameters are analyzed separately. If the measurement error in the amplitude of the fluctuation function along the x direction is less than 100% (i.e. if $|a_x - \hat{a}_x| < |a_x|$) there will be artifact reduction. In the first simulation, a_x is assumed to be measured with 50% error ($\hat{a}_x = 0.5a_x$). And the image is

reconstructed with $\hat{a}_x$ instead of a_x (see Figure 5.10). The ghost artifact due to the motion in y direction is completely suppressed and the artifact due to the x motion is reduced. Secondly, a similar simulation is carried out for the fluctuation function amplitude in the y direction. The motion artifact suppression is observed on the image which is reconstructed with $\hat{a}_y = 8\%$ instead of its actual value 10% (see Figure 5.11). In general, if $|a_y - \hat{a}_y| < |a_y|$ then the proposed reconstruction method is helpful in the artifact reduction. In both experiments the fluctuation function $f(t)$ is assumed to be known. An additive white noise on the measured fluctuation function, $\hat{f}(t)$, is assumed. The signal to noise ratio (SNR) of $\hat{f}(t)$ is $20dB$. The image obtained by $\hat{f}(t)$ is shown in Figure 5.12. Since the error function $f(t) - \hat{f}(t)$ is not periodic then $d\tilde{\boldsymbol{k}} - \Delta\boldsymbol{k}$ is not periodic, either, so there is not ghost like image artifact but there is blurring on the image. As the SNR of the $\hat{f}(t)$ decreases, the contrast to noise ratio of the reconstructed image also decreases.

The theoretical analysis of the sensitivity of the reconstruction method to $\mathcal{A}(t)$ is also conducted. The acquired data was formulated as (see equation Eq. 4.78):

$$\tilde{P}[\boldsymbol{k}] = \exp(j\Delta\boldsymbol{k}^T\boldsymbol{\mathcal{V}}\boldsymbol{c})P_s(\boldsymbol{\mathcal{V}}(\boldsymbol{k} - \Delta\boldsymbol{k})) \tag{5.21}$$

The proposed reconstruction method is based on this equation. The rectangular samples of P_s are calculated using $s[k_x, k_y]$, before taking the inverse Fourier transform. The image reconstruction is possible if $\Delta\boldsymbol{k}$ and $\boldsymbol{c}$ are exactly known. In the reconstruction if one uses $\Delta\hat{\boldsymbol{k}}$ instead of $\Delta\boldsymbol{k}$ then the image $\hat{I}$ will be obtained instead of I. In this reconstruction the following equation will be the base of the method:

$$\tilde{P}[\boldsymbol{k}] = \exp(j\Delta\hat{\boldsymbol{k}}^T\boldsymbol{\mathcal{V}}\boldsymbol{c})\hat{P}_s\Big(\boldsymbol{\mathcal{V}}(\boldsymbol{k} - \Delta\hat{\boldsymbol{k}})\Big) \tag{5.22}$$

If the above equation is combined with Eq. 5.21 the following result will be obtained:

$$\hat{P}_s\Big(\boldsymbol{\mathcal{V}}(\boldsymbol{k} - \Delta\hat{\boldsymbol{k}})\Big) = \exp\Big(-j(\Delta\boldsymbol{k} - \Delta\hat{\boldsymbol{k}})^T\boldsymbol{\mathcal{V}}\boldsymbol{c}\Big)\, P_s(\boldsymbol{\mathcal{V}}(\boldsymbol{k} - \Delta\boldsymbol{k})) \tag{5.23}$$

Let $\hat{\boldsymbol{k}} \equiv \boldsymbol{k} - \Delta\hat{\boldsymbol{k}}$. One must be careful while changing the $\boldsymbol{k}$ vector by $\hat{\boldsymbol{k}} + \Delta\hat{\boldsymbol{k}}$, because $\Delta\boldsymbol{k}$ and $\Delta\hat{\boldsymbol{k}}$ are both functions of $\boldsymbol{k}$ (see equation Eq. 4.68). But if one

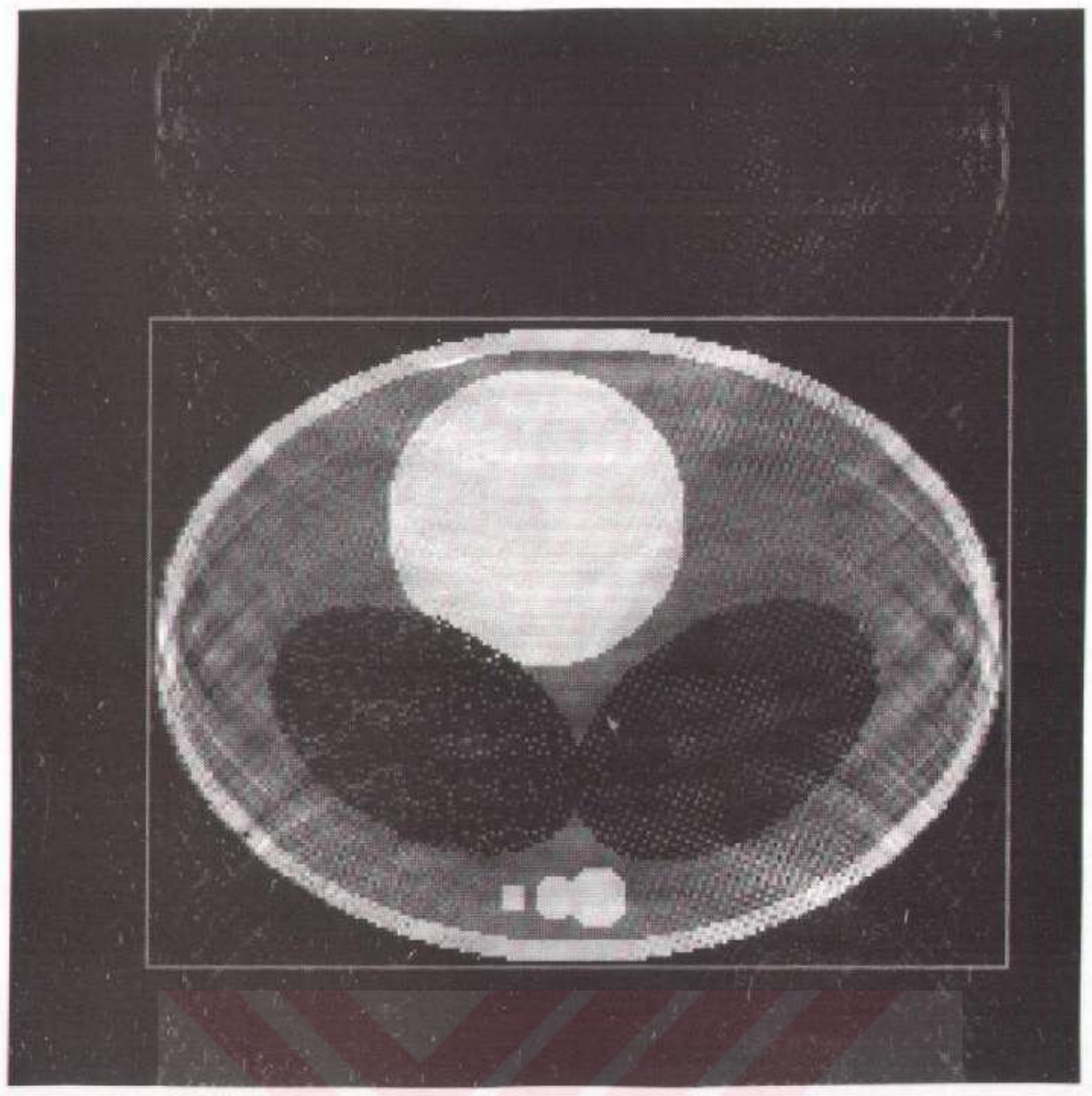

Figure 5.10: Demonstration of the sensitivity of the proposed method to the estimate of the motion function amplitude, a_x. The image is obtained by the proposed reconstruction method using $\hat{a}_x = 2\%$ instead of its exact value $a_x = 4\%$. The remaining motion parameters which are used in the reconstruction are the exact motion parameters. The composite interpolation method is used. To find the pseudo inverse, 33 eigen-values of the S matrix are set to 0. The average of the intensity levels at the outside of the region of interest is 0.0658 units.

assumes that

$$\Delta \boldsymbol{k}[\boldsymbol{k}] \approx \Delta \boldsymbol{k}[\hat{\boldsymbol{k}}] \tag{5.24}$$

the following approximate equation can be obtained:

$$\hat{P}[\hat{\boldsymbol{k}}] \approx \exp\left(-j(\Delta \boldsymbol{k} - \Delta \hat{\boldsymbol{k}})^T \boldsymbol{\mathcal{V}}^T \boldsymbol{c}\right) M\left(\boldsymbol{\mathcal{V}}(\hat{\boldsymbol{k}} - (\Delta \boldsymbol{k} - \Delta \hat{\boldsymbol{k}}))\right) \tag{5.25}$$

Since this approximate equation is similar to Eq. 5.21, the image artifact of the reconstructed image will be again a respiratory type of image artifact and the amount of this artifact will be small and proportional to the error in $\Delta \boldsymbol{k}$.

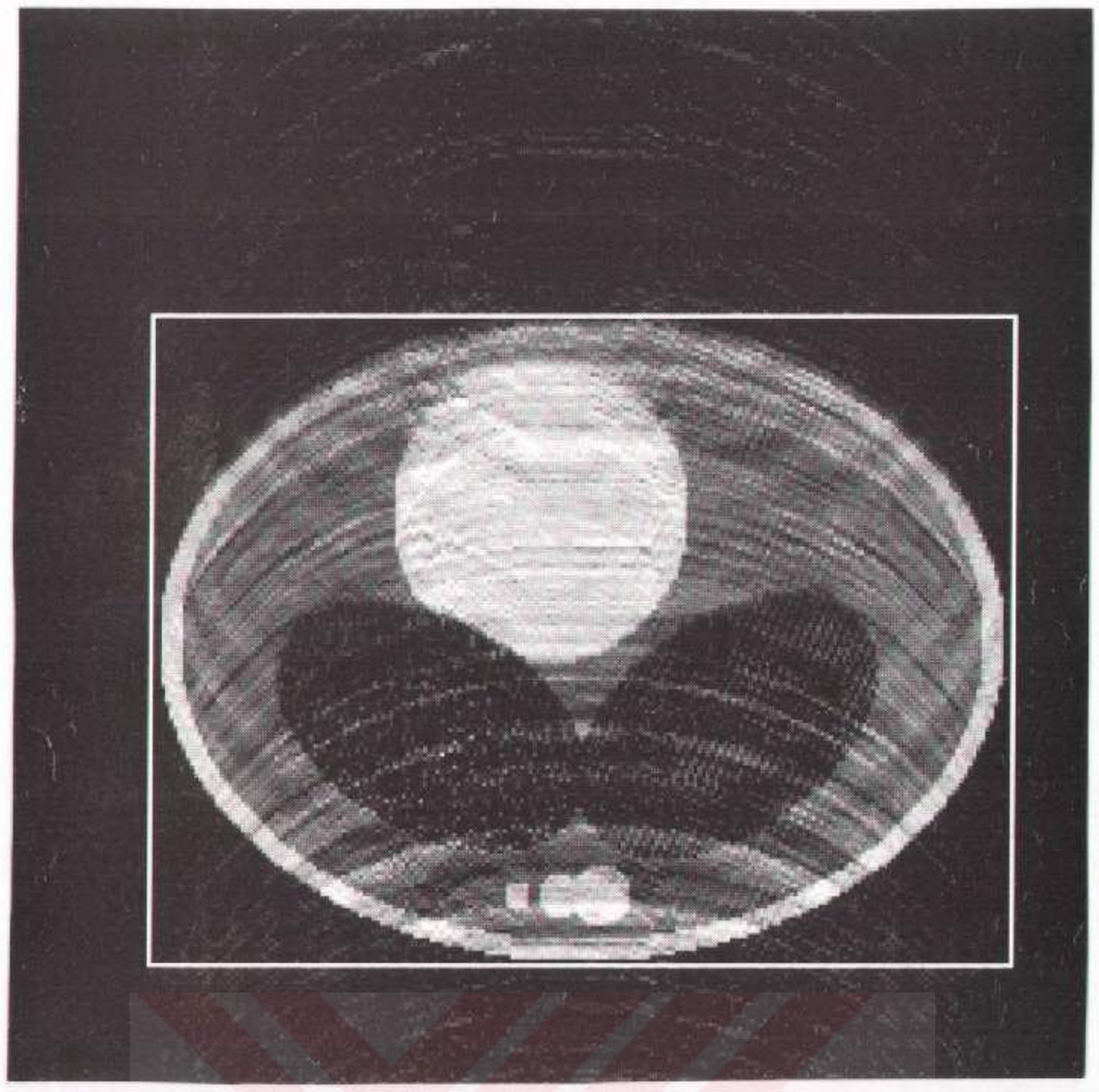

Figure 5.11: Demonstration of the sensitivity of the proposed method to the estimate of the motion function amplitude, a_y. The image is obtained by the proposed reconstruction method using $\hat{a}_y = 8\%$ instead of its exact value $a_y = 10\%$. The remaining motion parameters which are used in the reconstruction are the exact motion parameters. The composite interpolation method is used.To find the pseudo inverse, 33 eigen-values of the S matrix are set to 0. The average of the intensity levels at the outside of the region of interest is 0.0761 units.

There is a linear relation between $\Delta \boldsymbol{k}$ and $\boldsymbol{\mathcal{A}}(t)$:

$$\Delta \hat{\boldsymbol{k}} = \gamma \boldsymbol{\mathcal{V}}^{-1} \int_0^{k_x t_x/N+T_e} \boldsymbol{\mathcal{A}}([\tau', k_y]) \boldsymbol{g}_n([\tau', k_y]) \eta(k_x t_x/N + T_e, \tau') d\tau' \qquad (5.26)$$

Therefore, the error in $\boldsymbol{\mathcal{A}}(t)$ is proportional with the error in $\Delta \boldsymbol{k}$. As a result, if $\hat{\boldsymbol{\mathcal{A}}}(t)$ were used instead of $\boldsymbol{\mathcal{A}}(t)$ as the fluctuation function in the reconstruction algorithm then there would be artifacts on the reconstructed image as if there is a motion with the expansion matrix $\boldsymbol{\mathcal{A}}(t) - \hat{\boldsymbol{\mathcal{A}}}(t)$.

Reconstruction of an image with a reasonable estimate of the percentage

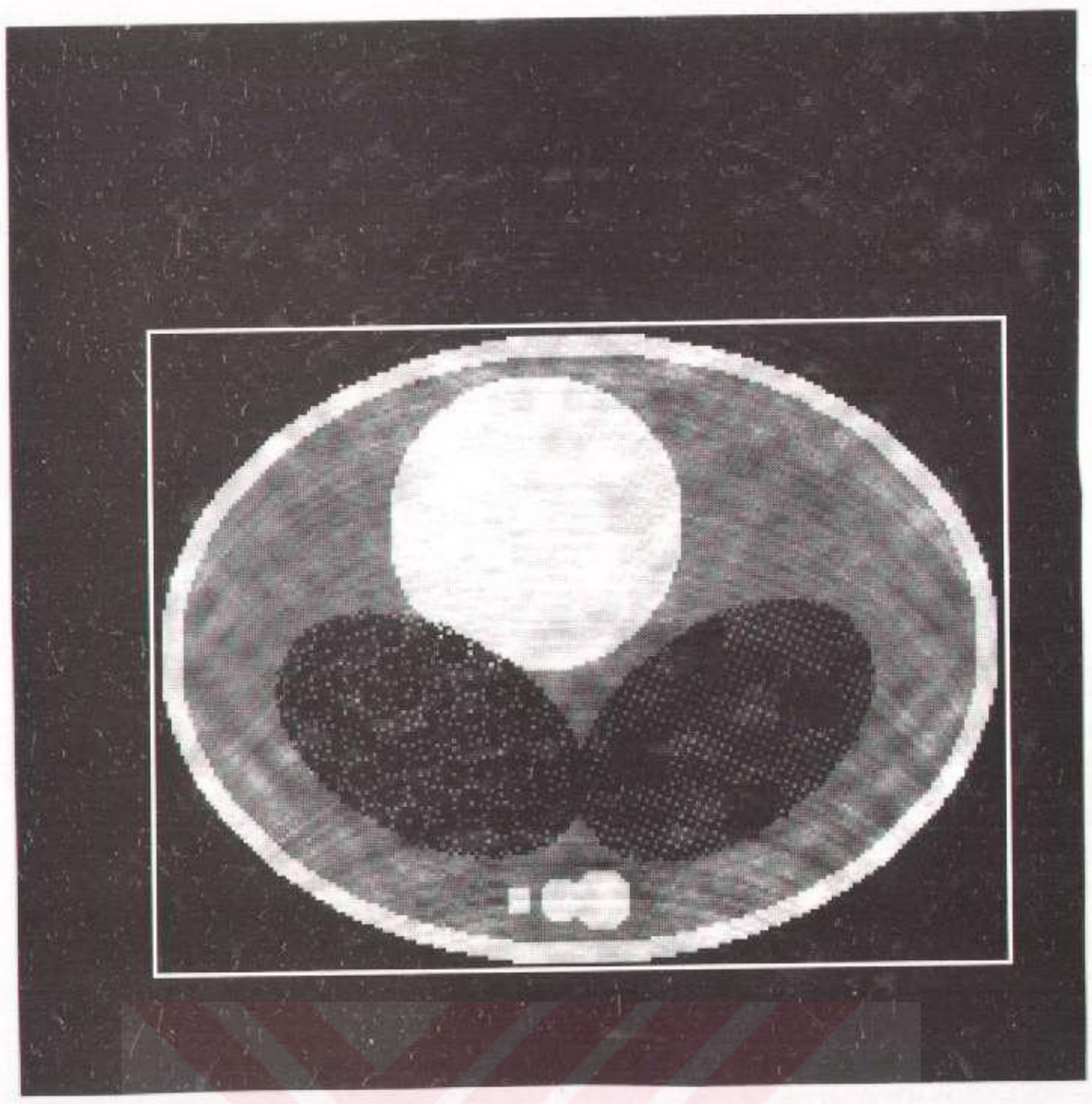

Figure 5.12: The image is reconstructed using the proposed method with a white noise error in the fluctuation function. The SNR of the fluctuation function is 20dB. The remaining motion parameters which are used in the reconstruction are the exact motion parameters. The composite interpolation method is used. To find the pseudo inverse, 39 eigen-values of the S matrix are set to 0. The average of the intensity levels at the outside of the region of interest is 0.1110 units.

expansion matrix $\mathcal{A}(t)$ considerably reduces the motion artifacts on the image.

5.2.3.ii Sensitivity of the reconstruction method to the center of expansion

Sensitivity discussion in this subsection is similar to the previous sections. If one reconstructs a moving object image with the motion parameter $\hat{c}$ instead of $\boldsymbol{c}$ then the reconstructed image will suffer from a motion artifact. This motion artifact will be similar to the artifact of the image of an object which has a block motion with $\mathcal{A}(\boldsymbol{c}-\hat{\boldsymbol{c}})$. A simulation result is given to confirm this argument. The

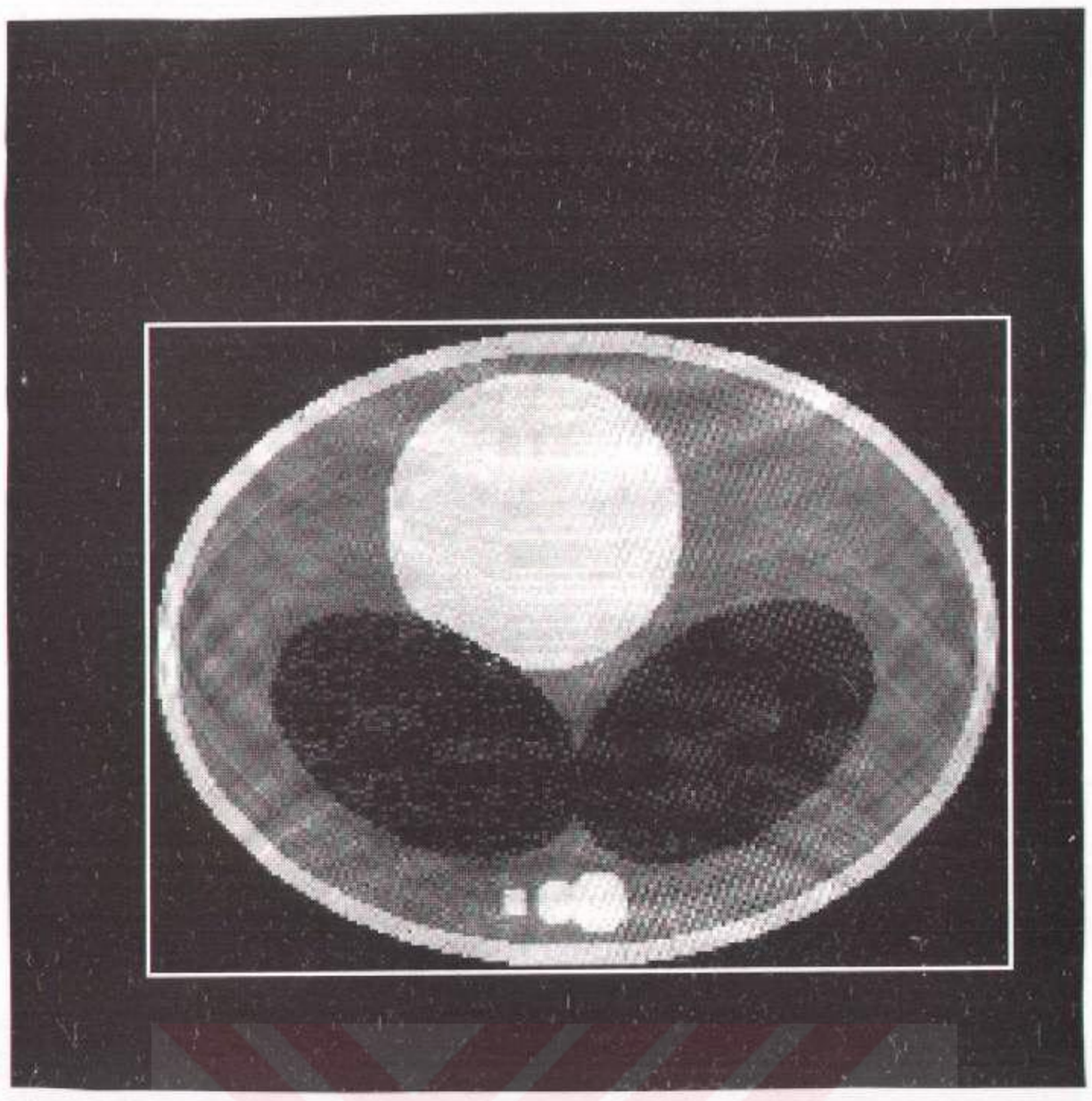

Figure 5.13: A simulation image to demonstrate the sensitivity of the proposed method to the motion model offset c_x. The MR image is reconstructed using the proposed method with incorrect value of the offset ($\hat{c}_x = -3mm$, $c_x = 7mm$). The artifact on the reconstructed image is a result of this $10mm$ error. For the image reconstruction the composite interpolation method is used. To find the pseudo inverse, 42 eigen-values of the S matrix are set to 0. The average of the intensity levels at the outside of the region of interest is 0.0629 units.

reconstruction is carried out using $\hat{c}_x$ instead of its real value c_x (see Figure 5.13). The motion artifact on this image is similar to the motion artifact of the image of the object which has a block motion in the x-direction. A similar simulation is carried out for the offset error in the y-direction (see Figure 5.14).

The sensitivity of the reconstruction method to the center of expansion is also theoretically analyzed. If the MR signal were taken from an object which has a expansion/shrinkage motion with parameter $\boldsymbol{c}$, then the acquired data would be as given in Eq. 5.21. Assume that the image is reconstructed using an erroneous

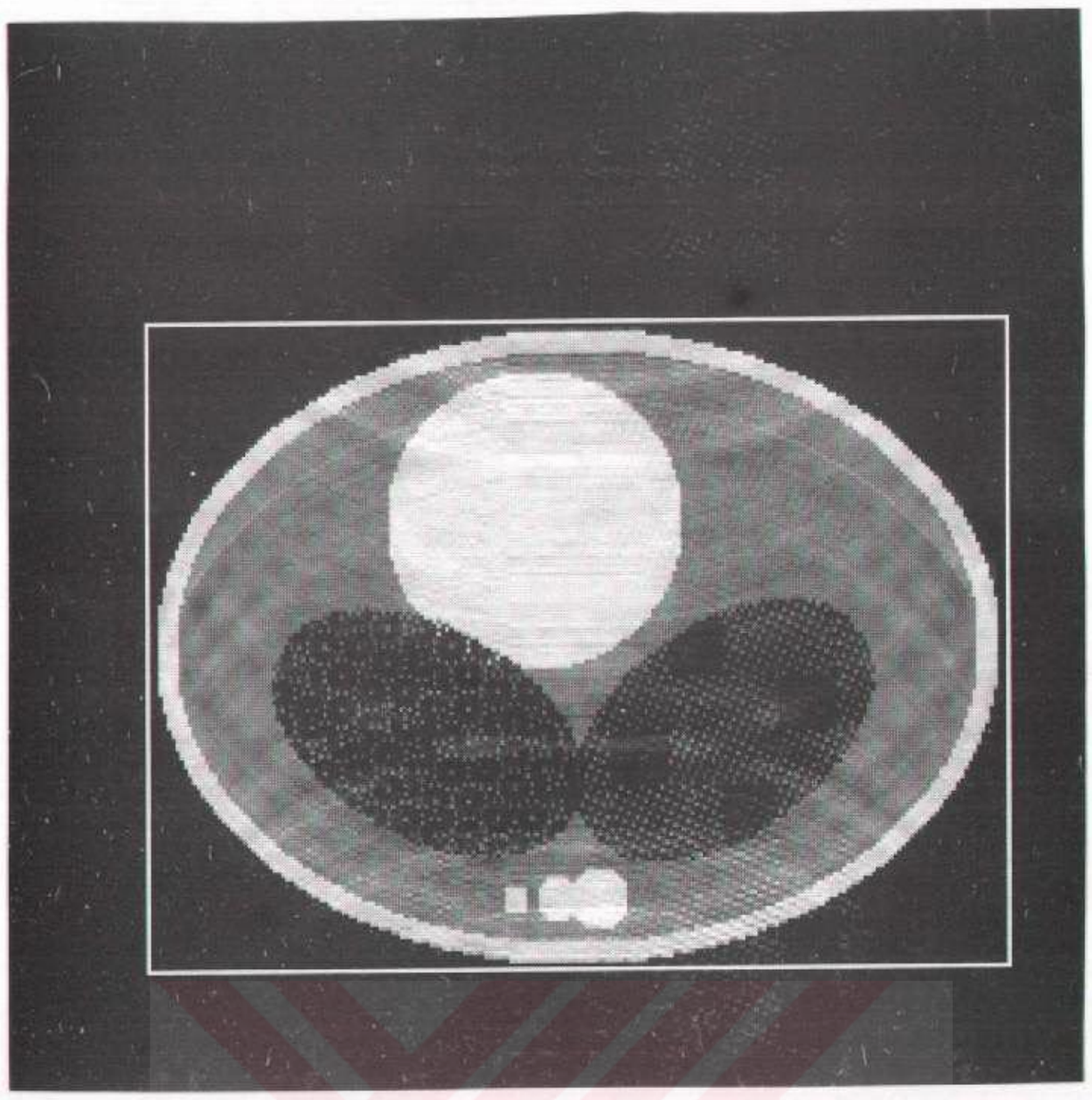

Figure 5.14: A simulation image to demonstrate the sensitivity of the proposed method to the motion model offset c_y. The MR image is reconstructed using the proposed method with incorrect value of the offset ($\hat{c}_y = -93mm$, $c_y = -98mm$). The artifact on the reconstructed image is a result of this $5mm$ error. For the image reconstruction the composite interpolation method is used. To find the pseudo inverse, 42 eigen-values of the S matrix are set to 0. The average of the intensity levels at the outside of the region of interest is 0.0715 units.

value of the center of expansion ($\hat{\boldsymbol{c}}$). The relation between the Fourier domain samples of the reconstructed image and the acquired data is:

$$\tilde{P}[\boldsymbol{k}] = \exp(-j\Delta\boldsymbol{k}^T\boldsymbol{\mathcal{V}}^T\hat{\boldsymbol{c}})\hat{P}\left(\boldsymbol{\mathcal{V}}(\boldsymbol{k}-\Delta\boldsymbol{k})\right) \tag{5.27}$$

If the above equation is combined with Eq. 5.21 the following result will be obtained:

$$\hat{P}_s\left(\boldsymbol{\mathcal{V}}(\boldsymbol{k}-\Delta\boldsymbol{k})\right) = \exp\left(-j\Delta\boldsymbol{k}^T\boldsymbol{\mathcal{V}}^T(\boldsymbol{c}-\hat{\boldsymbol{c}})\right) P\left(\boldsymbol{\mathcal{V}}(\boldsymbol{k}-\Delta\boldsymbol{k})\right) \tag{5.28}$$

Because of similar reasons as in Section 5.2.3.i, the vector $\boldsymbol{k}$ cannot be replaced by $\hat{\boldsymbol{k}} + \Delta\boldsymbol{k}$, unless we assume that

$$\Delta\boldsymbol{k}[\boldsymbol{k}] \approx \Delta\boldsymbol{k}[\hat{\boldsymbol{k}}] \tag{5.29}$$

then the following approximation will be obtained:

$$\hat{P}[\hat{\boldsymbol{k}}] \approx \exp\left(-j\Delta\boldsymbol{k}^T\boldsymbol{\mathcal{V}}^T(\hat{\boldsymbol{c}} - \boldsymbol{c})\right) P_s\left(\boldsymbol{\mathcal{V}}(\hat{\boldsymbol{k}})\right) \tag{5.30}$$

This equation is in the same form as Eq. 4.73. Therefore, the reconstructed image will suffer from the block motion if it is constructed with an approximate $\boldsymbol{c}$. But the amplitude of this block motion will be small and it is proportional to the error in the expansion center provided that the error in the center is much smaller than the size of the object.

5.2.3.iii Sensitivity of the reconstruction method to the higher order terms of the displacement function

It is known that the actual respiratory motion is not linear in space. For example, while the motion of the heart (for a phase of cardiac cycle) fits the block motion model, there is no motion within the spinal cord. If a linear respiratory motion is used as a model of the chest motion then the heart and the spinal cord are also assumed to obey the model. Obviously, this is not true. Therefore the question is "what will be the artifact if a linear motion model is used for reconstructing an image of an object which has a non-linear motion?".

To begin the analysis, let us rewrite the Taylor expansion formula (Eq. 4.59) for the displacement function:

$$\boldsymbol{d}(t;\boldsymbol{x}) = \boldsymbol{d}(t;0) + \boldsymbol{\mathcal{J}}(t)\boldsymbol{x} + \boldsymbol{d}_{ho}(t;\boldsymbol{x}) \tag{5.31}$$

For the non-zero $\boldsymbol{d}_{ho}$ case, the relation between the acquired MR signal and the proton density distribution will be as:

$$\tilde{P}[\boldsymbol{k}] = \zeta[\boldsymbol{k}] \int\int \rho_s(\boldsymbol{x}) \exp\left(j(\boldsymbol{k} - \Delta\boldsymbol{k})^T\boldsymbol{\mathcal{V}}\boldsymbol{x}\right) \lambda_{ho}(\boldsymbol{k};\boldsymbol{x}) dxdy \tag{5.32}$$

where

$$\lambda_{ho}(t;\boldsymbol{x}) = \frac{1}{D}\int_{-D/2}^{D/2}\exp\left(j\gamma\int_0^{\tau}\boldsymbol{g}^T([\tau',n])\boldsymbol{d}([\tau',n];\boldsymbol{x})\eta(\tau,\tau')d\tau'\right)dz$$

$$\lambda_{ho}(\boldsymbol{k};\boldsymbol{x}) = \lambda_{ho}([k_x t_x/N + T_e, k_y];\boldsymbol{x})$$

Although the motion model does not fit the linear respiratory motion model, if that model is chosen for the reconstruction, then the following equation will be the relation between the acquired data and the Fourier transform of the reconstructed image.

$$\tilde{P}[\boldsymbol{k}] = \exp(-j\Delta\boldsymbol{k}^T\boldsymbol{\mathcal{V}}^T\boldsymbol{c})\hat{P}_s\left(\boldsymbol{\mathcal{V}}(\boldsymbol{k}-\Delta\boldsymbol{k})\right) \tag{5.33}$$

Combining above equation and Eq. 5.32, and assuming

$$\Delta\boldsymbol{k}[\boldsymbol{k}] \approx \Delta\boldsymbol{k}[\hat{\boldsymbol{k}}] \tag{5.34}$$

$$\lambda(\boldsymbol{k},\boldsymbol{x}) \approx \lambda(\hat{\boldsymbol{k}},\boldsymbol{x}) \tag{5.35}$$

the following result is obtained:

$$\hat{P}[\boldsymbol{k}] \approx WD\iint\rho_s(\boldsymbol{x})\exp\left(-j\boldsymbol{k}^T\boldsymbol{\mathcal{V}}^T\boldsymbol{x}\right)\lambda_{ho}(\boldsymbol{k};\boldsymbol{x})dxdy \tag{5.36}$$

As a conclusion, the proposed reconstruction method cancels the linear and constant terms of the undesired phase of the acquired MRI signal. If the main components of a motion is the linear expansion and/or block motion then a substantial amount of motion artifact suppression will be obtained.

To observe this effect by simulation, an object which has a non-linear respiratory motion is selected. The heart of the phantom (the white circular block of the phantom) is assumed to be moving as a block while the other parts of the phantom has a linear respiratory motion. To obtain the MRI signal of this phantom two simulations are carried out. The heart of the phantom is removed and two independent objects are obtained. The block motion model is used in obtaining the MRI signal of heart. Another MRI signal is obtained by assuming a linear respiratory motion for the rest of the phantom. The MRI signal of the phantom which has a non-linear motion is acquired by adding the MRI signals of these two simulations.

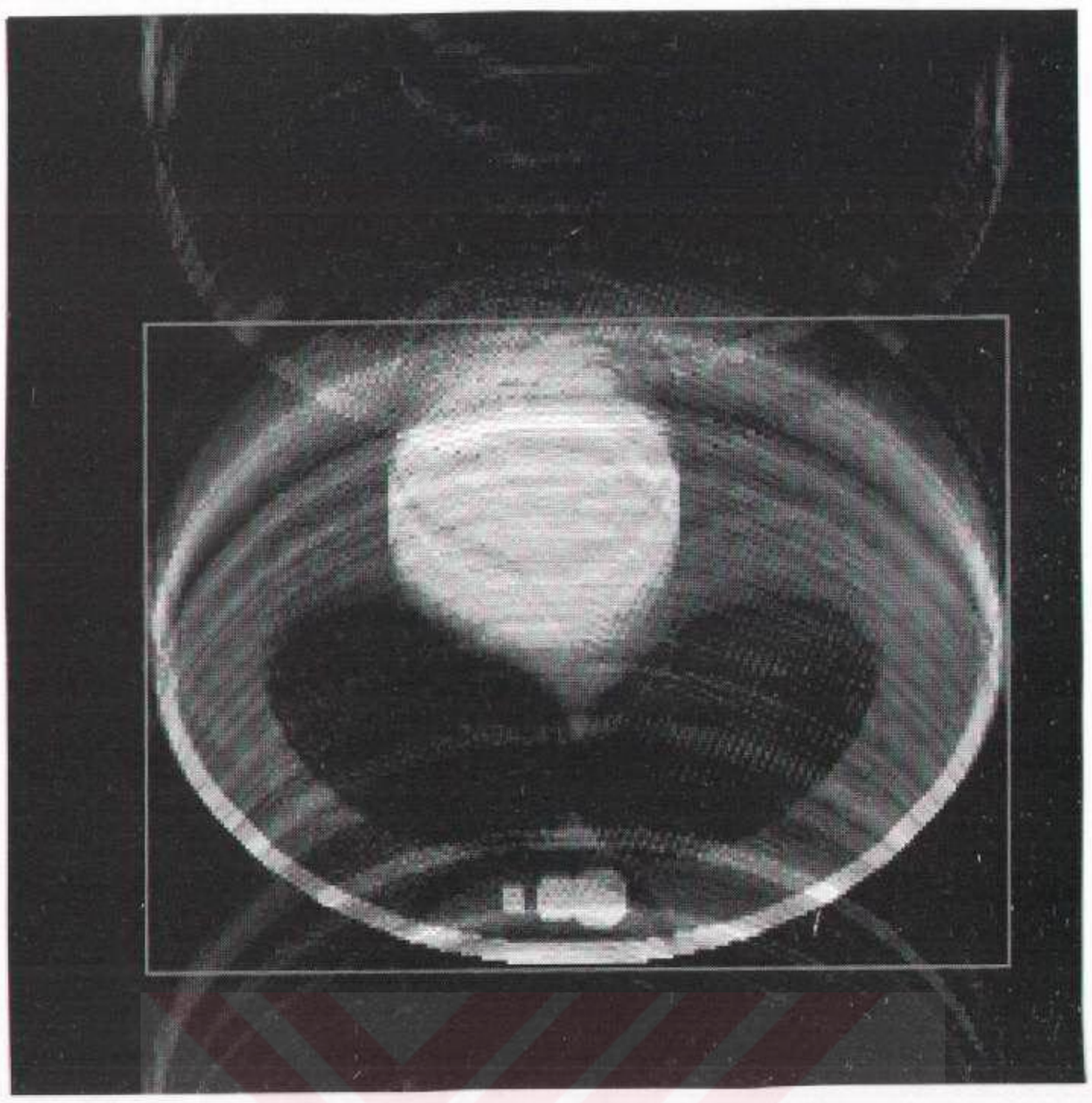

Figure 5.15: Non-linear motion during data acquisition causes non-linear motion artifact. The MRI signal is obtained by assuming the heart of the phantom has a block motion as explained in the text while the rest of the phantom has a linear respiratory motion. The image is reconstructed by the conventional image reconstruction method. The average of the intensity levels at the outside of the region of interest is 0.138 units.

The image shown in Figure 5.15 is reconstructed directly by taking the inverse Fourier transform of the MR signal. On the other hand, the image shown in Figure 5.16 is reconstructed by the proposed method. There is a considerable improvement in the image quality. The resultant image has some motion artifact due to the higher order undesired phase terms.

As a result, the non-linearity of the respiratory motion affects the reconstructed image quality. But it is demonstrated that, using the proposed image reconstruction algorithm the effects of the constant and linear terms of the respiratory motion are compensated and a significant reduction in the motion

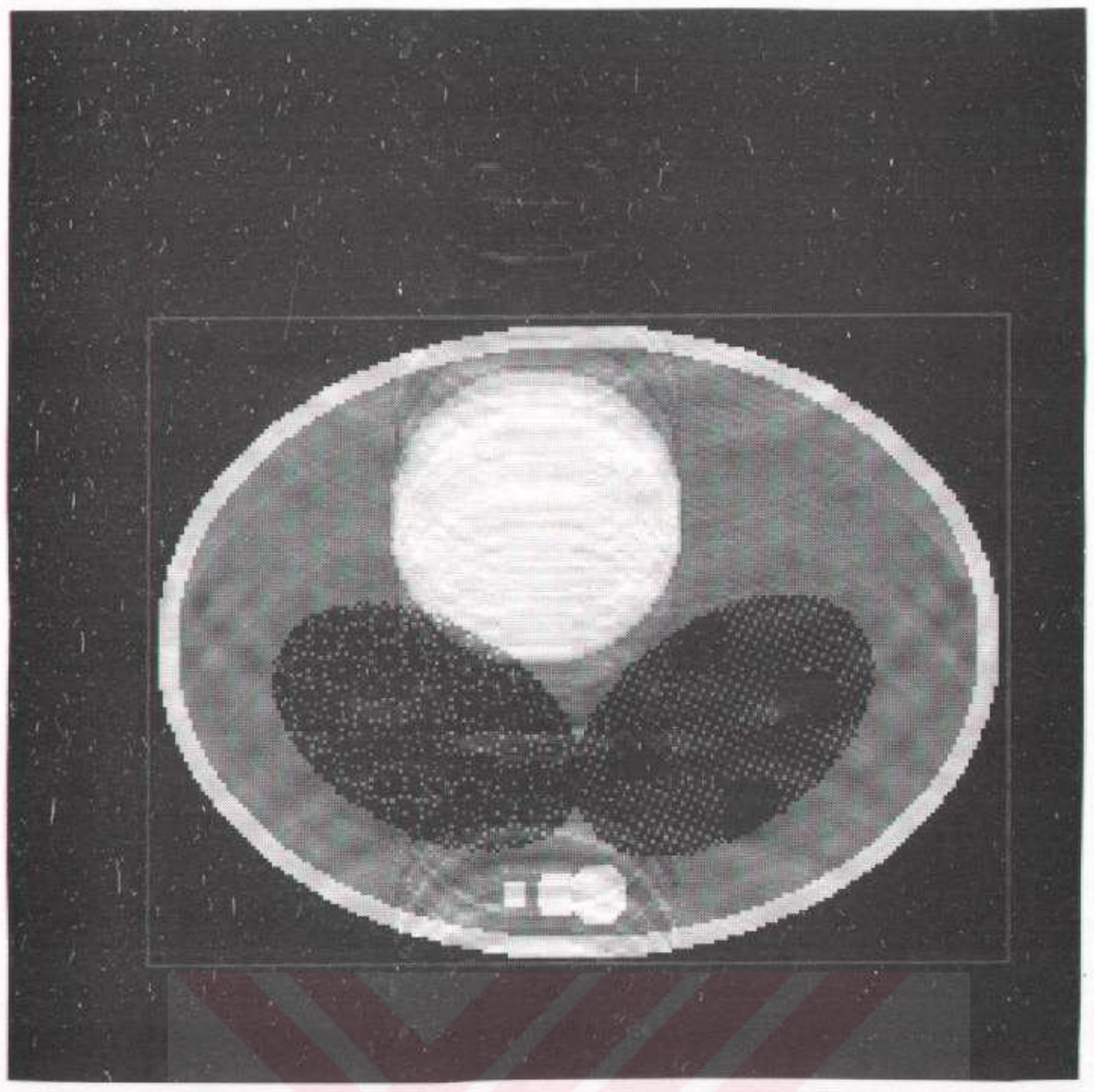

Figure 5.16: Reconstructed image of the non-linear motion using the proposed image reconstruction method. There is a motion artifact on the image due to the non-linear motion of the phantom. For the image reconstruction the composite interpolation method is used. To find the pseudo inverse, 47 eigen-values of the S matrix are set to 0. The average of the intensity levels at the outside of the region of interest is 0.0835 units.

artifact is obtained.

5.2.4 Estimation of the Motion Model Parameters

In the proposed image reconstruction method, the motion parameters, a_x, a_y, c_x, c_y and $f(t)$ are assumed to be known. However, the estimation of these parameters is one of the basic steps of the image reconstruction method.

The simplest way is to measure these expansion/shrinkage motion parameters using the displacement transducers [46]. In this method, at least two displacement transducers are required. Using these transducers, it is possible to measure the

amount of displacement at the positions where these transducers are placed. The position of the transducer and the center of the expansion may be marked by an operator on the image which has the ghost artifact. Using this information all the motion parameters can be easily calculated. Only drawback of this method is the requirement of a special (but simple) hardware and operator interaction.

In this dissertation, two motion parameter estimation methods are proposed although the direct measurement is feasible. In this way, full automation of the image reconstruction method is achieved. The first method that is explained in the following subsection is an iterative method to find these parameters. This method assumes that the fluctuation function, $f(t)$, is already known. The second subsection is devoted to a method which utilizes the navigator echoes [47] to obtain the motion model parameters.

5.2.4.i An iterative method for the estimation of the motion model parameters

As it is stated previously, in the estimation of the motion model parameters two displacement transducers are required and the positions of these transducers must be known. However, most of the commercial magnetic resonance imaging instruments support only one displacement transducer. Using this transducer only $f(t)$ can be measured. Since, there is no setup to find the position of the displacement in these instruments, another way to estimate the other motion model parameters (a_x, a_y, c_x, and c_y) must be investigated. In this subsection, first, a new method for the estimation of the center of expansion (c_x and c_y) is explained. Later an iterative method for the estimation of the amplitudes of the fluctuation functions (a_x and a_x) is proposed.

Finding the position of the center of expansion can be automated by the aid of a simple algorithm. The position of the center of expansion, (c_x, c_y), must be at the bottom center of the image. The location can be found from the original image which has the ghost artifact. For this purpose, the image projections, $p_x(x)$ and $p_y(y)$, onto x and y axes are obtained (see Figure 5.17). And then the estimated center of expansion is calculated. $\hat{c}_x$ is the mean value of x which

satisfies $p_x(x) > T$, and c_y is the minimum y which satisfies $p_y(y) > T$. Here T is an experimental threshold constant. By this algorithm, the center of expansion is estimated with no detectable error for the phantom we used. In real applications, there can be higher estimation errors, but it is already shown that the proposed algorithm is not very sensitive to errors in the estimates of $\boldsymbol{c}$.

The amplitudes of the fluctuation function along the x and y directions can be found using an iterative method which is developed in this dissertation [48]. In this method the center of expansion (c_x and c_y) and the fluctuation function, $f(t)$, are assumed to be known. For this case, the image can be reconstructed using initial estimates of the amplitudes of the fluctuation function along the x and y directions ($\hat{a}_x$ and $\hat{a}_y$). Because of the error in the initial estimates, the image will suffer from the motion artifact. The amount of the artifact on the image, e, is quantified as the average of the intensity levels where there is no object (background). It is a function of the estimates of the amplitudes of the fluctuation function.

$$e = e(\hat{a}_x, \hat{a}_y) \tag{5.37}$$

If the estimated and the real motion model parameters exactly match, (i.e. $\hat{a}_x = a_x$ and $\hat{a}_y = a_y$) there will be almost no motion artifact on the reconstructed image and e will be very close to zero. Therefore e will have a global minimum at this point. No local minimum is expected because as the error in the estimation increases the amount of motion artifact also increases (See Section 5.2.3.i).As an example, a 3-dimensional plot of the error function is given (see Figure 5.18). A global minimum at the expected point can be seen and there are no local minima.

Therefore, the parameter estimation problem can be converted to a multivariate minimization problem. The parameters which minimize the function e are the correct motion model parameters. There are many known multivariate minimization algorithms in the literature [49]. The polytope, Powell and quasi Newton minimization algorithms are used to find the global minimum. The polytope algorithm solved the sample problem in the previous section in 160 iterations with 0.01 % error. On the other hand the Powell minimization

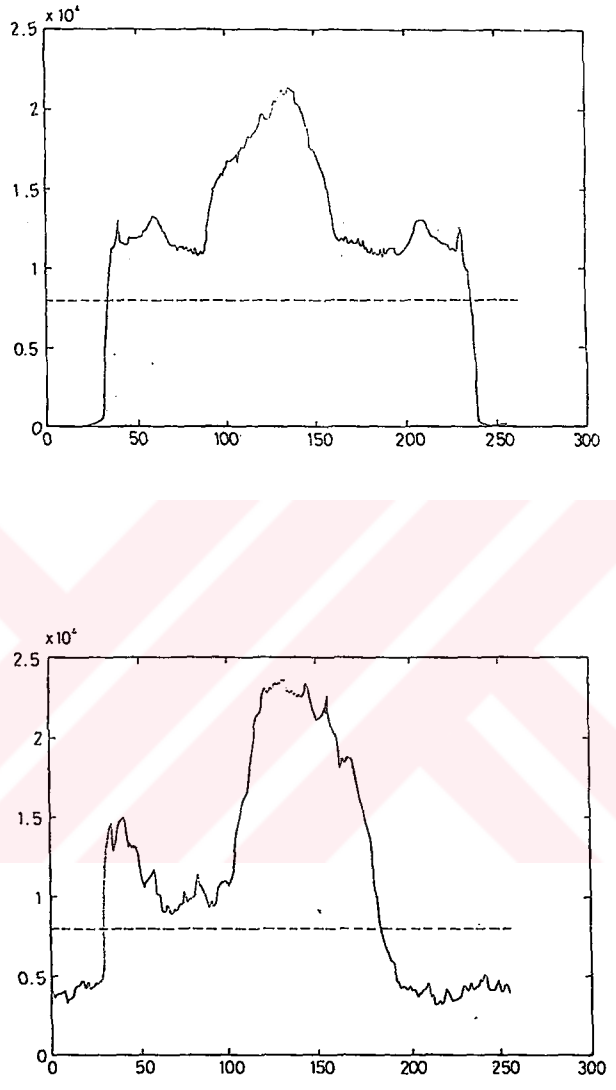

Figure 5.17: The projections of the image shown in Figure 5.4. (a) The projection onto x-axis, $p_x(x)$, (b) the projection onto y axis, $p_y(y)$. The image shown in Figure 5.4 is obtained by the conventional reconstruction method. $p_x(x)$ is obtained by summing the intensities of the pixels over the vertical lines. Similarly, $p_y(y)$ is obtained as the sum of the intensities of the pixels over the horizontal lines. The dashed line shown in both graphics represents the threshold level, T.

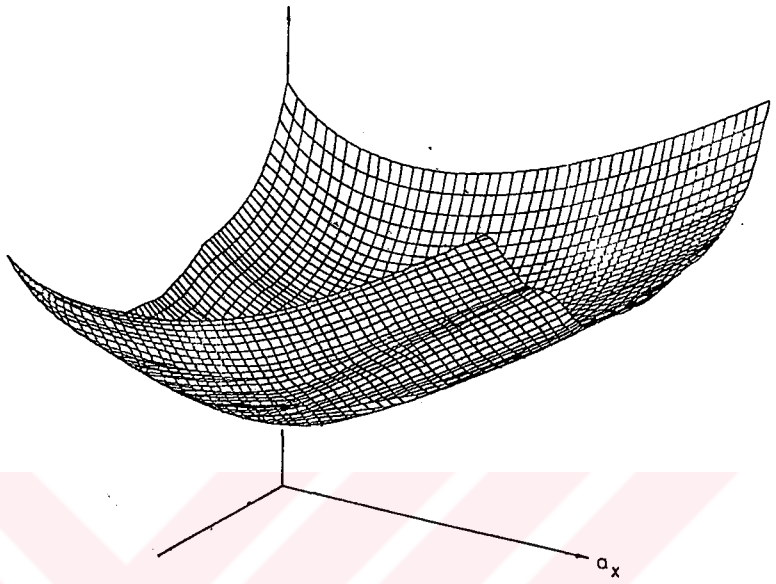

Figure 5.18: The three-dimensional plot of the error function $e(\hat{a}_x, \hat{a}_y)$. The minimum is observed at (4%, 10%). The function is smooth. Finding the minimum is not difficult.

algorithm solved the problem in 83 iterations within the same error bound. The quasi Newton method reached the minimum in 141 iterations. The above algorithms are implemented using a SUN-3 160 workstation, each iteration took approximately 63 seconds.

The block diagram of the proposed iterative motion model parameter estimation algorithm is given in Figure 5.19. In this method, the fluctuation function is assumed to be measured using a displacement transducer. The center of expansion is found using an non-iterative method. And finally, the amplitudes of the fluctuation function along the x and y directions are found by minimizing the amount of motion artifact on the reconstructed image.

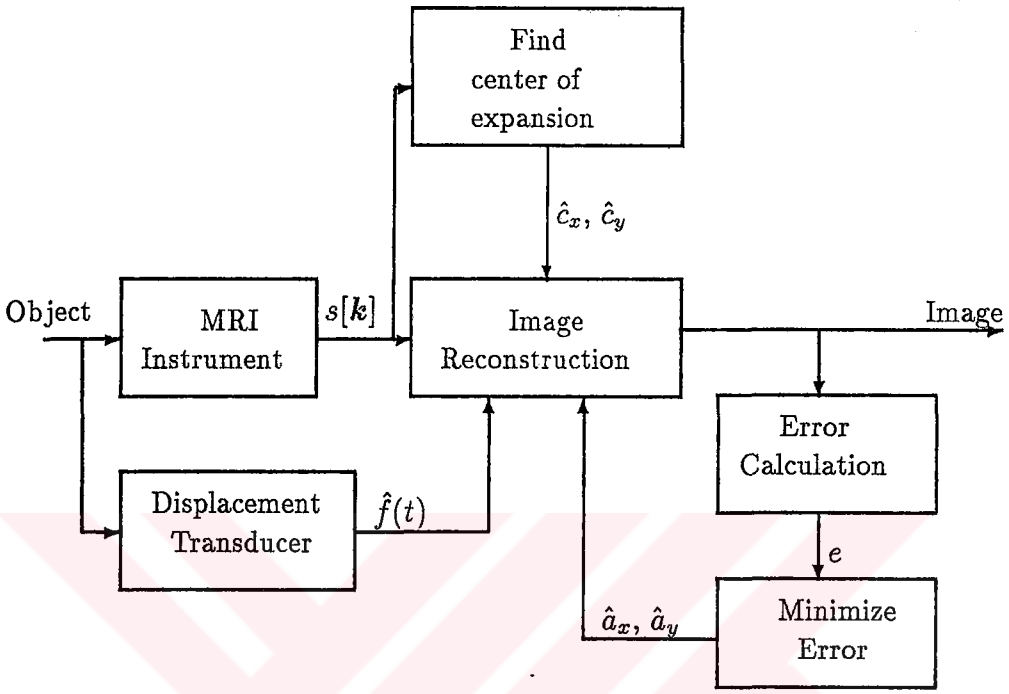

Figure 5.19: The block diagram for the iterative image reconstruction method. $\hat{f}(t)$ is assumed to be already measured by the aid of a displacement transducer. The center of expansion, $(\hat{c}_x, \hat{c}_y)$, is found using $p_x(x)$ and $p_y(y)$. The remaining two motion model parameters which are necessary for the proposed reconstruction method are found by the iterative image reconstruction method. e is the average of the intensity levels at the outside of the region of interest.

5.2.4.ii A parameter estimation method using the navigator echoes

Instead of measuring the motion by displacement transducers, the motion may be measured using the navigator echoes [47], [50]. Using the pulse sequence shown in Figure 5.20, three echoes are obtained in each repetition interval. The first and the third echoes are called the navigator echoes, and the second one is the MR signal which will be used in the image reconstruction.

In this method, the intraview motion of the protons are ignored. They are assumed to be suppressed by the gradient moment nulling (GMN) technique

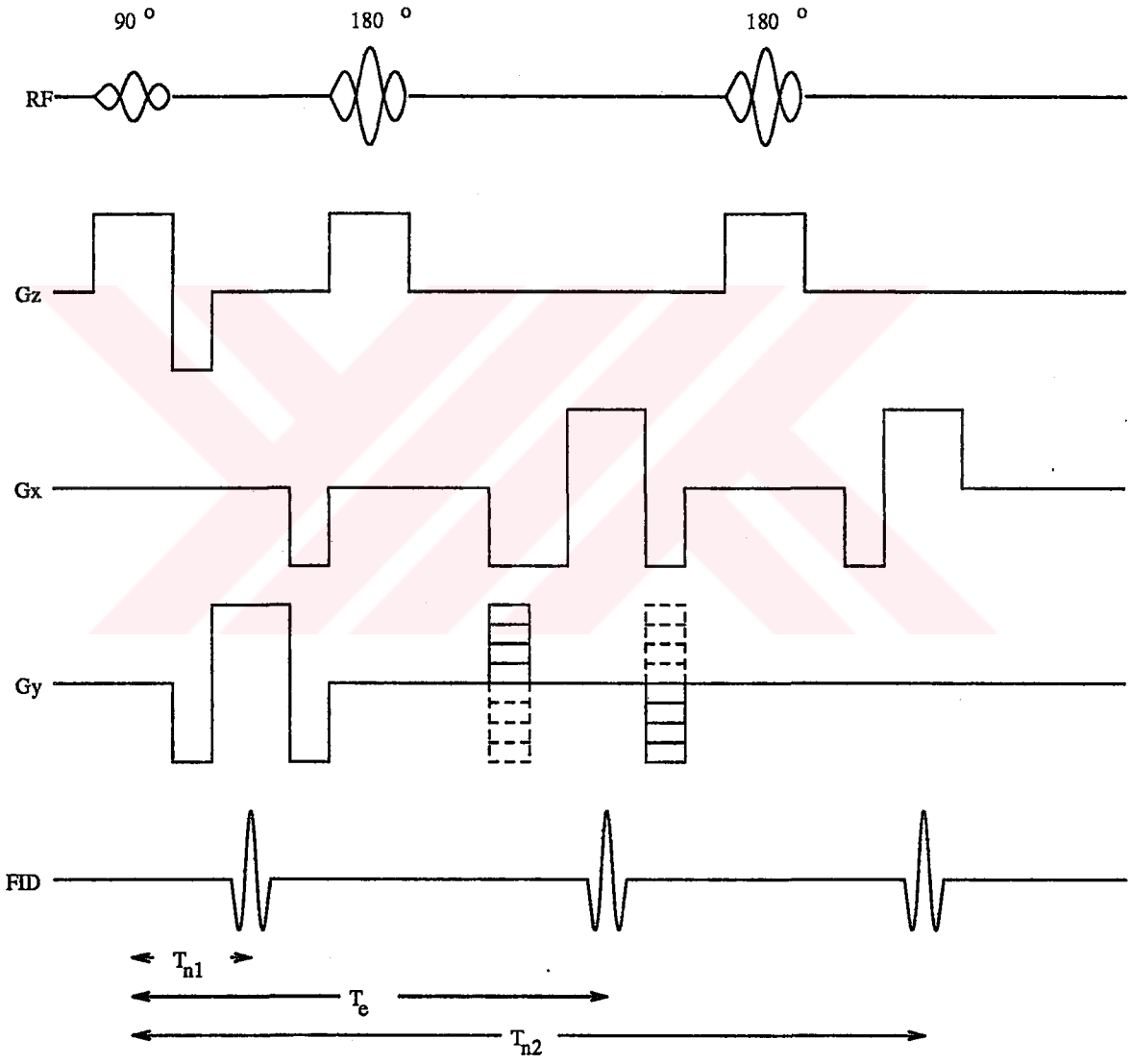

Figure 5.20: MR imaging pulse sequence for generation two navigator echoes.

[31]. And there are only in-plane expansion/shrinkage and block type of motions. Therefore the proton density function can be written as:

$$\tilde{\rho}(\boldsymbol{x}_0; t) = |\mathcal{A}_n| \rho_s(\mathcal{A}_n \boldsymbol{x} + b_n) \tag{5.38}$$

where $|\mathcal{A}_n|$ is the determinant of $\mathcal{A}_n$ and

$$\begin{aligned} \mathcal{A}_n &= \mathcal{A}([0,n]) \\ \boldsymbol{b}_n &= \boldsymbol{b}([0,n]) - \mathcal{A}([0,n])\boldsymbol{c} \end{aligned}$$

If one obtains the values of $\mathcal{A}_n$ and $\boldsymbol{b}_n$ for all n then the reconstruction of the image without any artifact is possible. These values can be found by the aid of the navigator echoes. First, the projection of the proton density distribution onto x and y axes are obtained, then these projections are compared to find $\mathcal{A}_n$ and $\boldsymbol{b}_n$ values.

The first MR signal appears at time $\tau \approx T_{1n}$. Since there is no intraview motion, one can write the relation between the signal and the MR signal as follows:

$$s([\tau, n]) = WD \iint \tilde{\rho}(\boldsymbol{x}_0; [0,n]) \exp\left(j\gamma Q_y(\tau - T_{1n})y\right) dxdy \tag{5.39}$$

where Q_y is the amplitude of the y-gradient when $\tau \approx T_{1n}$. Remember $\boldsymbol{x}_0 = [x, y, 0]^T$. Assume N samples are acquired at time $\tau = t_y k_y/N + T_{1n}$ for $N/2 < k_y \leq -N/2$. After some simple and tedious manipulations the relation between the samples and the FT of the time varying proton density can be obtained as:

$$s\left([\frac{t_y}{N}k_y, n]\right) = WDP_n(0, \frac{2\pi}{f_y}k_y) \tag{5.40}$$

where

$$P_n(\omega_x, \omega_y) = \mathcal{F}_{(2)}\left(\tilde{\rho}(\boldsymbol{x}_0; [0,n])\right) \tag{5.41}$$

Using the projection-slice theorem [51], one can immediately write the following relation:

$$\mathcal{F}_{(1)}^{-1}\left(P(0,\omega_x)\right) = \int \tilde{\rho}(\boldsymbol{x}_0; [0,n]) dx \tag{5.42}$$

where $\mathcal{F}_{(1)}^{-1}$ represents one dimensional inverse Fourier transform. Therefore, the one-dimensional inverse Fourier transform of the navigator echo gives the projection of the proton density distribution onto the y-axis. The similar analysis can be carried out for the third echo. And it can easily demonstrated that the one-dimensional inverse FT of the third echo gives the projection of the proton density onto the y axis.

Let $p_n(y)$ be the projection obtained by the Fourier transformation of the navigator echo at the nth repetition interval.

$$\begin{aligned} p_n(y) &= \int \tilde{\rho}(\boldsymbol{x}_0; [0, n])dx \\ &= a_{xn}a_{yn} \int \rho_s(a_{xn}x + b_{xn}, a_{yn}y + b_{yn})dx \\ &= a_{yn} \int \rho_s(x, a_{yn}y + b_{yn})dx \end{aligned} \tag{5.43}$$

Since the 0th repetition is the reference frame:

$$p_0(y) = \int \rho_s(x, y)dx \tag{5.44}$$

Combining the above equation with Eq. 5.43, the following result can be obtained:

$$p_n(y) = a_{yn}p_0(a_{yn}y + b_{yn}) \tag{5.45}$$

The p_n and p_0 functions are known. The problem is to find the a_{yn} and b_{yn} values. There may be various ways of finding these values, the one which is developed in this dissertation is robust to the non-linearities of the motion.

Let us define the normalized ith moment of the function $p_n(y)$ as:

$$M_n^{(i)} = \frac{\int p_n(y)y^n dy}{\int p_n(y)dy} \tag{5.46}$$

Using this definition one may easily derive the following relations:

$$M_n^{(1)} = \frac{1}{a_{yn}}(M_0^{(1)} - b_{yn}) \tag{5.47}$$

$$M_n^{(2)} = \frac{1}{a_{yn}^2}\left(M_0^{(2)} + 2b_{yn}M_0^{(1)} + b_{yn}^2\right) \tag{5.48}$$

The above equations can be solved for a_{yn} and b_{yn}. The results are:

$$a_{yn} = \sqrt{\frac{M_0^{(2)} - {M_0^{(1)}}^2}{M_n^{(2)} - {M_n^{(1)}}^2}} \tag{5.49}$$

$$b_{yn} = M_0^{(1)} - a_{yn} M_n^{(1)} \tag{5.50}$$

As a result, it is shown that the FT of the navigator echoes are the projections of the moving proton density distribution. Using these projections it is possible to calculate the amount of expansion/shrinkage and the block motion in each repetition interval.

5.3 Rotational Motion

The rotational motion of the object in MR imaging is an interesting subject. There are some methods in the literature on the static imaging of the rotating objects [52], [53] and [54]. In all of these studies the object is assumed to have a constant angular frequency. Cory *et al.* [52] solved the imaging problem by rotating gradients with the same frequency of the object. On the other hand, Matsui *et al.* [53] got the MR image by applying linearly increasing gradient field. In their method, the k-domain is scanned spirally as in [23]. Ogura and Sekihara [54] applied a constant gradient. Their object experienced an oscillating gradient field as in [55].

In our study, the object is assumed to have rotational motion with arbitrarily time varying angular velocity. In addition, the center of the rotation may also be time varying. For the rotational motion, the relation between the proton density distribution and the acquired MR signal is as follows (see Eq. 4.82):

$$\tilde{P}[\boldsymbol{k}] = \xi[\boldsymbol{k}] P_s(\mathcal{V}\boldsymbol{k}_r) \tag{5.51}$$

Therefore, the main image reconstruction ideas for the expansion/shrinkage motion and the rotational motion cases are the same. As it is in the former type of motion, the first step to obtain the static image of the rotating body is

the phase compensation:

$$\overline{P[\boldsymbol{k}]} = \tilde{P}[\boldsymbol{k}]\xi^{-1}[\boldsymbol{k}] \tag{5.52}$$

These phase compensated samples are the non-rectangular samples of the proton density distribution:

$$\overline{P[\boldsymbol{k}]} = P_s(\boldsymbol{\mathcal{V}}\boldsymbol{k}_r) \tag{5.53}$$

To get the static image of this rotating body, the rectangular samples of the object must be interpolated. The two dimensional discrete inverse FT of these recovered rectangular samples will be the static image.

The most important part of the reconstruction method is the interpolation of the rectangular samples using the non-rectangular ones. As it is already proved, the exact recovery of the rectangular samples from the non-rectangular samples is possible if there are enough number of samples.

As in the case of the expansion/shrinkage motion, the position of the non-rectangular samples is not arbitrary. The samples which are acquired in the same repetition interval scan lie on the same straight line. But now, this scan line is not necessarily horizontal. This fact can be shown easily. Let us recall the definition of $\boldsymbol{G}_r$ (see Eq. 4.81):

$$\boldsymbol{G}_r([\tau, n]) = \gamma \int_0^{\tau} \boldsymbol{\mathcal{R}}\left(-\beta([\tau', n])\right) \boldsymbol{g}([\tau', n])\eta(\tau, \tau')d\tau' \tag{5.54}$$

Since the angular velocity of the body may not be very high, one may assume that the body is stationary during the MR data sampling time. So the above equation may be modified if $\tau \approx T_e$ as:

$$\begin{aligned} \boldsymbol{G}_r([\tau, n]) \;=\; & \gamma \int_0^{T_e} \boldsymbol{\mathcal{R}}\left(-\beta([\tau', n])\right) \boldsymbol{g}([\tau', n])\eta(\tau, \tau')d\tau' + \\ & \boldsymbol{\mathcal{R}}\left(-\beta([T_e, n])\right) \begin{bmatrix} Q_x \\ 0 \end{bmatrix} (\tau - T_e) \end{aligned} \tag{5.55}$$

If the MR is signal is sampled at the time $[k_x t_x/N + T_e, k_y]$, $\boldsymbol{k}_r$ can be found as:

$$\boldsymbol{k}_r[k_x, k_y] = \boldsymbol{\mathcal{V}}^{-1} \left(\frac{2\pi}{f_x} \boldsymbol{\mathcal{R}}(\beta[k_y]) \begin{bmatrix} k_x \\ 0 \end{bmatrix} + \boldsymbol{q}[k_y] \right) \tag{5.56}$$

where

$$\begin{aligned} \boldsymbol{q}[k_y] &= \gamma \int_0^{T_e} \mathcal{R}(\beta([\tau', k_y])\boldsymbol{g}([\tau', k_y])\eta(\tau', T_e)d\tau' \\ \beta[k_y] &= \beta([T_e, k_y]) \end{aligned}$$

If there were no rotational motion, then $\beta[k_y]$ would be zero all the time and $\boldsymbol{q}[k_y] = 2\pi \boldsymbol{k}_y / f_x$. Therefore, if there were no motion $\boldsymbol{k}_r$ would be equal to $\boldsymbol{k}$.

On the other hand, if there is rotational motion, $\boldsymbol{q}$ and $\beta[k_y]$ may take arbitrary values. The careful analysis of Eq. 5.56 depicts the fact that for a constant k_y value, the samples on the k-domain will be on a non-horizontal line.

Although the problem of finding the rectangular samples over the k-domain using the non-rectangular ones is a two-dimensional problem, using the above property of the acquired samples it can be reduced to 2 one-dimensional problems as in the case of the expansion/shrinkage motion.

The most important question of this method is the possibility of having an ill conditioned problem. The non-rectangular samples may be placed so that some considerable large regions have no samples. This fact makes the interpolation of these regions practically impossible. If the maximum deviation of the angle of rotation is small enough the possibility of having such regions decreases. Further studies on the reconstruction algorithm is left as a future research area.

5.4 The Expansion/Shrinkage Along the z-direction

The static image reconstruction algorithm for an object which has an expansion/shrinkage motion along the z-direction is very similar to the algorithm proposed for the block motion. In the expansion/shrinkage motion along the z direction, the the MR data correspond to the amplitude distorted samples over k-domain. Remember that there was a phase distortion in the block motion case. For the expansion/shrinkage along the z direction, the image reconstruction algorithm starts with the evaluation of the amplitude distortion. Then the

amplitude compensated rectangular k-domain samples is found. And the image is reconstructed by calculating the inverse discrete Fourier transform of these rectangular samples.

In case of expansion/shrinkage motion along the z-direction, the relation between the acquired MR data set and the k-domain can be written as (See Eq. 4.97):

$$\tilde{P}[\boldsymbol{k}] = \xi[\boldsymbol{k}] P_s(\mathcal{V}\boldsymbol{k}) \tag{5.57}$$

where (See Equations 4.98, 4.99, 4.96 and 4.94)

$$\xi[\boldsymbol{k}] = \frac{WD}{1 + A_z([0,k])} \mathrm{sinc}(\Delta k_z) \tag{5.58}$$

$$\Delta k_z = \frac{D}{2\pi} \Delta G_z([k_x t_x/N + T_e, k_y]) \tag{5.59}$$

$$\Delta G_z([\tau, n]) = \gamma \int_0^{\tau} g_z([\tau', n]) A'_z([\tau', n]) \eta(\tau, \tau') d\tau' \tag{5.60}$$

$$A'_z([\tau, n]) = \frac{A_z([\tau, n]) - A_z([0, n])}{1 + A_z([0, n])} \tag{5.61}$$

In the above equations, W, D, t_x, N, T_e, g_z, and η are the parameters which are related to the pulse sequence and all of them are known. $A_z(t)$ stands for the amount of expansion along the z-direction. Therefore, once $A_z(t)$ is known evaluation of the amplitude distortion is not difficult.

Using the acquired MR data set and these calculated values, the rectangular samples over the k-domain can be evaluated as:

$$P_s(\mathcal{V}\boldsymbol{k}) = \tilde{P}[\boldsymbol{k}] \xi^{-1}[\boldsymbol{k}] \tag{5.62}$$

And finally, the inverse discrete Fourier transform of these calculated values gives the desired motion artifact free image.

It is interesting to observe the study carried out by Mitsa *et. al.* [35]. In their study an infinitely thin object oscillates along the z direction. This motion causes amplitude distortion as in the case of expansion/shrinkage motion. Mitsa *et. al.* developed an iterative method which corrects this amplitude distortion. In this excellent iterative method, it is not necessary to know the motion model parameters. However, their methods has no practical application because in

reality infinitely thin objects can not be found. With a modification, their method can be used in reduction of the expansion/shrinkage motion along the z direction. Because the expansion/shrinkage motion of a thick object along the z direction and the z motion of an infinitely thin object cause exactly the same type of artifact.

Chapter 6

CONCLUSION AND FURTHER RESEARCH AREAS

In this dissertation, the motion artifact in magnetic resonance imaging is analyzed. Useful formulas for the block, expansion/shrinkage and rotational motions are derived. It is proved that if these types of motions exist during the data acquisition period, the samples of the MRI signal are the phase and amplitude distorted non-rectangular samples of the Fourier transform of the proton density distribution of the body.

In the image reconstruction methods which are proposed in this dissertation, the distortion is compensated and the rectangular samples are interpolated. It is proved that for these type of motions, the problem of calculating the rectangular samples using the non-rectangular samples can be converted into two one-dimensional problems. This yields significant computational savings.

In this dissertation, the in-plane expansion/shrinkage motion is simulated for a fictitious phantom and the image reconstruction method for this type of motion is used to eliminate the motion artifact. It is observed that the image quality depends on the interpolation method. Best results are obtained when the singular value decomposition method is utilized as the interpolation method.

But because of the high computation cost of this method some other interpolation methods are also tested. It is observed that the quality of the images decreases with the methods which have lower computational cost. Although the optimum interpolation method depends on the application, the author recommends the cubic spline interpolation method which increases the computation time by 30 %.

Some properties of the proposed image reconstruction methods are:

- The proposed methods can be used to reduce the motion artifact of a object whose motion is an arbitrary function of time.
- These methods are robust with respect to the estimates of the motion model parameters. These estimates are used during image reconstruction. The methods work even if the accurate estimates of these parameters are not available. Considerable improvement in the image quality can still be obtained even if the estimates are not very accurate.
- The methods can be used in conjunction with any Fourier transform imaging pulse sequence. Therefore, already proposed motion artifact suppression methods in the literature can be combined with the proposed method to get better results.

An important issue which is investigated in this dissertation is the modeling of the motion. It is believed that the MR signal itself contains information on the motion, and the related motion model parameters can be estimated. For this purpose, an iterative image reconstruction method is proposed. In this method the two of the expansion/shrinkage motion model parameters (a_x and a_y) are found iteratively. This method could be easily adopted to the other motion types to find their parameters. The most important problem of this method is the computation cost because of the iterative nature of the motion.

The possible applications of the proposed image reconstruction methods are respiratory motion artifact suppression in the transaxial imaging of the chest, conscious motion of the head and eye. All of these cases should be experimentally

verified. The verification of the proposed image reconstruction methods is not done in this dissertation. The experiments are left to the future studies.

Another issue which may be analyzed in the future studies is the recovery of the rectangular samples from the non-rectangular ones. The interpolation methods used in this dissertation failed if there are some regions which has no or very few samples. This situation is important especially for the rotational motion artifact reduction. To overcome this difficulty the singular value decomposition or similar techniques are used. However, the performance of these methods might be increased using the property:

$$P_s(\omega_x, \omega_y) = P_s^*(-\omega_x, -\omega_y) \tag{6.1}$$

It is known that the proton density distribution is a real function. Therefore, its Fourier transform proton density distribution should hold the above relation. Therefore every non-rectangular sample corresponds to two points in the k-domain. In this way, the number of non-uniform samples in the k-domain may be doubled. There are some practical difficulties of this method, and the implementation is of this method requires further studies.

APPENDICES

A Basic NMR Equation for the Rotating Frame

In this appendix, the statement "the rotating frame cancels the effect of the main magnetic field" will be proved. This statement was formulated in Eq. 2.11 as:

$$\frac{d\boldsymbol{m}'}{dt} = \gamma \boldsymbol{m}' \times \boldsymbol{h}_{eff} \tag{A.1}$$

where

$$\boldsymbol{h}_{eff} = \boldsymbol{h}' - H_0 \hat{\boldsymbol{z}} \tag{A.2}$$

To obtain the above formulation the following steps are carried out.

The relation between the magnetization in the stationary and rotating frames can be written as:

$$\boldsymbol{m} = \mathcal{R}_z(\omega_0 t)\boldsymbol{m}' \tag{A.3}$$

where $\mathcal{R}_u(\alpha)$ is the rotation matrix around u-axis in counter clockwise direction. For example:

$$\mathcal{R}_z(\alpha) = \begin{bmatrix} \cos(\alpha) & \sin(\alpha) & 0 \\ -\sin(\alpha) & \cos(\alpha) & 0 \\ 0 & 0 & 1 \end{bmatrix}$$

Similarly, the magnetic field in the stationary and rotating frames have the relation:

$$\boldsymbol{h} = \mathcal{R}_z(\omega_0 t)\boldsymbol{h}' \tag{A.4}$$

The basic equation of the NMR defines a relation between the magnetization of the protons and the magnetic field which affects these protons (see Eq. 2.5).

$$\frac{d\boldsymbol{m}}{dt} = \gamma \boldsymbol{m} \times \boldsymbol{h} \tag{A.5}$$

If one substitutes the equation A.3 into the above equation, the following result will be obtained.

$$\frac{d\mathcal{R}_z(\omega_0 t)}{dt}\boldsymbol{m}' + \mathcal{R}(\omega_0 t)\frac{d\boldsymbol{m}'}{dt} = \gamma \boldsymbol{m} \times \boldsymbol{h} \tag{A.6}$$

On the other hand, it can be shown that:

$$\frac{d\mathcal{R}_z(\omega_0 t)}{dt}\boldsymbol{m}' = \omega_0 \mathcal{R}_z(\omega_0 t)\,(\boldsymbol{m}' \times \hat{\boldsymbol{z}}) \tag{A.7}$$

where $\hat{\boldsymbol{z}}$ is the unit vector in the z direction. Using the above equation, the relation A.6 can be reduced into the following form:

$$\frac{d\boldsymbol{m}'}{dt} = \gamma \mathcal{R}_z^{-1}(\omega t)\,(\boldsymbol{m} \times \boldsymbol{h}) - \omega_0 \boldsymbol{m}' \times \hat{\boldsymbol{z}} \tag{A.8}$$

Knowing that

$$\mathcal{R}_z(\omega_0 t)\,(\boldsymbol{a} \times \boldsymbol{b}) = (\mathcal{R}_z(\omega_0 t)\boldsymbol{a}) \times (\mathcal{R}_z(\omega_0 t)\boldsymbol{b}) \tag{A.9}$$

one may simplify Eq. A.8 as:

$$\frac{d\boldsymbol{m}'}{dt} = \gamma \boldsymbol{m}' \times (\boldsymbol{h}' - H_0 \hat{\boldsymbol{z}}) \tag{A.10}$$

This completes the proof of Eq. A.1.

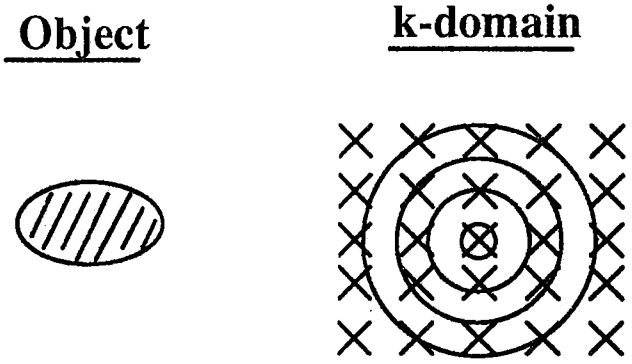

Figure B.1: The proton density distribution of a stationary object. The k-domain is sampled rectangularly.

B The Effect of Motion: Examples

This appendix is prepared to give a feeling to the reader to understand the relation between the proton density distribution of a moving object and the samples of the MR signal. In this appendix, the block, expansion/shrinkage and rotational motions will be analyzed on some simple examples. In these examples, the intraview motion is ignored and it is assumed that there are 5 repetition intervals and 5 samples are acquired in each repetition interval.

Let the proton density distribution of an object be as shown in Figure B.1. If there were no motion, the samples of the MR signal would correspond to the rectangular samples over the k-domain (the Fourier transform domain).

B.1 Block Motion

It is known that the shift in the space domain corresponds to the linear phase change in the k-domain. For example if the object displaces along the y-direction by a distance of y_0, the Fourier transform of the original object must be multiplied by $\exp(-j\omega_y y_0)$. Assume that the object is in the original position during the first repetition interval as shown in Figure B.2a. Assume that the object is displaced by y_0 along the y-direction before the second repetition interval. The phase of

the Fourier transform of the object is changed and the new samples are acquired on the second row with these new phases (See Figure B.2b). Again it is assumed that the object goes back the original position before the third repetition interval. And the samples acquired during the third repetition interval have the original phases. In the fourth repetition interval, the object displaces along the y-direction by a distance of y_0 one more time. The phases of the samples acquired during this repetition interval are changed. And at the last repetition interval, object goes back its original position again. The samples acquired during this interval have original phases (See Figure B.2e). As a result, for this simple motion, the samples acquired have different phase distortions depending on the position of the object at the data acquisition time. The data which are acquired on the second and the fourth rows have phase distortions but there are no phase distortion on the other samples (See Figure B.2).

If one considers the intraview motion as well as the view-to-view motion, the same effect on the acquired samples will be observed. But the calculation of the amount of phase distortion requires some manipulations (See Section 4.3.1).

B.2 Expansion/Shrinkage

It is known that expansion in the space domain corresponds to shrinkage in the k-domain. Assume that the object is in the original position during the first repetition interval (See Figure B.3a). Five samples are acquired during this period. It is assumed that the object is expanded just before the second repetition interval (See Figure B.3b). The FT of the proton density distribution is shrunk and the new samples are acquired on this domain. The object goes back the original form before the third repetition interval (See Figure B.3c). And the samples acquired during the third repetition interval are on the original domain. In the fourth repetition interval the object is expanded one more time. The samples acquired during this repetition interval are on the shrunk FT domain. And at the last repetition interval, the object goes back its original position. The samples acquired during this interval have original phases. Since there is a one to one relation between the original FT domain and the shrunk FT domain, all

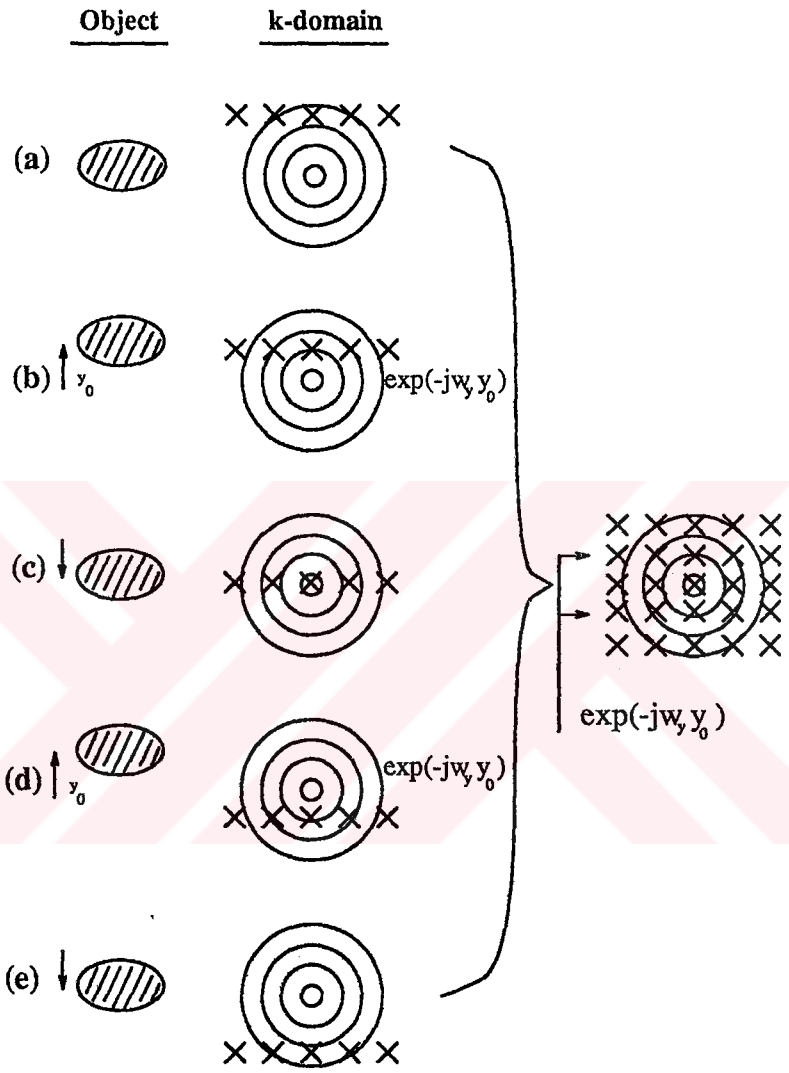

Figure B.2: An example for the block motion. (a) First repetition interval. The position of the samples are shown by cross-marks. (b) Second repetition interval. The object displaces along the y-direction and the phase of its Fourier transform changes. (c) Third repetition interval. The object goes back its original position. The samples are acquired on the third row. (d) Fourth repetition interval. The object moves along the y-direction. (e) Fifth repetition interval. The object goes back the original position one more time. In the image shown at the right hand side, all the samples are placed on the FT of the original form of the object. The samples acquired on the second and fourth rows have phase distortion.

the samples may be collected in one domain as shown in Figure B.3. As a result, for this simple example, the samples acquired during the expansion/shrinkage of the body correspond to non-rectangular samples over the k-domain.

In addition to the view-to-view motion, if there were intraview motion, the expansion/shrinkage would have the same effect on the acquired samples but finding the positions of the samples would not be as simple as in this example. In addition to that in the above example the center of expansion is assumed to be at the center of the image. But if the center of the expansion and the center of the image do not coincide then additional phase distortion will be observed (See Section 4.3.2).

B.3 Rotational Motion

It is known that a rotation in the space domain corresponds to a rotation in the k-domain. Assume that the object is at the original position during the first repetition interval (See Figure B.4a). And assume that the object is rotated before the second repetition interval (See Figure B.4b). The FT of the proton density distribution is also rotated and the new samples are acquired on this domain. It is assumed that object goes back the original position before the third repetition interval (See Figure B.4c). And the samples acquired during the third repetition interval are on the original domain. Assume that the object is rotated one more time. The samples acquired during this repetition interval are on the rotated FT domain. And at the last repetition interval, the object goes back its original position. The samples acquired during this interval have original phases. Since there is a one to one relation between the original FT domain and the rotated FT domain, all the samples may be collected in one domain as shown in Figure B.4. As a result, for this simple example, the samples acquired during the rotational motion of the body correspond to non-rectangular samples over the k-domain.

If one also considers the intraview motion, the rotational motion causes sample position shift as in the view-to-view case. But the method for finding the position of the samples will be different. In addition, in the above example the center

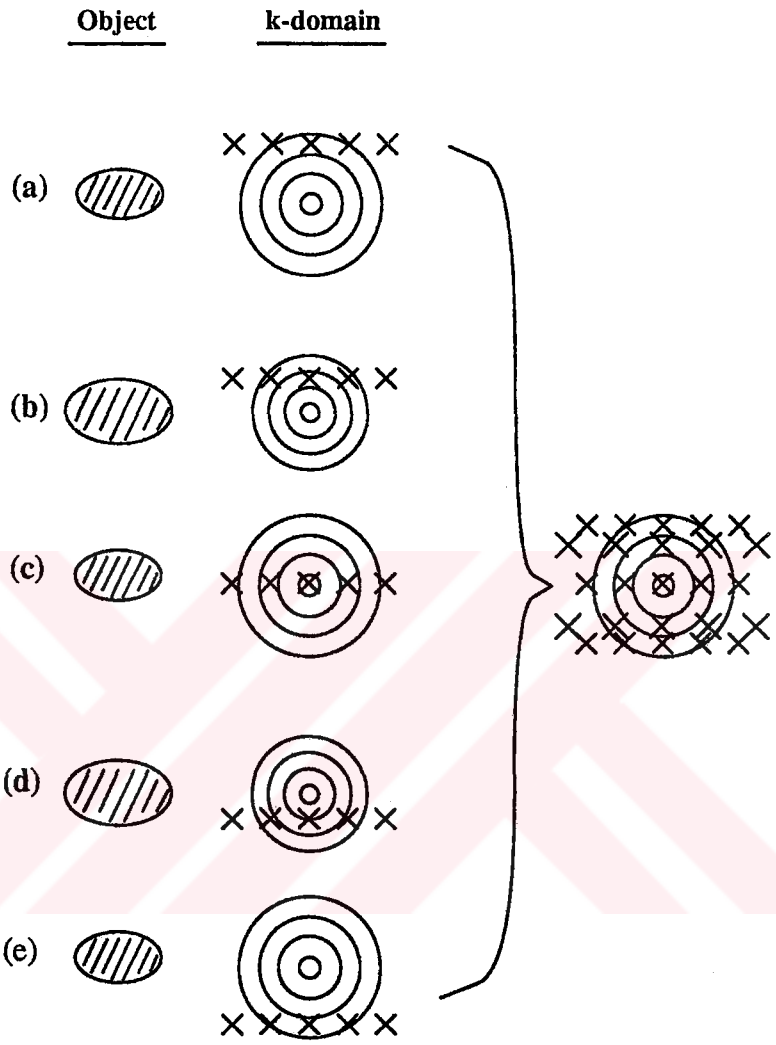

Figure B.3: An example for the expansion/shrinkage. (a) First repetition interval. 5 samples are acquired on the k-domain. The position of these samples are shown by cross-marks. (b) Second repetition interval. The object expands and its Fourier transform shrinks. Five samples are acquired on the second row. (c) Third repetition interval. The object goes back its original form. The samples are acquired on the third row. (d) Fourth repetition interval. The object expands. (e) Fifth repetition interval. The object goes back the original form one more time. In the image shown at the right hand side, all the samples are placed on the FT of the original form of the object.

of rotation is assumed to be at the center of the image. But if the center of the rotation and the center of the image do not coincide then additional phase distortion will be observed (See Section 4.3.3).

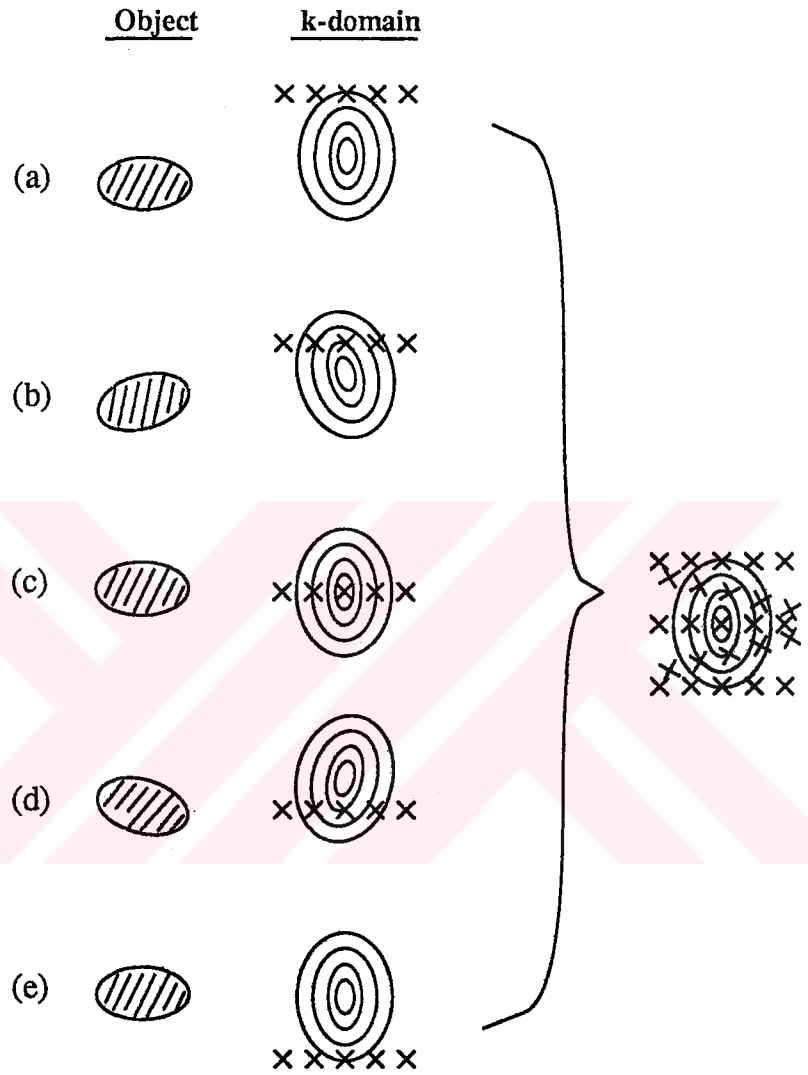

Figure B.4: An example for the rotational motion. (a) First repetition interval. 5 samples are acquired on the k-domain. The position of these samples are shown by cross-marks. (b) Second repetition interval. The object rotates and as a result its Fourier transform also rotates. Five samples are acquired on the second row. (c) Third repetition interval. The object goes back its original form. The samples are acquired on the third row. (d) Fourth repetition interval. The object rotates. (e) Fifth repetition interval. The object goes back the original form one more time. In the image shown at the right hand side, all the samples are placed on the FT of the original form of the object.

C Some Interpolation Algorithms

In this appendix, three interpolation methods (linear, third order Lagrange, and cubic spline) are introduced. These methods are used to get a signal of which the non-uniform samples are given.

Let $h(t)$ be a bandlimited signal and let $\{t_i : i = 1 \dots N\}$ be an arbitrary set of time instances. Without loss of generality one may assume $t_i \geq t_j$ if $i > j$. Let $\hat{h}(t)$ be the signal which is obtained by the interpolation of $\{h(t_i) : i = 1 \dots N\}$.

Linear interpolation is defined as:

$$\hat{h}(t) = \begin{cases} D_1^1 h(t_{i+1}) + D_0^1 h(t_i) & t_{i+1} \geq t > t_i, \quad i = 1, 2 \dots N-1 \\ 0 & \text{otherwise} \end{cases} \tag{C.1}$$

where

$$D_k^m = \prod_{\substack{j=0 \\ j \neq k}}^{m} \frac{t - t_j}{t_k - t_j} \tag{C.2}$$

The linear interpolation may be called first order Lagrange interpolation.

The **third order Lagrange interpolation** is defined as:

$$\hat{h}(t) = \begin{cases} \sum_{k=0}^{3} D_k^3 h(t_{i+k}) & t_{i+2} \geq t > t_{i+1}, \quad i = 1, 2 \dots N-3 \\ 0 & \text{otherwise} \end{cases} \tag{C.3}$$

The **cubic spline** is an interpolation method for smooth functions. Each time segment $[t_{i+1} \dots t_i]$ is interpolated by a third order polynomial function, $\hat{h}_i(t)$. The coefficients of these functions are calculated so that:

$$\hat{h}_i(t_i) = h(t_i) \tag{C.4}$$

$$\hat{h}_i(t_{i+1}) = h(t_{i+1}) \tag{C.5}$$

$$\hat{h}_i'(t_i) = \hat{h}_{i-1}'(t_i) \tag{C.6}$$

$$\hat{h}_i'(t_{i+1}) = \hat{h}_{i+1}'(t_{i+1}) \tag{C.7}$$

where $\hat{h}'(t)$ is the first derivative of $\hat{h}(t)$. As a boundary condition, $\hat{h}_0'(t_1)$ and $\hat{h}_{N+1}'(t_N)$ are assumed to be zero. For cubic spline interpolation, the function

$\hat{h}(t)$ is defined as:

$$\hat{h}(t) = \begin{cases} h_i & t_{i+1} \geq t > t_i, \quad i = 1, 2 \ldots N-1 \\ 0 & \text{otherwise} \end{cases} \tag{C.8}$$

For the details of these interpolation methods, see rf. [45].

Bibliography

[1] Felix Bloch "Nuclear induction," *Physical Review*, vol. 70, pp. 460–474, 1946.

[2] E. M. Purcell, H. C. Torrey, and R. V. Pound "Resonance absorbtion by nuclear magnetic moments in a solid," *Physical Review*, vol. 69, pp. 37–38, 1946.

[3] Paul C. Lauterbur "Image formation by induced local interactions: Examples employing nuclear magnetic resonance," *Nature*, vol. 242, pp. 190–191, March 1973.

[4] David G. Norris "Ultrafast low-angle RARE: U-FLARE," *Magnetic Resonance in Medicine*, vol. 17, pp. 539–541, February 1991.

[5] Peter G. Morris. *Nuclear Magnetic Resonance Imaging in Medicine and Biology.* Oxford University Press, Walton Street, Oxford OX2 6DP England, 1986.

[6] Z. H. Cho, H. S. Kim, H. B. Song, and James Cumming "Fourier transform nuclear magnetic resonance tomographic imaging," *Proceedings of the IEEE*, vol. 70, pp. 1152–1173, October 1982.

[7] Thomas L. James and Alexander R. Margulis, eds. *Biomedical Magnetic Resonance.* Radiology Research and Education Foundation, Third and Parnassus Avenues-Suite C324 SAn Francisco, California 94143 U.S.A., 1984.

[8] P. G. Mansfield and Peter G. Morris. *NMR Imaging in Biomedicine.* Supplement 2 Advances in MAgnetic Resonance. Academic Press, 111 Fifth Avenue, New York, New York 10003 U.S.A, 1982.

[9] Thomas C. Farrar and Edwin D. Becker. *Pulse and Fourier Transform NMR Introduction to Theory and Methods.* Academic Press, 111 Fifth Avenue, New York, New York 10003, 2 edition, 1974.

[10] Atta ur Rahman. *Nuclear Magnetic Resonance Basic Principles.* Springer-Verlag New York Inc., 175 Fifth Avenue, New York, New York 10010, U.S.A., 1986.

[11] Derek Shaw. *Fourier Transform N. M. R. Spectroscopy.* Elsevier Scientific Publishing Company, 335 Jan van Galenstraat P.O. Box 211, 1000 AE Amsterdam, The Netherlands, 1976.

[12] Denis L. Rousseau, ed. *Structural and Resonance Techniques in Biological Reseach.* Academic Press, Inc., Orlando, Florida 32887, 1984.

[13] Eiichi Fukushima and Stephen B. W. Roeder. *Experimental Pulse NMR A Nuts and Bolts Approach.* Addison-Wesley Publishing Company, Inc., Massachusetts 01867, U.S.A, 1981.

[14] Allexander R. Margulis, Charles B. Higgins, Leon Kaufman, and Lawrence E. Crooks, eds. *Clinical Magnetic Resonance Imaging.* Radiology Research and Education Foundation, Third and Parnassus Avenues-Suite C324, San Francisco, California 94143, 1983.

[15] Margaret A. Foster and James M. S. Hutchison, eds. *Practical NMR Imaging.* IRL Press, Oxford Washington DC, 1987.

[16] A. Abragam. *Principles of Nuclear Magnetism.* The International Series of Monographs on Physics. Oxford University Press, Walton Street, Oxford OX2 6DP England, 1986.

[17] Richard P. Feynman, Robert B. Leighton, and Matthew Sands. *The Feynman Lectures on Physics*, volume II. Addison Wesley Publishing Company, Inc., korean edition, 1984.

[18] Richard P. Feynman, Robert B. Leighton, and Matthew Sands. *The Feynman Lectures on Physics*, volume I. Addison Wesley Publishing Company, Inc., korean edition, 1984.

[19] Bong-Soo Kim. "Design study of high sensitive RF coil in NMR imaging system,". Master's thesis, Imaging System Sceince Lab. Department of Electrical Engineering, Korea Advanced Institute of Science and Technology, 1985.

[20] Soo Yeol Lee. "Design and analysis of ring resonator RF coils for high-field NMR system,". Master's thesis, Imaging System Sceince Lab. Department of Electrical Engineering, Korea Advanced Institute of Science and Technology, 1985.

[21] Ghy-Boong Hong. "Design of RF coil for high field NMR imaging,". Master's thesis, Imaging System Sceince Lab. Department of Electrical Engineering, Korea Advanced Institute of Science and Technology, 1984.

[22] P. G. Mansfield and Peter G. Morris. *NMR Imaging in Biomedicine*, pp. 65–77. Supplement 2 Advances in MAgnetic Resonance. Academic Press, 111 Fifth Avenue, New York, New York 10003 U.S.A, 1982.

[23] C. B. Ahn, J. H. Kim, and Z. H. Cho "High-speed spiral-scan echo planar NMR imaging-I," *IEEE Trans. on Medical Imaging*, vol. MI-5, pp. 2–7, March 1986.

[24] D.R. Bailes, D.J. Gilderdale, G.M. Bydder, A.G. Collins, and D.M. Firmin "Respiratory ordered phase encoding (ROPE): A method for reduction respiratory motion artifacts in MR imaging," *Journal of Computer Assisted Tomograph*, vol. 9, pp. 835–838, July/August 1985.

[25] Val. M. Runge, J.A. Clanton, C.L. Partain, and A.E. James "Respiratory gating in magnetic resonance imaging at 0.5 tesla," *Radiology*, vol. 151, pp. 512–523, 1984.

[26] Michael L. Wood and R.Mark Henkelman "Suppression of respiratory motion artifacts in magnetic resonance imaging," *Medical Physics*, vol. 13, pp. 794–805, November/December 1986.

[27] Micheal L. Wood, Val M. Runge, and R. Mark Henkelman "Overcoming motion in abdominal MR imaging," *American Journal of Roentgenol.*, vol. 150, pp. 513–522, March 1987.

[28] W. Thomas Dixon, Marijn E. Brummer, and John A. Malko "Acquistion order and motional artifact reduction in spin warp images," *Magnetic Resonance in Medicine*, vol. 6, pp. 74–83, 1988.

[29] E. Mark Haacke, Gerald W. Lenz, and A. Dennis Nelson "Pseudo-gating: Elimination of periodic motion artifacts in magnetic resonance imaging without gating," *Magnetic Resonance in Medicine*, vol. 4, pp. 162–174, 1987.

[30] Robert R. Edelman, Dennis J. Atkinson, Michael S. Silver, Francisco L. Loaiza, and Warren S. Warren "FRODO pulse sequences: A new means of eliminating motion, flow and wraparound artifacts," *Radiology*, vol. 166, pp. 231–236, 1988.

[31] Pradip M. Pattany, Jeffrey J. Phillips, Lee C. Chiu, James D. Lipcamon, Jeffrey L. Duerk, James M. McNally, and Surya N. Mohapatra "Motion artifact suppresion technique (MAST) for MR imaging," *Journal of Computer Assisted Tomograph*, vol. 11, pp. 369–377, May/June 1987.

[32] Allen D. Elster "Motion artifact suppression technique (MAST) for cranial MR imaging: Superiority over cardiac gating for reducing phase-shift artifacts," *American Journal of Neuroradiology*, vol. 9, pp. 671–674, August 1988.

[33] Donald G. Mitchell, Simon Vinitski, Jr D. Lawrence Burk, David W. Levy, and Matthew D. Rifkin "Motion artifact reduction in MR imaging of the abdomen: Gradient moment nulling versus respiratory-sorted phase encoding," *Radiology*, vol. 169, pp. 155–160, October 1988.

[34] E. Mark Haacke, Z.-P. Liang, and F. Boada "Image reconstruction using projection onto convex sets, model constraints, and linear prediction theory for removal of phase, motion, and gibbs artifacts in magnetic resonance and ultrasound imaging," *Optical Engineering*, vol. 29, pp. 555–566, May 1990.

[35] T. Mitsa, K. J. Parker, W. E. Smith, A. M. Tekbas, and J. Szumowski. "Correction of periodic motion artifacts along the slice selection axis in MRI,". *IEEE Trans. Med. Imaging* accepted for publication.

[36] Murray R. Spiegel. *Theory and Problems of Advanced Calculus*, chapter 6. McGraw-Hill Book Company, 1974.

[37] Michael L. Wood and R. Mark Henkelman "MR image artifacts from periodic motion," *Medical Physics*, vol. 12, pp. 143–151, March/April 1985.

[38] I. S. Gradshteyn and I. M. Ryzhik. *Table of Intergals, Series, and Products*, chapter 7. Academic Press, Orlando, Florida, 1980.

[39] Hope W. Korin, Farhad Fanzaneh, Ronald C. Wright, and Stephen J. Riederer "Compensation for effects of linear motion in MR imaging," *Magnetic Resonance in Medicine*, vol. 12, pp. 99–113, 1989.

[40] E. Mark Haacke and John. L. Patrick "Reducing motion artifacts in two-dimensional fourier transform imaging," *Magnetic Resonance Imaging*, vol. 4, pp. 359–376, 1986.

[41] Ergin Atalar and Levent Onural "A respiratory motion artifact reduction method in magnetic resoance imaging of the chest," *IEEE Transactions on Medical Imaging*, vol. MI-10, pp. 11–24, March 1991.

[42] J. L. Yen "On nonuniform sampling of bandwidth-limited signals," *IRE Transaction on Circuit Theory*, vol. CT-3, pp. 251–257, December 1956.

[43] A. Oppenheim and A. S. Willsky. *Signals and Systems*, pp. 522–523. Prentice-Hall, Inc., Englewood Cliffs, NJ, 1983.

[44] Thomas Muir. *A Treatise on the Theory of Determinants*, chapter 11, pp. 321–363. Dover Publications, Inc., New York, 1950.

[45] W. H. Press, B. P. Flannery, S. A. Teukolsky, and W. T. Vetterling. *Numerical Recipes in C.* Cambridge University Press, Boston MA, 1988.

[46] Hakan Musa Asyali. "Analysis of respiratory motion of human at rest,". Ee 492 senior project, Bilkent University, Dept. of Electrical and Electronics Eng., 1990.

[47] Richard L. Ehman and Joel P. Felmlee "Adaptive techniques for high-definition MR imaging of moving structures," *Radiology*, vol. 173, pp. 255–263, 1989.

[48] Ergin Atalar and Levent Onural "An iterative image reconstruction method for respiratory artifact reduction in MRI of chest," in *Proc. Europ. Congr. NMR Med. Biol.*, p. 355, Strasbourg, May 2-5 1990.

[49] P. E. Gill, W. Murray, and M. H. Wright. *Practical Optimization*, chapter 4, pp. 83–153. Academic Press, London, 1981.

[50] W. S. Kim, C. W. Mun, D. J. Kim, and Z. H. Cho "Extraction of cardiac and respiratory motion cycles by use of projection data and its applications to NMR imaging," *Magnetic Resonance in Medicine*, vol. 13, pp. 25–27, January 1990.

[51] Dan E. Dudgeon and Russell M. Mersereau. *Multidimensional Digital Signal Processing*, pp. 366–367. Prentice-Hall, Inc., Englewood Cliffs, NJ, 1984.

[52] D. G. Cory, J. M. Van Os, and W. S. Veeman "NMR images of rotating solids," *Journal of Magnetic Resonance*, vol. 76, pp. 543–547, 1988.

[53] S. Matsui, K. Sekihara, H. Shiono, and H. Kohno "A static NMR image of a rotating object," *Journal of Magnetic Resonance*, vol. 77, pp. 182–186, 1988.

[54] Yukiko Ogura and Kensuke Sekihara "A new method for static imaging of a rotating object," *Journal of Magnetic Resonance*, vol. 83, pp. 177–182, 1989.

[55] Albert Mackovski "Volumetric NMR imaging with time-varying gradients," *Magnetic Resonance in Medicine*, vol. 2, pp. 29–39, 1985.